

SPIN-RELATED OPTICAL BISTABILITY AND TRISTABILITY

by

Masao KITANO

February 1984

Radio Atmospheric Science Center

Kyoto University

Uji, Kyoto 611, Japan

DOCTORAL THESIS
SUBMITTED TO
THE FACULTY OF ENGINEERING
KYOTO UNIVERSITY

ACKNOWLEDGEMENTS

The author would like to express his sincere appreciation to Professor Toru Ogawa for his continuous guidance, many stimulating suggestions and discussions throughout the present work. The author is deeply grateful to Dr. Tsutomu Yabuzaki for many helpful discussions and encouragement in all phases of this work. In addition to their specific contributions, they helped create an atmosphere in which learning and growth came naturally.

The author also wishes to express his deep appreciation to Professors Susumu Kato and Iwane Kimura for their comments and constructive suggestions. He also benefited from valuable discussions with Dr. Yoshisuke Ueda on chaos.

Experiments and calculations in Chapter 4 were performed with the help of Messrs. Toshiyuki Okamoto and Kenji Komaki. Some figures were prepared by Mr. Hidenori Kawanishi. Mr. Takashi Sekiya read the manuscript critically. It is a pleasure to acknowledge their help and cooperation.

The author appreciates the help and the encouragements of Dr. Minoru Tsutsui and other staffs of Radio Atmospheric Science Center and Professor Kimura's group.

This work was partly supported by the Grant-in-Aid for Scientific Research from the Ministry of Education, Science, and Culture. He has been a recipient of a Sakkokai Foundation Fellowship (April 1982 - March 1984).

ABSTRACT

This thesis concerns with nonlinear behaviors of spin-related bistable and tristable systems.

In recent years there has been a substantial theoretical and experimental effort on optically bistable systems. An optically bistable system is a device which exhibits two distinct states of optical transmission. It has acquired much attention from the aspect of practical application as optical devices and also from the fundamental standpoint since it offers various nonlinear phenomena inherent in systems far from equilibrium.

It is shown, in this thesis, that inclusion of light polarization leads to qualitatively new variations of the phenomena. Light polarization is connected to the atomic spins of the medium. So far no works on polarization effects in optical bistability have been made. Here two types of such spin-related optical system are proposed and studied.

The first system is a Fabry-Perot cavity filled with atoms with degenerate Zeeman sublevels in the ground state. It is found that for linearly polarized incident light, the high transmission state is doubly degenerate with respect to the output light polarization; one is almost right-circularly polarized (σ_+ state) and the other is almost left-circularly polarized (σ_- state). In the low transmission state, the output remains linearly polarized (linear state). Therefore the three states coexist and we call the phenomenon optical tristability. In the σ_+ (σ_-) state, the atomic spins are oriented parallel (antiparallel) to the propagation direction of the incident light, whereas in the linear state, they

ABSTRACT

v

are random. When we increase the intensity of the linearly polarized incident light, at a critical point, the linear state becomes unstable and a discontinuous transition to the σ_+ or σ_- state takes place with equal probabilities. The symmetry of the system with respect to the polarization is spontaneously broken. This is a result of a competitive interaction of the σ_+ (right-circularly polarized) and σ_- (left-circularly polarized) light beams through optical pumping.

Bifurcations which appear when the input intensities of σ_+ and σ_- components are changed independently are also investigated. It is found that the bifurcation structure can well be understood in context of a butterfly catastrophe.

Next the dynamical property of the system is studied. It is shown that when we apply a static magnetic field transversely to the optical axis, self-sustained precession of the spin polarization occurs. Correspondingly, the σ_+ and σ_- components of the transmitted light are modulated at about the Larmor frequency. It is also shown that a modified Bloch equation which describes the motion of the spin polarization in the cavity can be reduced to the van der Pol equation.

The second system we propose uses the same medium as the first one but has no optical cavity. The optical system is composed of a cell containing the atoms, a $\lambda/8$ plate, and a mirror. The feedback is realized by the optically induced Faraday effect. The system exhibits a pitchfork bifurcation which breaks the symmetry as the input intensity is increased. Namely, the symmetry breaking is of a supercritical type, whereas in the first system it is of a subcritical type. This system has also two input parameters and a cusp catastrophe appears when they are changed independently. It

is also found that in the presence of a transverse magnetic field, self-sustained spin precession takes place.

The static behavior of the second system is confirmed experimentally by using Na vapor and a multimode dye laser.

Chaotic (or turbulent) phenomena in optical bistability is also investigated. Chaotic oscillation occurs when a delay time in the feedback loop is longer than the response time of the medium as predicted by Ikeda. The delay-induced chaos in a simple and familiar acoustic system is studied experimentally. It is an acoustic analogue of optically bistable systems. The system goes over into chaotic state after some cascades of period-doubling bifurcations as we increase the loop gain.

The delay-induced chaos in the second optical system is investigated. Particular attention is paid on the symmetry of the solutions with respect to the polarizations. The output of the system bifurcates in the following way as the input light intensity increases: (1) symmetric steady state, (2) asymmetric steady state, (3) asymmetric periodic oscillation, (4) asymmetric chaos, (5) symmetric chaos. The first bifurcation is a well-known symmetry-breaking transition. It is shown that the last bifurcation through which the symmetry is recovered can be viewed as a crisis of chaos, which has been defined by Grebogi et al. as a sudden change of strange attractor. By changing system parameters, we find three distinct types of the crises in the experiment with an electronic circuit which simulates the differential-difference system equation. Before and after the crises, waveforms characteristic of each type is observed. In a simple two-dimensional-map model, we can find the three types of crises. It is also found that the types of crises are determined by the nature

of unstable fixed (or periodic) points which cause the crises by colliding to the chaotic attractors. The symmetry-recovering crises seem to be general phenomena appearing in nonlinear systems with some symmetries.

CONTENTS

ACKNOWLEDGEMENTS

ABSTRACT

CHAPTER 1	GENERAL INTRODUCTION	1
1.1	Optical Bistability	1
1.2	Optical Pumping and Spin Polarization	5
1.3	Outline of Present Work	10
CHAPTER 2	OPTICAL TRISTABILITY	14
2.1	Introduction	14
2.2	Theory	16
2.3	Symmetry-Breaking Bifurcation	19
2.4	Butterfly Catastrophe	23
2.5	Experimental Evidence	27
2.6	Conclusions and Discussion	28
CHAPTER 3	SELF-SUSTAINED SPIN PRECESSION	30
3.1	Introduction	30
3.2	Modified Bloch Equation	31
3.3	Self-Sustained Spin Precession	35
3.4	Experimental Evidence	39
3.5	Conclusions and Discussion	41
CHAPTER 4	OPTICALLY BISTABLE SYSTEM WITHOUT A CAVITY	43
4.1	Introduction	43
4.2	Optical System and Stable States	45
4.3	Self-Pulsing by Spin Precession	54

CONTENTS

ix

4.4	Experiment with Sodium Vapor	57
4.5	Conclusions and Discussion	62
CHAPTER 5	CHAOS IN AN ACOUSTIC SYSTEM	65
5.1	Introduction	65
5.2	A Differential-Difference Equation	66
5.3	Experimental Setup	68
5.4	Experimental Results	70
5.5	Comparison with Theory	72
5.6	Concluding Remarks	76
CHAPTER 6	SYMMETRY-RECOVERING CRISES IN OPTICAL BISTABILITY	77
6.1	Introduction	77
6.2	System Equation	79
6.3	One-Dimensional-Map Model	82
6.4	Simulation by Analog Circuit	84
6.5	Two-Dimensional-Map Model	88
6.6	Conclusions	98
CHAPTER 7	CONCLUSIONS	101
APPENDIX A	OPTICAL PUMPING IN FOUR-LEVEL ATOMS	105
A.1	Optical Pumping in Four-Level Atoms	105
A.2	Spatially Averaged Bloch Equation	114
A.3	Light Propagation in a Spin-Polarized Medium	115
APPENDIX B	CATASTROPHE	118
B.1	Thom's Theorem	118
B.2	Examples	121

B.3	Remarks	125
APPENDIX C	BIFURCATION IN MODIFIED BLOCH EQUATION	129
C.1	Liénard's Method	129
C.2	Takens' Normal Form	130
APPENDIX D	CHAOS	132
D.1	Introduction	132
D.2	Roads to Chaos	135
D.3	Bifurcations in One-Dimensional Maps	137
APPENDIX E	CLASSIFICATION OF A FIXED POINT OF 2D MAP	140
REFERENCES		141

CHAPTER 1

GENERAL INTRODUCTION

This thesis concerns with some of nonlinear phenomena in spin-related optically bistable and tristable systems. The present chapter contains an introduction to the topics which were investigated. A short review of theoretical and experimental studies on optical bistability is presented. A brief description on nonlinear effects caused by laser optical pumping is given because they plays an important role throughout this work. Finally the outline of this work is presented.

1.1 Optical Bistability

Recently a new class of optical systems which may have two (or more) distinct output states for a given input state has drawn intense interests. Such a system is called an optically bistable (or multistable) system. It will potentially be used as optical logic devices for ultra-high-speed signal processing and communications. In principle, very fast switching with low power consumption and two-dimensional parallel processing are possible.

Generally an optically bistable system is realized when the transmitted light of a nonlinear medium is fed back to itself by some means. If the feedback is through some electronic circuits the system is called "hybrid," whereas an all-optical system is called "intrinsic." The most popular intrinsic system is an optical cavity filled with a nonlinear dispersive medium. Figure 1.1 shows the principles of operation (Smith and Tomlinson, 1981). Curves A_1

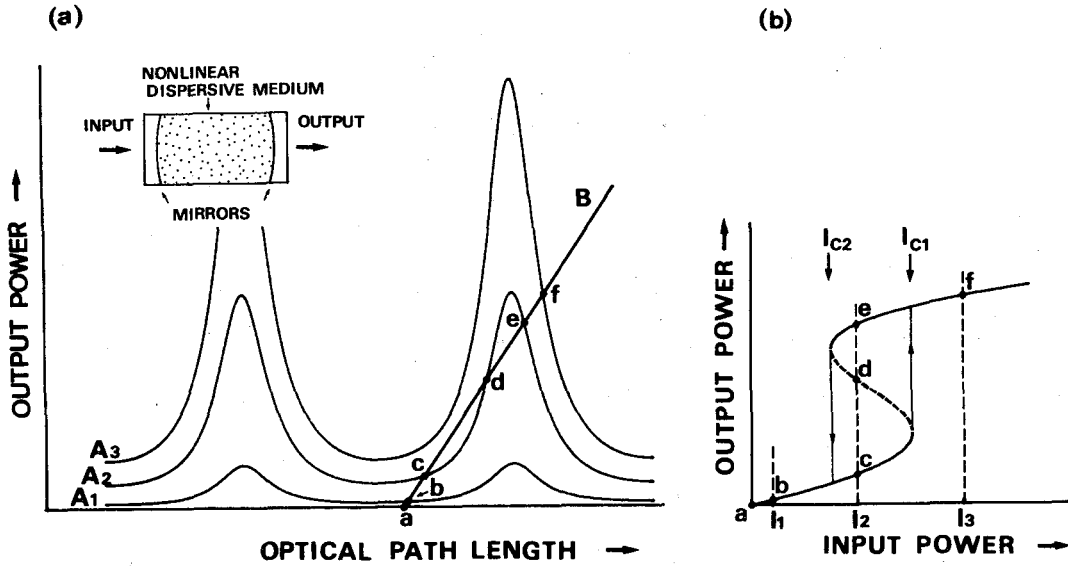


Fig. 1.1 Principle of operation of an optically bistable device which utilizes a Fabry-Perot interferometer and a nonlinear dispersive medium. (a) Curves A_i : interference patterns of Fabry-Perot cavity for input power I_i ($I_1 < I_2 < I_3$). Curves B: variation of the effective path length of the medium under the influence of the intracavity laser field. Crossing points a ~ b: equilibrium states of the system. (b) Plots of equilibrium points vs input power.

show fringe patterns of the optical cavity for the incident light of intensities I_i . The abscissa represents the effective optical length of the cavity and the coordinate represents the output optical power. The output power is proportional to the input power, if the optical path length is fixed. The optical power in the cavity is proportional to the output power. Curve B represents the variation of the optical length of the medium under the influence of intracavity light, which means the dispersion, or the refractive index is dependent on the intensity of light propagating through it. The crossings of Curves A_i and B correspond to equilibrium points of the system. We plot the equilibrium output optical power for various values of I_i and obtain Fig. 1.1(b). The

portion of negative slope is found to be unstable. The upper and lower stable branches correspond to the transparent and opaque states respectively. As the input light intensity is increased from zero, at $I = I_{c1}$, a sudden jump from the lower branch to the upper one takes place. Inversely the input is decreased passing I_{c2} , the output jumps back to the lower branch. Between I_{c2} and I_{c1} , two stable states coexist. By modifying the system parameters, we can obtain devices which have a differential gain or a switching characteristic.

Optical bistability is firstly proposed by Szöke et al. (1969). Experimentally Gibbs et al. (1976) successfully demonstrated the effect by using sodium vapor as a nonlinear dispersive medium.

Under certain conditions a part of upper branches becomes unstable and the output of the system shows oscillatory behavior. The phenomenon is called "self-pulsing." Possibility of self-pulsing in optical bistability was firstly discussed by Szöke et al. (1969). Theory and a hybrid optical bistable experiment, both by McCall (1978), showed that a bistable device can pulsate when the nonlinearity has two contributions of opposite sign and different time constants. The experimental evidence in an intrinsic device was given by Jewell et al. (1982) in a GaAs etalon, where the thermal and the electronic contributions to the refractive index was utilized. Even in simpler media without the above-mentioned character, self-pulsing is possible if we take the light-propagation effects into account. The stability analysis for the steady state solutions to the Maxwell-Bloch equation was performed by Bonifacio and Lugiato (1978b) and it was shown that there is a part of the curve in Fig. 1.1(b) with positive slope in

which some off-resonant cavity modes become unstable.

More recently, Ikeda (1979) and Ikeda et al. (1980) investigated the dynamics of a ring cavity containing a nonlinear dielectric medium and predicted that the instability in such a system gives rise to a turbulent behavior, or so-called chaos. This instability comes from delayed feedback of the light transmitted through the medium. They showed that chaos appears only when the round-trip time t_R of light is longer than the response time γ^{-1} of the medium. Subsequently Gibbs et al. (1981) succeeded in the first experimental observation of the phenomena in a hybrid optical device. Chaos in an intrinsic device was observed by Nakatsuka et al. (1983) where optical fiber was used as a nonlinear medium. Later on, Ikeda et al. (1982) pointed out even in the cases $t_R \ll \gamma^{-1}$, chaotic pulsation is possible and interpreted it as a self-induced Rabi nutation of the electric field vector.

Anyway their proposal has renewed interest in optical examples of chaotic dynamics. All of the above-mentioned phenomena in bistable systems, such as multiplicity of the state, a hysteresis loop, a sudden change of state for a continuous change of the parameters, self-pulsing, and chaos, are distinctive features of a nonlinear dynamical system. Thus optical bistability attracts much attentions from a fundamental point of view and is now a theoretical model to study nonlinear phenomena. Optical devices are rather simple by comparison to the other systems such as hydrodynamical and biophysical models. As such, comparison of theory with experiment is sometimes more straightforward than in other cases.

It should be noted that one can add moderate complexities to optical systems by taking into account various effects and can find

qualitatively new phenomena. For example, Moloney et al. (1982) showed that the light beam of a bistable device, which is called "spatial ring," may exhibit coherent spatial structure spontaneously. The inclusion of the transverse profile of the laser beam causes new phenomena which are similar to those in hydrodynamics.

1.2 Optical Pumping and Spin Polarization

Before describing optical pumping itself, we mention its relation to laser nonlinear spectroscopy. Nonlinear spectroscopy is now a very powerful tool to study atomic and molecular structures with high resolution and high sensitivity. The nonlinearity is brought about when the population distribution in the atomic states is changed appreciably from the thermal equilibrium by laser light with high intensity. The coherency or the monochromaticity of laser enables us to modify the population distribution selectively and to create atomic coherences. We can not only select the atomic internal state but also its velocity and coordinate. Intense laser light can populate highly excited states efficiently against the fast relaxation to the ground state.

Before the advent of a laser, a method to create the population changes by conventional light sources, such as atomic resonance lamps, was proposed and various techniques has been developed. The term "optical pumping" indicates these techniques in its narrower sense. One of the key concepts of optical pumping is the use of polarization of light. Irradiation of polarized light can create an orientation or an alignment of the atoms, namely the population difference in the magnetic sublevels. We can

see a germ of nonlinear laser spectroscopy. Furthermore, the laser itself can be viewed as one of the resulting products from a development of optical pumping.

In order to describe the optical pumping process, we shall use

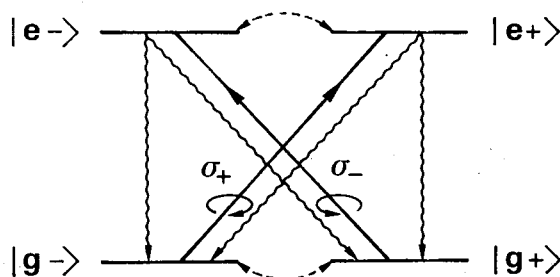


Fig. 1.2 Energy level diagram of atoms with $J = 1/2 \rightarrow J = 1/2$ transition. Real lines: excitation by σ_+ (right-circularly polarized) and σ_- (left-circularly polarized) light. Wavy lines: spontaneous and collisional decay. Dashed lines: spin relaxation.

a simplified atomic model shown in Fig. 1.2. The excited state with a total angular momentum $J_e = 1/2$ is coupled to the ground state with $J_g = 1/2$ by optical transitions. Such a configuration can be seen in the D_1 line ($^2P_{1/2} \rightarrow ^2S_{1/2}$) of an alkali metal, if we neglect the effects of the nuclear spin. The $m_j = \pm 1/2$ levels of the ground state are represented as $|g\pm\rangle$. For the excited state, $|e\pm\rangle$ are defined similarly. The selection rule of an electric-dipole transition is $\Delta m_j = +1$ for σ_+ (right-circularly polarized) light and $\Delta m_j = -1$ for σ_- (left-circularly polarized) light. In the absence of light the levels $|g+\rangle$ and $|g-\rangle$ are equally populated. Suppose we irradiate an ensemble of such atoms with σ_+ light. Only the atoms in the $|g-\rangle$ level are excited to the $|e+\rangle$ level by the presence of the selection rule. Some of which fluoresce and return to the level $|g-\rangle$ and the others to $|g+\rangle$. If

this process is repeated, a considerable part of atoms is transferred from the $|g\rangle$ to the $|g+\rangle$ level. The final relative population will be determined by such parameters as the pumping light intensity, relative transition probabilities, and spin-relaxation time of the ground state. Generally, the relaxation time is relatively long (a few milliseconds or longer) and a large population difference can be created by weak light. The population difference corresponds to the orientation of the angular momentum or the magnetic momentum of the atoms.

The process described above is a typical example of optical pumping. It should be noted that owing to the light polarization, a kind of selection as in the nonlinear spectroscopy becomes possible.

Use of lasers in the optical pumping experiments adds new features. For example, polarization spectroscopy (Wieman and Hänsch, 1976), which utilizes optical pumping to the full, is now a very useful method in analyzing complex atomic or molecular structures. Aside from spectroscopic use, laser optical pumping was found to exhibit various interesting phenomena in nonlinear optics, such as self-focusing of a weak light beam (Yabuzaki et al., 1982), repulsion of two circularly-polarized beams of opposite polarizations, (Tam and Happer, 1977), break up of a linearly polarized beam into two coherent beams of opposite circular polarization (Tam and Happer, 1977), and propagating wave front generated by laser pumping (Bhaskar et al., 1979). Our studies are on these lines.

To close this section we discuss on the nonlinearities caused by optical pumping. Consider two extreme cases pictured in Fig. 1.3. In the case (a), the atoms are not optically pumped and the

(a) NO PUMPING

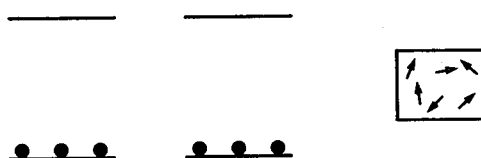
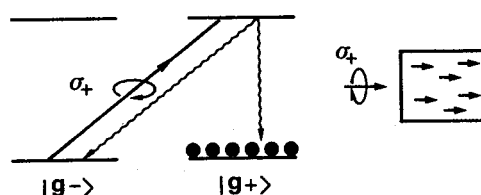
(b) σ_+ PUMPING

Fig. 1.3 Population distribution (a) in the absence of pumping light, and (b) under the irradiation of intense σ_+ light. In the case (a), the ensemble of atoms can be considered as an isotropic medium, whereas in (b), the circular dichroism and birefringence appear.

$|g+\rangle$ and the $|g-\rangle$ levels are equally populated. The absorption coefficients α_+ (α_-) and the incremental refractive indices $n_+ - 1$ ($n_- - 1$) for σ_+ (σ_-) light are proportional to the populations of $|g+\rangle$ and $|g-\rangle$. So the relations

$$\alpha_+ = \alpha_- = \alpha, \quad (1.1a)$$

$$n_+ = n_- = n, \quad (1.1b)$$

hold, where α and n are constants. In the case (b), all atoms are pumped to the $|g+\rangle$ level by intense σ_+ light and the optical characteristics are changed as

$$\alpha_+ = 0, \quad \alpha_- = 2\alpha, \quad (1.2a)$$

$$n_+ = 1, \quad n_- = 1 + 2(n - 1). \quad (1.2b)$$

We see the medium shows circular dichroism and circular birefringence. We should firstly note that the pumping by the σ_+ light changes the optical constants for itself via optical pumping. In other words, the atomic system acts as a nonlinear medium. Secondly, the pumping light also influences the propagation of σ_- light if it exists. Conversely, σ_- light will change the optical constants for σ_+ light. This interaction between the σ_+ and σ_- components of light and the nonlinearity play important roles in the phenomena treated in this work.

The process of optical pumping can well be described by the Bloch equation for the ground-state spin \vec{m} (Appendix A):

$$\frac{d\vec{m}}{dt} = \vec{m} \times \vec{Q}_0 - \Gamma_g \vec{m} - P_+(\vec{m} - \hat{z}) - P_-(\vec{m} + \hat{z}), \quad (1.3)$$

where \vec{Q}_0 , Γ_g , P_{\pm} , and \hat{z} represent the magnetic field, the spin relaxation rate, the σ_{\pm} light intensities, and the unit vector along the light propagation direction, respectively. When these parameters are constant, Eq. (1.3) is an autonomous (time-independent) linear equation which has one equilibrium point. The equilibrium point is stable and all solutions are attracted to this point exponentially as time passes. Although the position of the equilibrium point can be changed by adjusting the parameters, no qualitative change does not occur. If, however, P_+ and P_- are functions of \vec{m} , then Eq. (1.3) becomes nonlinear and qualitatively new phenomena can be expected. Such situation can be realized by detecting the spin polarization by some means and feeding it back to the light intensities P_{\pm} . Two types of feedback are used in this thesis; one utilizes the interference in a Fabry-Perot cavity

and the other uses the optically induced Faraday effect. In both cases, the dependence of dispersion (or refractive index) on the spin \vec{m} plays an essential role.

1.3 Outline of Present Work

In this thesis we treat two optical systems both of which utilize the nonlinearity and the coupling between the σ_+ and σ_- light through optical pumping. The first system treated in Chapters 2 and 3 is composed of a Fabry-Perot cavity and an intracavity cell filled with atoms which have degenerate Zeeman sublevels in the ground state. The second system in Chapters 4 and 6 is also of intrinsic type as the first one and uses the same atomic system, but has no optical cavity. The feedback is realized by the optically induced Faraday effect. Chapter 6 is devoted to the description of chaotic behaviors seen in the no-cavity system. Chaos appears when a delay in the feedback exists. Preparatory to it, in Chapter 5, some general aspects of the delay-induced chaos are presented. We also present experimental results on chaotic oscillation observed in a simple and familiar acoustic system. The system equation is essentially the same as that for the optically bistable system.

Here we outline the content of each chapter. Chapter 2 is devoted to the description of the static behavior of the first system. At the beginning the mathematical model for the atomic system is set up. The model is used throughout this work. From the steady state solution the bifurcation structure is investigated. The marked phenomenon predicted to occur in this system is optical tristability. In the case of linearly polarized

incident light the three states can be characterized as follows: (1) The light in the cavity is linearly polarized, (2) it is essentially right-circularly polarized (σ_+ state), and (3) it is essentially left-circularly polarized (σ_- state). In the σ_+ (σ_-) state, the atomic spins are oriented parallel (anti-parallel) to the direction of the incident light beam. The symmetry-breaking bifurcation from the linear state to the σ_+ or σ_- states occurs when the incident light intensity increases.

The bifurcations which appear in general cases where the σ_+ and σ_- components of the input light are changed independently are also investigated. From the aspects of Thom's novel theory, it is interpreted as a butterfly catastrophe. Finally some extensions of the tristable system and new predictions made by other authors are reviewed. The experimental evidence of the optical tristability by Cecchi et al. is also reviewed.

Chapter 3 is devoted to the dynamical behavior of the tristable system. It is predicted that a new type of self-pulsing is induced by a magnetic field applied perpendicularly to the optical axis. The mechanism underlying is the self-sustained spin precession about the magnetic field. The σ_+ and σ_- components of the output light are modulated alternately. The oscillation frequency can be controlled by the strength of the magnetic field. It is shown that the system can be described by the van der Pol equation. An experimental evidence shown by Mitschke et al. is also represented.

In Chapter 4, we propose a spin-related bistable system without cavity. The system utilizes the optically induced Faraday rotation as the feedback mechanism. Use of no cavities relaxes the condition for the light source that it should operate on a single

mode and the frequency should be tuned at a definite part of the cavity fringe. An incoherent light source may be enough if other conditions are satisfied.

It is shown that in the case of linearly polarized incident light the system exhibits a pitchfork bifurcation which breaks the polarization symmetry and no hysteresis appears. In other words, the symmetry breaking bifurcation is of a supercritical type, while in the tristable system it is of a subcritical type (Joseph, 1981). Considering the difference between σ_+ and σ_- components of the incident light or an asymmetry of the system as a parameter in addition to the input intensity, we can see a cusp catastrophe.

Self-pulsing as in Chapter 3 can be expected to exist in this system. The nonlinearity is simpler than before. So the conditions for the oscillation can be written down explicitly.

The experiments were carried out to examine the static behavior of this system. Sodium vapor in a heat-pipe oven was used as the nonlinear medium, to which the multimode dye laser tuned on a wing of the D_1 line was applied. The operation of the proposed system was verified experimentally.

Chapter 5 is devoted to some general aspects for chaotic phenomena. Our attention is focussed on the delay-induced chaos in optical bistability. The delay is caused by the propagation of feedback light. To get intuition, an experiment in a simple acoustic system was carried out. The system equation is essentially the same as that for the optical system. There we found that the system passes the period-doubling route to chaos as seen in various kind of systems.

In Chapter 6, we investigate the delay-induced chaos in the optical system treated in Chapter 4. The most striking phenomena

is the bifurcation which recovers the polarization symmetry broken by the symmetry-breaking bifurcation. The new bifurcation lies between an asymmetric chaos and a symmetric chaos. We found some types of such bifurcations by changing the system parameters. An attempt to explain the underlying mechanism for each type is presented by using a mathematical model.

CHAPTER 2

OPTICAL TRISTABILITY

2.1 Introduction

In this chapter we study on an optical system composed of a Fabry-Perot cavity and an intracavity cell which contains atoms with degenerate Zeeman sublevels in the ground state. The medium shows polarization anisotropy in the nonlinear regime as shown in Chapter 1. So we should treat the optical field as a vector and the dielectric susceptibility of the medium as a tensor. Although many studies have been made on optical bistability, none of them take into account the vectorial nature of the optical field nor the tensorial nature of the medium. We show here that inclusion of such natures brings qualitatively new phenomena. The most remarkable feature of the system is optical tristability which is the central subject of this chapter. For linearly polarized incident light the system shows a hysteresis as in the ordinary bistable system when we observe only the output light intensity. If, however, we also observe the polarization state, the high transmission branch appears to be degenerate with respect to the right- and left-circular polarizations. We have therefore three stable states; the linear (low transmission) state, the almost right circular (high transmission) state, and the almost left circular (high transmission) state. The three states are abbreviated to linear, σ_+ , and σ_- states. As easily seen, the transition to the high transmission states, σ_+ or σ_- , is a symmetry breaking one, which is a very important notion in a non-

equilibrium dynamical system. Generally, a non-equilibrium system acquires a spatial or temporal structure spontaneously through symmetry breaking bifurcations (Nicolis and Prigogine, 1977).

The symmetry breaking can be connected to the atomic state. In the σ_+ state (σ_- state), the atomic spins are oriented parallel (anti-parallel) to the direction of the incident light beam and in the linear state, they are random. Above the critical point for the symmetry breaking, the medium behaves as if it were a gaseous ferromagnetic material.

In Sec. 2.2, we present the state equation for the optical tristable system. The equation is obtained by coupling the steady solution of the rate equation for the atomic system and the input-output characteristics of the Fabry-Perot cavity. In Sec. 2.3 the conditions for the symmetry-breaking bifurcation are examined by the stability analysis of a trivial symmetric solution. The numerically obtained double hysteresis loop is also presented.

It should be noted that this system has two independent input parameters; right- and left-circularly polarized components of the incident light. In Sec. 2.4 we investigate the bifurcations which appear in general cases where the two parameters are varied independently. The bifurcations occur in somewhat complicated manners. The parameter space is divided into mono-, bi-, and tri-stable regions. It is found the bifurcation scheme can well be understood in context of the catastrophe theory (Thom, 1975). In Appendix B we describe the Thom's theory on the classification of elementary catastrophes. It is a deep result obtained from purely mathematical discussions. So all that we can do is to explain it intuitively from a physical point of view. In Sec. 2.4 it is shown that our system is a good example of the butterfly catastrophe

which is one of the seven elementary catastrophes.

In Sec. 2.5 we propose an experiment to observe optical tristability. According to the proposal, Cecchi et al. (1982) performed the experiment and observed the phenomena by using sodium vapor as a nonlinear medium. A brief summary of their experiment is given.

2.2 Theory

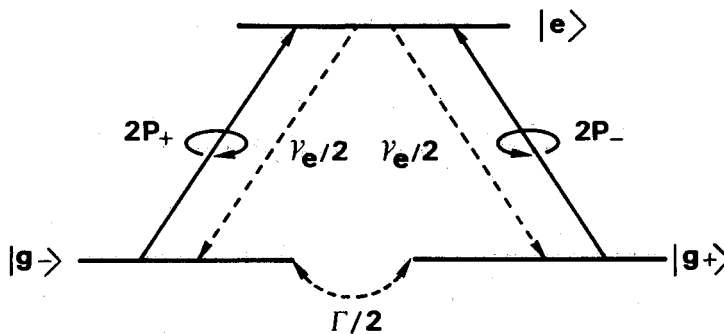


Fig. 2.1 Simplified atomic level scheme.

We consider atoms with energy levels indicated in Fig. 2.1. The spin-up level $|+\rangle$ and spin-down level $|-\rangle$ in the ground state are degenerate and have equal number densities $N_+ = N_- = N/2$ in the absence of light beams, where N is the total atomic density. The optically excited levels are represented by a single level $|e\rangle$, which is possible when these levels are completely mixed by atomic collisions. In such a three-level system, the effect of optical pumping is described by the rate equations for N_+ and N_- (Appendix A):

$$dN_{\pm}/dt = -P_{\mp}N_{\pm} + P_{\pm}N_{\mp} - (\Gamma/2)(N_{\pm} - N_{\mp}), \quad (2.1)$$

where Γ is the spin relaxation rate, and the pumping rate P_{\pm} have been assumed to be smaller than the decay rate γ_e of the excited state, which therefore has negligible population. The rates P_{\pm} are expressed in terms of the light intensities (photon flux) I_{\pm} and the absorption cross-section σ by $P_{\pm} = (1/2)\sigma I_{\pm}$. For homogeneously broadened medium, the absorption cross-section σ for monochromatic light of the frequency ω is given by

$$\sigma = \frac{4\pi p^2 \omega_0}{c\hbar} \frac{\gamma_{ab}}{\Delta^2 + \gamma_{ab}^2}, \quad (2.2)$$

where p is the atomic dipole moment, γ_{ab} is the relaxation rate for optical coherence, ω_0 is the transition frequency, and $\Delta = \omega_0 - \omega$ is the atomic detuning.

The steady-state solutions of Eq. (2.1) are

$$N_{\pm} = \frac{\sigma I_{\pm} + \Gamma}{\sigma(I_{+} + I_{-}) + 2\Gamma} N. \quad (2.3)$$

With use of Eqs. (2.2) and (2.3) the absorption coefficients α_{\pm} and the wavenumbers k_{\pm} for the σ_{+} and σ_{-} light are

$$\alpha_{\pm} = (\sigma/2)N_{\mp}, \quad (2.4)$$

$$k_{\pm} = k_0 + (\sigma/2)(\Delta/\gamma_{ab})N_{\mp}, \quad (2.5)$$

where k_0 is the wavenumber in a vacuum (see Sec. A.3). For simplicity we will neglect the absorption losses by taking relatively large values of $|\Delta|$. Inclusion of absorption losses will not change the essential features of our discussion.

The transmission characteristics of a Fabry-Perot cavity which includes a dispersive medium are derived as follows. Two mirrors

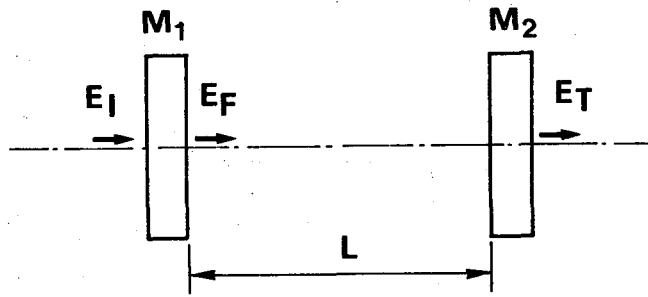


Fig. 2.2 Cavity system.

with a reflectivity R are separated by a length L . The field amplitudes E_I , E_F , and E_T at positions indicated in Fig. 2.2 satisfy the following boundary conditions:

$$E_F = \sqrt{1 - R} E_I + R E_F e^{-2ikL} \quad (2.6)$$

$$E_T = \sqrt{1 - R} E_F e^{-ikL}, \quad (2.7)$$

where k is the wavenumber. From Eqs. (2.6) and (2.7) we get

$$|E_T|^2 = (1 - R)^2 |E_I|^2 [1 + R^2 - 2R \cos 2kL]^{-1}. \quad (2.8)$$

The relation is easily extended to the case where circular birefringence, namely the difference between k_+ and k_- , exists:

$$I_{T\pm} = T^2 I_{I\pm} [1 + R^2 - 2R \cos 2k_{\pm} L]^{-1}, \quad (2.9)$$

where $I_{I\pm}$ are the incident light intensities, $I_{T\pm}$ are the transmitted light intensities, and $T = 1 - R$ is the transmissivity of the mirrors. The wavenumbers k_{\pm} are assumed to be constant over the entire cavity length L because standing-wave structure of the spin-polarized atoms which have relatively long relaxation time is washed out by their thermal motion. The moving atoms are pumped by

mean-field intensities I_{\pm} in the cavity which are related to $I_{T\pm}$ by (see Sec. A.2)

$$I_{\pm} = (I_{T\pm}/T)(1 + R). \quad (2.10)$$

With use of Eqs. (2.3) and (2.10) the expressions (2.5) for k_{\pm} become

$$k_{\pm} = k_0 + 2\kappa(X_{\mp} + 1)/(X_{+} + X_{-} + 2), \quad (2.11)$$

where $\kappa = (\sigma/2)(\Delta/\gamma_{ab})(N/2)$ is the linear dispersion and $X_{\pm} = (\sigma/T)I_{\pm}$ are the normalized transmitted intensities. Substitution of Eq. (2.11) into Eq. (2.9) gives the following coupled nonlinear equations which relate the transmitted light intensities to those of incident ones:

$$X_{\pm} = \frac{TY_{\pm}}{1 + R^2 - 2R \cos(2[k_0 + 2\kappa(X_{\mp} + 1)/(X_{+} + X_{-} + 2)]L)}, \quad (2.12)$$

where we introduced the normalized incident light intensities $Y_{\pm} = (\sigma/T)(1 + R)I_{I\pm}$.

The variables X_{+} and X_{-} are not independent because k_{+} and k_{-} in Eq. (2.11) are connected by the relation $k_{+} + k_{-} = 2(k_0 + \kappa)$. In fact, if we derive the equation for atomic variables, it contains only m_z as will be seen later. In this chapter, however, we will use Eq. (2.12) mainly.

2.3 Symmetry-Breaking Bifurcation

We consider, at first, the case where the incident light is linearly polarized, namely, $Y_{+} = Y_{-} = Y$. Equation (2.12) gives trivial solutions:

$$X_+ = X_- = X, \quad (2.13)$$

where $X = \tau Y$ and

$$\tau = T(1 + R^2 - 2R \cos[2(k_0 + \kappa)L])^{-1} \quad (2.14)$$

is the transmissivity of the Fabry-Perot cavity for weak-field limit $X_+, X_- \ll 1$. As for the transmitted field amplitudes and phases of both circularly polarized components, the solutions (2.13) are symmetric, and the polarization of resultant transmitted light remains linear. The nonlinearity nor the coupling between the two circularly polarized light may seem to play no role in the solutions (2.13), but makes them unstable under some conditions.

The stability of the solutions (2.13) can be examined by calculating the differential gain which diverges at critical points where stable solutions become unstable under a continuous change of parameters (Gibbs et al., 1979). (The analysis can be done more straightforwardly by using the dynamical equation for the atomic variable. See Chapter 3.) Expanding the light intensities around the solutions (2.13) as $Y_{\pm} = Y + y_{\pm}$, $X_{\pm} = X + x_{\pm}$, and substituting into Eq. (2.12), we obtain linearized equations:

$$x_+ + x_- = \tau(y_+ + y_-), \quad (2.15)$$

$$x_+ - x_- = \xi_D(y_+ - y_-), \quad (2.16)$$

where $\xi_D = \tau/(1 - 2\pi\tau)$ is the differential gain for the difference between both light intensities, and π is a parameter representing the strength of nonlinearity which is given by

$$\pi = (2R/T)\kappa L[X/(X + 1)] \sin[2(k_0 + \kappa)L]. \quad (2.17)$$

At the critical point $\eta = \eta_{c1} = 1/(2\tau)$, ξ_d diverges. In the region $\eta < \eta_{c1}$, which includes the linear case $\eta = 0$, the solutions (2.13) are stable; hence in the region $\eta > \eta_{c1}$ they are unstable.

By using Eqs. (2.14) and (2.17), the unstable condition is written down explicitly:

$$\cos[2(k_0 + \kappa)L] + 2\kappa L \frac{X}{X+1} \sin[2(k_0 + \kappa)L] > \frac{1+R^2}{2R}. \quad (2.18)$$

Consider the case where the inequality (2.18) is satisfied in the limit $X \rightarrow \infty$ by choosing adequate values of k_0 , κ , L , and R . When the incident light intensities are small enough, namely, $X = \tau Y \sim 0$, the inequality (2.18) is not satisfied because the left-hand side is less than unity, whereas the right-hand side is greater than unity for $0 \leq R \leq 1$. Below the critical value X_{c1} ($= \tau Y_{c1}$) which satisfies the equation corresponding to the inequality (2.18), the symmetric solutions (2.13) are stable. At the point $Y = Y_{c1}$ symmetry-breaking transition occurs and for $Y > Y_{c1}$ only unsymmetric solutions are stable.

To obtain the unsymmetric solutions we solved Eq. (2.12) numerically. By expressing Eq. (2.12) as $X_{\pm} = f_{\pm}(X_+, X_-)$, the iterative procedure to get the stable solutions is written as follows:

$$X_{\pm}^{(n+1)} = \beta X_{\pm}^{(n)} + (1 - \beta) f_{\pm}(X_+^{(n)}, X_-^{(n)}), \quad (2.19)$$

where β represents the properly chosen convergence factor and satisfies $0 < \beta < 1$. Starting from an initial value $X_{\pm}^{(0)}$, the procedure is repeated until $X_{\pm}^{(n)}$ converge. In Fig. 2.3 we have plotted X_+ as a function of Y for $2k_0L = -\pi/2 + 2\pi M$ (M is an integer), $2\kappa L = \pi$, $R = 0.7$. With respect to X_- , the same curves are obtained but the upper branch corresponds to the lower one for

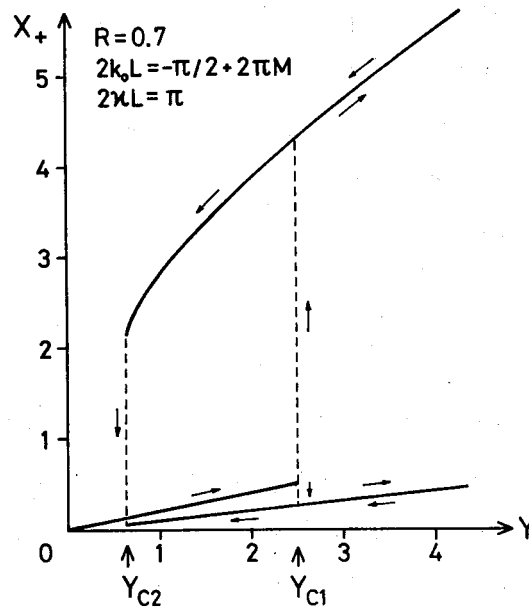


Fig. 2.3 Hysteresis cycles of right-circularly polarized transmitted light (X_+) in the case of linearly polarized incident light. The same curve is obtained for left-circularly polarized transmitted light (X_-) but the upper (lower) branch corresponds to the lower (upper) branch for X_+ . At $Y = Y_{c1}$, if X_+ jumps to the upper (lower) branch, then X_- necessarily jumps to the lower (upper) one and the σ_+ (σ_-) state is established.

X_+ , and vice versa. Increasing the incident light intensity one finds that, at the critical point Y_{c1} , X_+ jumps to the upper (lower) branch and X_- to the lower (upper) one. Above the point Y_{c1} the two stable state, i.e., σ_+ -dominant and σ_- -dominant states, are possible.

If, conversely, one decreases Y starting from values $Y > Y_{c1}$, one sees that, at the other critical point Y_{c2} , both X_+ and X_- jump back to the middle branch which represents the symmetric solutions (2.13). Thus in the region $Y_{c2} < Y < Y_{c1}$ there exist three stable solutions.

In Fig. 2.4 we show the bifurcation diagram with respect to

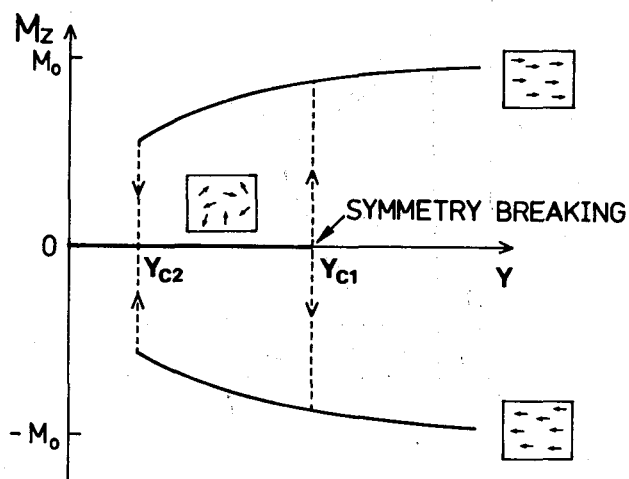


Fig. 2.4 Hysteresis cycles for the spin polarization M_z . Corresponding spin states are pictured schematically in boxes.

the atomic variable $N_+ - N_-$ or M_z , schematically. The z component M_z of the magnetization is proportional to $N_+ - N_-$ (Appendix A). In the linear state $N_+ = N_-$ because no optical pumping takes place. In the σ_+ (σ_-) state $N_+ - N_-$ takes positive (negative) values as a consequence of optical pumping due to the imbalance between the σ_+ and σ_- light components in the cell. As easily seen, in the σ_{\pm} state, the atomic spins are oriented parallel (antiparallel) to the optical axis, whereas in the linear state they are random.

2.4 Butterfly Catastrophe

We also calculated solutions to Eq. (2.12) for general cases $Y_+ \neq Y_-$. In Fig. 2.5 we have plotted critical points on the (Y_+, Y_-) plane schematically. At the critical points, the number of stable solutions changes. The single-stable, bistable, and

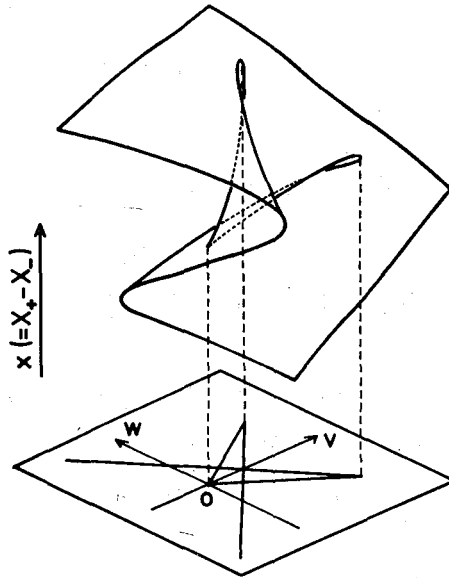


Fig. 2.6 Steady-state surface and bifurcation set for butterfly catastrophe ($t = t_0 < 0$, $u = 0$). The surface is doubly folded and is divided into three stable sheets.

upper (lower) part of the surface corresponds to the σ_+ (σ_-) dominant state and the intermediate part corresponds to the compromised state.

For linearly polarized incident light, the control variables move along the line $w = 0$ in Fig. 2.5 as the incident light intensity is varied and meet the two critical points at $Y = Y_{c1}$ and $Y = Y_{c2}$. In cases where incident light is circularly polarized, control line passes through the regions S , B_+ (B_-), and S_+ (S_-). This corresponds to the ordinary optical bistability, which has been studied in detail by Agrawal and Carmichael (1979) in the context of a cusp catastrophe. In that case, the potential V is represented by a quartic polynomial including two control parameters.

In order to see how the butterfly appears in our system, we

investigate the system equation analytically. We use the Bloch equation, which will be introduced in Chapter 3, in stead of the system equilibrium equation (2.12).

$$dm_z/dt = -(\Gamma + P_+ + P_-)m_z + (P_+ - P_-) \quad (2.21)$$

$$P_{\pm} = T[1 + R^2 - 2R \cos 2(k_0 + \kappa(1 \mp m_z))]^{-1} Q_{\pm}, \quad (2.22)$$

where $m_z = (N_+ - N_-)/N$ and $Q_{\pm} = (1/2)\sigma(1 + R)I_{I\pm}$ are the normalized incident light intensities. Representing Eq. (2.22) as $P_{\pm} = \tau_{\pm}(m_z)Q_{\pm}$ and expanding into Taylor series, we have

$$P_{\pm} = (\tau_0 \pm \tau_1 m_z + \tau_2 m_z^2 \pm \tau_3 m_z^3 + \tau_4 m_z^4 \pm \tau_5 m_z^5)Q_{\pm}. \quad (2.23)$$

In the case of $Q_+ = Q_- = Q$, Eq. (2.21) becomes

$$dm_z/dt = 2[(-\Gamma + Q(\tau_1 - \tau_0))m_z + (\tau_3 - \tau_2)Qm_z^3 + (\tau_5 - \tau_4)Qm_z^5]. \quad (2.24)$$

The critical condition for the symmetry breaking can be written in this context as

$$Q_{c1}(\tau_1 - \tau_0) - \Gamma = 0. \quad (2.25)$$

When $Q < Q_{c1}$, $m_z = 0$ is stable and when $Q > Q_{c1}$, $m_z = 0$ is unstable. In the unstable region we must consider the higher order terms. Numerical calculation shows the coefficient $\tau_3 - \tau_2$ is positive for the parameter values used previously. This means inclusion of the m_z^3 term is insufficient. The coefficient $\tau_5 - \tau_4$ is negative and therefore we can eliminate the terms higher than m_z^6 . The singularity m_z^5 leads the butterfly catastrophe.

2.5 Experimental Evidence

Finally, we will estimate parameters for the experiment to realize the optical tristability in which sodium vapor is used as a dispersive medium. By filling He gas at pressure higher than 200 Torr as a buffer gas, γ_{ab} for D_1 line at 589.6 nm becomes larger than 2 GHz (McCartan and Farr, 1976), and we can neglect hole-burning effect and hyperfine pumping especially for off-resonant light. Furthermore, the buffer gas mixes the excited hyperfine and Zeeman structure completely. Thus the situation is very close to the model which we have used in this chapter. To satisfy the inequality (2.18), $2\kappa L$ must be of order of unity or larger, which can be achieved by choosing $N \sim 10^{12} \text{ cm}^{-3}$, $L = 10 \text{ cm}$, and $|\Delta| = 30\gamma_{ab}$. Then the absorption loss $2\alpha L$ is about 0.1 and will be neglected. The required optical power density of a cw dye laser is the order of 10 mW/mm^2 .

To verify the prediction described in this chapter, Cecchi et al. (1982) performed an experiment. They used the temperature-stabilized Na-filled Fabry-Perot interferometer with effective finesse ~ 6 . Sodium vapor density is $\sim 10^{12} \text{ cm}^{-3}$. The light source was a cw dye laser tuned on the high-frequency wing of the D_1 line. The detuning was about 1.5 GHz, because they used the Na cell containing the Ar buffer gas of relatively low pressure (1 - 23 Torr) which causes a small line broadening ($< 0.2 \text{ GHz}$). A weak magnetic field (few gauss) along the optical axis was applied to align the ground state spin. They analyzed the transmitted intensity with a quarter-wave plate followed by a Wollaston prism and recorded the σ_+ and σ_- components simultaneously. By modulating the input intensity (0 - 25 mW) with a triangular wave

at low frequency (12 Hz), they observed the curve corresponds to Fig. 2.3. They also scanned the input polarization from almost circular polarization to the opposite circular polarization and observed a hysteresis curve. The behavior is expected from Fig. 2.6, if we change parameters I_+ and I_- keeping $I_+ + I_-$ constant. Modulating the cavity length, they observed the cavity transmission function both σ_+ and σ_- output components. The dependence of the system behavior on the cavity length of mistuning may be understood, if we put forward the analysis in Sec. 2.4.

2.6 Conclusions and Discussion

We have investigated the static behavior of a Fabry-Perot cavity containing atoms with degenerate Zeeman sublevels in the ground state. It has been shown that when the intensity of the linearly polarized incident light is increased, a symmetry breaking bifurcation occurs at a critical level. Above the threshold, the output light is circularly polarized in either direction. The symmetry breaking is of a subcritical type and therefore a double-loop hysteresis appears. The behavior of the system can be interpreted in terms of the butterfly catastrophe, when we vary the right and left circular components of the input light independently.

The essential point of the phenomenon is a conflict of the two beams. We notice that the optical tristability can be realized by other methods; namely by replacing the σ_+ and the σ_- beams with a pair of conflicting light beams. In fact some examples are proposed. Walls et al. (1981), and Agrawal and Flytzanis (1981) showed that two beams with frequencies ω_1 and ω_2 interacting

through a two-photon transition $\omega_0 \sim \omega_1 + \omega_2$ induce tristability (See also Hermann and Walls, 1982). Kaplan and Meystre (1981) utilized two counter-propagating beams in a ring cavity, which interact via the nonlinear refractive index grating generated by themselves. They also suggested that the effect can be used to enhance the Sagnac effect by several orders of magnitude.

Different nonlinearities causes various bifurcations that have not been discussed in this chapter (Parigger et al., 1983; Poston et al., 1982; Savage et al., 1982; Areshv et al., 1983; Arecchi et al., 1983). Anyway, such two-parameter systems reveal the variety of bifurcations and may be applicable to functional devices.

CHAPTER 3

SELF-SUSTAINED SPIN PRECESSION

3.1 Introduction

We have shown in Chapter 2 that a Fabry-Perot cavity containing atoms with degenerate Zeeman sublevels in the ground state exhibits optical tristability. The phenomena are due to spin polarization in the ground state by optical pumping in the region of anomalous dispersion. In the case of linearly polarized incident light, the three states are characterized as follows: (i) the transmitted light (E_T) and the reflected light (E_R) are both linearly polarized (linear state), (ii) E_T is right-circularly polarized and E_R is left-circularly polarized (σ_+ state), and (iii) a state with opposite polarizations to the σ_+ state (σ_- state). When the incident light intensity exceeds a threshold level, the linear state becomes unstable and a symmetry-breaking transition to the σ_+ or σ_- states occurs. Above the threshold atomic spins are forced to orient parallel or antiparallel to the optical axis. This phenomenon can be considered as an example of self-circular-birefringence proposed by Tam and Happer (1977).

When static magnetic field transverse to the optical axis is applied, the spontaneous magnetization begins to precess about it. In general a precession of macroscopic magnetization is faded out by thermal relaxations unless it is driven by periodic external forces such as a radio-frequency magnetic field or a modulated light beam (Kastler, 1961). In the present paper we show that self-sustained precession is possible in our system without any

periodic external forces. According to the precession the circularly polarized components of the transmitted light are modulated regeneratively. It is a new type of self-pulsing in optical bistability (or multistability) and we may call it "magnetically induced self-pulsing."

Self-pulsing phenomena in an optically bistable system was proposed and demonstrated experimentally by McCall (1978). It is explained as a relaxation oscillation due to a medium having two opposing contributions to the nonlinear refractive index, which have different time responses each other. A similar relaxation oscillation was proposed by Szöke et al. (1969), although its period is determined mainly by cavity holding time. Light propagation effects in a ring cavity with nonlinear medium also induce instabilities, where the pulsing frequency is related to the frequency difference of the cavity modes (Bonifacio et al., 1979). In our system the frequency is determined by the Larmor frequency, namely, by the strength of the static magnetic field.

3.2 Modified Bloch Equation

We consider the same atomic system as in Chapter 2 except for an application of a static magnetic field. The atoms are optically pumped by right-circularly polarized light (σ_+) and left-circularly polarized light (σ_-) simultaneously. We can neglect the population of the excited state assuming the spontaneous decay is fast enough compared to the pumping rates. The atomic state can be characterized by the magnetization, or the spin-polarization \vec{M} in the ground state. The time evolution of \vec{M} can be described by the Bloch equation (Appendix A; Dehmelt, 1957).

$$\frac{d\vec{M}}{dt} = \gamma \vec{M} \times \vec{H}_0 - \Gamma \vec{M} - P_+(\vec{M} - \vec{M}_0) - P_-(\vec{M} + \vec{M}_0), \quad (3.1)$$

where γ and Γ are the gyromagnetic ratio and the spin relaxation rate of the ground state respectively. The third (fourth) term of the right-hand side of Eq. (3.1) represents the effect of optical pumping by the σ_+ (σ_-) component of the intracavity light. If the pumping rate P_+ (P_-) is large enough, all atoms are pumped to the state $m_j=1/2$ ($-1/2$) and maximum polarization \vec{M}_0 ($-\vec{M}_0$) along the optical axis is established. The pumping rates P_{\pm} are expressed in terms of the σ_+ and σ_- light intensities (photon flux) I_{\pm} and the absorption cross-section σ by

$$P_{\pm} = \frac{1}{2} \sigma I_{\pm}. \quad (3.2)$$

For a homogeneously broadened medium, the absorption cross-section σ for monochromatic light of the frequency ω is given by

$$\sigma = \frac{4\pi p^2 \omega_0}{c\hbar} \frac{\gamma_{ab}}{\Delta^2 + \gamma_{ab}^2}, \quad (3.3)$$

where p is the atomic dipole moment, γ_{ab} is the relaxation rate for the optical coherence, ω_0 is the optical transition frequency, and $\Delta = \omega - \omega_0$ is the atomic detuning. For simplicity we neglected effects of the static magnetic field H_0 on σ assuming the Zeeman frequency $\Omega_0 = \gamma H_0$ is small compared with the homogeneous width γ_{ab} .

Taking the light propagation direction along the z axis and the static magnetic field \vec{H}_0 along the y axis (Fig. 3.1), we obtain the equations for the normalized magnetization components $m_i = M_i/M_0$ ($i = x, y, z$):

$$\frac{dm_x}{dt} = -Q_0 m_z - (\Gamma + P_+ + P_-) m_x, \quad (3.4a)$$

$$\frac{dm_y}{dt} = -(\Gamma + P_+ + P_-) m_y, \quad (3.4b)$$

$$\frac{dm_z}{dt} = Q_0 m_x - (\Gamma + P_+ + P_-) m_z + (P_+ - P_-). \quad (3.4c)$$

From Eq. (3.4b) we see that m_y decays sooner or later, so hereafter we concern ourselves only with Eqs. (3.4a) and (3.4c).

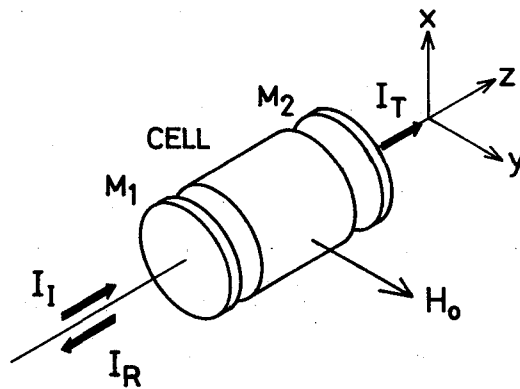


Fig. 3.1 Fabry-Perot cavity with a nonlinear medium cell. Static magnetic field H_0 is applied along the y axis.

The susceptibilities of the medium for σ_+ and σ_- light are determined by the magnetization component along their propagation direction, namely, m_z (Dehmelt, 1957; Happer, 1972). We assume that m_z varies slowly with respect to the cavity damping time $L/(cT)$, where L is the length of the cavity and T is the transmissivity of the mirrors. We can also adopt the quasi-static susceptibility approximation (Happer, 1972). The absorption coefficients α_{\pm} and the wavenumbers k_{\pm} are

$$\alpha_{\pm}(m_z) = \alpha_0(1 \mp m_z), \quad (3.5a)$$

$$k_{\pm}(m_z) = k_0 + \kappa(1 \mp m_z), \quad (3.5b)$$

where α_0 and $k_0 + \kappa$ is the absorption coefficient and the wave number for the unpolarized medium. To simplify the situation we neglect the absorption effect by taking relatively large detuning $|\Delta|$.

Thus the transmission characteristics of the Fabry-Perot cavity is given by the equation

$$I_{T\pm} = T^2 I_{I\pm} [1 + R^2 - 2R \cos 2k_{\pm}(m_z)L]^{-1}, \quad (3.6)$$

where $I_{I\pm}$ and $I_{T\pm}$ are the incident and transmitted light intensities respectively and $R = 1 - T$ is the reflectivity of the mirrors. we also assumed that m_z has no z dependence due to the standing-wave structure of the pumping field, because the atoms move many wavelengths during the pumping time P_{\pm} and the decay time Γ^{-1} . The effective pumping light intensity in the cavity is represented as a sum of the forward and backward wave intensities (Appendix A):

$$I_{\pm} = I_{T\pm}(1 + R)/T. \quad (3.7)$$

By using Eqs. (3.2), (3.6), and (3.7), the pumping rates in Eqs. (3.4) are represented as follows:

$$P_{\pm} = T[1 + R^2 - 2R \cos 2k_{\pm}(m_z)L]^{-1} Q_{\pm}, \quad (3.8)$$

where $Q_{\pm} = (1/2)\alpha(1+R)I_{I\pm}$ are quantities which relate to the incident light intensities. Substituting Eq. (3.8) into Eqs. (3.4a) and (3.4c), we obtain two-dimensional nonlinear differential equations

which describe the motion of the Bloch vector $\vec{m} = (m_z, m_x)$ in the cavity.

Let us consider, at first, the case where no external magnetic field is applied, namely, the case of $Q_0 = 0$. We rewrite Eq. (3.3c) with $Q_0 = 0$ as

$$\frac{dm_z}{dt} = f_\mu(m_z), \quad (3.9)$$

where μ represents parameters such as Γ and Q_\perp as a whole. The equilibrium points are found by solving the equation $f_\mu(m_z) = 0$, which is equivalent to Eq. (2.9), although the latter is for the field variables and the former is for the atomic variable. We also find equivalence of $f_\mu(m_z)$ to $\partial V/\partial x$ in Chapter 2, where $V(x)$ is a system potential introduced in context of the catastrophe theory. The stability of a equilibrium point is determined by the first derivative of f_μ with respect to m_z at the point. If $df_\mu/dm_z > 0$, the equilibrium point is unstable and if $df_\mu/dm_z < 0$, then stable. Figure 3.2 shows some example of $f_\mu(m_z)$ in the case of linearly polarized incident light. We choose the parameters μ so as to give single-stable, tristable, and bistable cases. We also show, in Fig. 3.3, the motion of the Bloch vector on the (m_z, m_x) plane for the bistable case. There the equilibrium point $\vec{m} = 0$ is unstable and the atomic spins orient parallel or antiparallel to the z axis spontaneously. It is quite natural to expect that if $Q_0 \neq 0$, the spontaneous magnetization continues to precess about the static magnetic field without decaying to $\vec{m} = 0$.

3.3 Self-Sustained Spin Precession

To see the effect qualitatively we introduce following

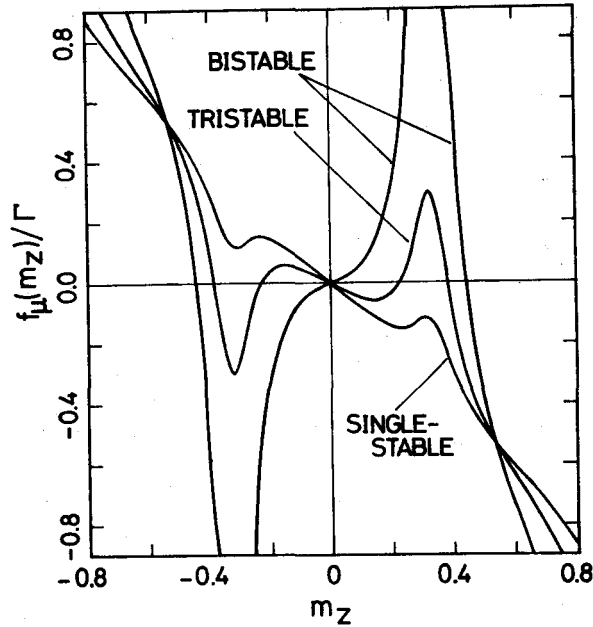


Fig. 3.2 Plot of the function $f_{\mu}(m_z)$ for single-stable, tristable, and bistable cases. Parameters are $R = 0.7$; $2k_0L = -\pi + 2M\pi$ (M : integer); $2\kappa L = 1.5\pi$; and $Q_+ = Q_- = 0.1\Gamma$ (single stable), $Q_+ = Q_- = 0.3\Gamma$ (tristable), $Q_+ = Q_- = 1.0\Gamma$ (bistable). The equilibrium points satisfying $f_{\mu}(m_z) = 0$ are stable (unstable) when $df_{\mu}/dm_z < 0$ (> 0). In the bistable case, for example, the point $m_z = 0$ is unstable and $m_z = \pm 0.44$ are stable.

equations:

$$\frac{dm_x}{dt} = -Q_0 m_z - \xi m_x, \quad (3.10a)$$

$$\frac{dm_z}{dt} = Q_0 m_x - \eta m_z (m_z^2 - m_s^2), \quad (3.10b)$$

where ξ and η are positive constants. The first terms of the right-hand side represent the precession about the y axis and the second terms simulate the motion of \vec{m} governed by Eqs. (3.4a) and (3.4c) in the absence of the magnetic field. Namely, in the case of $Q_0 = 0$, Eqs. (3.10) have two stable equilibrium points $(\pm m_s, 0)$ and an unstable equilibrium point $(0, 0)$ and give qualitatively the

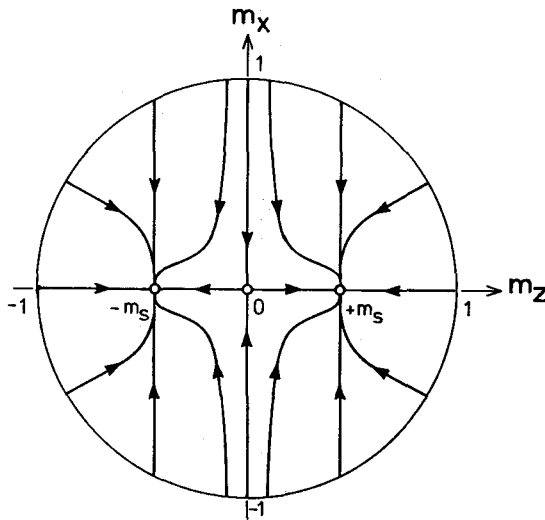


Fig. 3.3 Some trajectories of \vec{m} on the (m_z, m_x) plane for the bistable case. The stable equilibrium point $\vec{m} = (m_s, 0)$ corresponds to the σ_+ state and $\vec{m} = (-m_s, 0)$ corresponds to the σ_- state.

same flow as shown in Fig. 3.3. Equations (3.10) are quite similar to van der Pol's equations which describes the operation of electron-tube oscillators. The difference is the presence of the term ξm_x in Eq. (3.10a) but it can easily be eliminated by a variable transformation. By choosing suitable parameters, Eqs. (3.10) give a stable limit cycle on the (m_z, m_x) plane. To confirm the oscillation we solved Eqs. (3.4a) and (3.4c) numerically. Figure 3.4 gives an example of the trajectories, which starts from a point close to the origin, spirals out, and approaches to a limit cycle asymptotically. Two bends on the limit cycle are vestiges of the attractors which are located at the points $(\pm m_s, 0)$ when no magnetic field is applied. The velocity of the moving point becomes slower in the neighborhood of the bends, and therefore the period of rotation is longer than the Larmor period $T_0 = 2\pi/\Omega_0$. With an increase of Ω_0 , the period approaches to the Larmor period

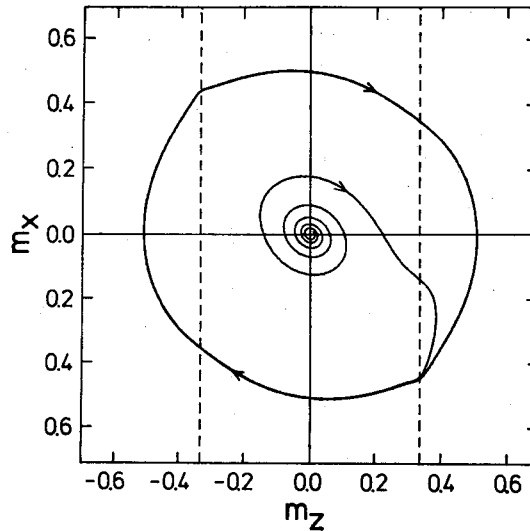


Fig. 3.4 Self-sustained precession of Bloch vector \vec{m} . Parameters are $R = 0.7$, $Q_0 = 50\Gamma$, $2k_0L = -\pi + 2M\pi$, $2\kappa L = 1.5\pi$, and $Q_+ = Q_- = 10\Gamma$.

and the limit cycle becomes rounder. There is a critical value of Q_0 below which the trajectories trapped to either of the attractors (for the parameters used in Fig. 3.4, the critical value is about 40Γ). We note that the limit cycle lies in the real space, whereas in cases of other self-pulsing phenomena, it lies in a mathematically constructed space, namely, in a phase space.

We also calculated temporal behaviors of P_{\pm} which are proportional to the intensities of the σ_+ and σ_- components of the transmitted light respectively (Fig. 3.5). The oscillation in P_{\pm} are built up according to the growth of the trajectory in Fig. 3.4. In the steady state alternative pulsation in P_{\pm} are observed. In the half cycle of $m_z > 0$ (< 0), P_+ (P_-) is enhanced and $|m_z|$ is elongated through optical pumping. Thus the length of the Bloch vector \vec{m} is maintained against the thermal relaxations.

The two peaks in each pulse, one of which is sharp and the other broad, are explained as follows. For example, P_+ which is a

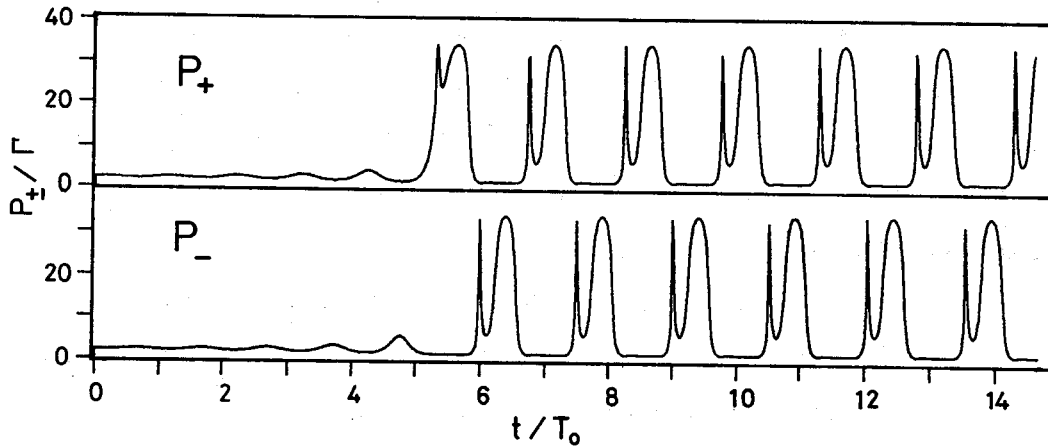


Fig. 3.5 Self-pulsing in σ_+ and σ_- components of the transmitted light. Corresponding trajectory of \vec{m} is shown in Fig. 3.4.

function of m_z takes the maximum value on the dotted line in the half plane $m_z > 0$ of Fig. 3.4. The trajectory crosses the line twice in a cycle, first rapidly in the upper half-plane and secondly slowly in the lower half-plane.

3.4 Experimental Evidence

Here we propose an actual system which exhibits the phenomenon described above. The system is essentially the same as that shown in Chapter 1, where sodium vapor was used as a nonlinear medium. The D_1 line (589.6 nm) is homogeneously broadened by filling a relatively high-pressure buffer gas (e.g. $\nu_{ab} \sim 2$ GHz for 200 torr of helium), and the Doppler broadening can be neglected. The buffer gas also serves to prevent the hyperfine pumping in the ground state $3^2S_{1/2}$. Thus the behavior of the atom can be described substantially by the model depicted in Fig. 3.1. Taking

$|\Delta l| \sim 30\gamma_{ab}$, vapor density $N \sim 3 \times 10^{12} \text{ cm}^{-3}$, and $L \sim 10 \text{ cm}$, we obtain the maximum phase shift $2\kappa L \sim 5$. The spin relaxation rate Γ is estimated to be $\sim 10^3 \text{ s}^{-1}$, and therefore the oscillation will be observed for the Larmor frequency $\Omega_0 > 40\Gamma \sim 4 \times 10^4 \text{ s}^{-1}$, which corresponds to $H_0 \gtrsim 10 \text{ mG}$. The required power density of a CW dye laser is of the order of 10 mW/mm^2 .

According to the proposal described above, Mitschke et al. (1983) performed the experiment successfully. They used a heated stainless-steel cell containing sodium atoms ($N \sim 10^{13} \text{ cm}^{-3}$) in an argon atmosphere ($\sim 150 \text{ Torr}$); the length of the heated zone is about 20 mm. The cell was placed in the center of a piezoelectrically controlled near confocal Fabry-Perot cavity (finesse = 17). The light source was a dye laser which was tuned by 10-20 GHz on either side of the Na-D₁ line. The light with a power of 5-50 mW could be switched on to observe transient phenomena. The transverse magnetic field H_0 was applied by Helmholtz coils. The right- and left-circular components were measured by a pair of photodiodes separately. Measurements were performed in either region $H_0 < H_{cr}$ or $H_0 > H_{cr}$. The critical magnetic field H_{cr} , above which oscillation took place, was in the range 0.3 to 1.5 Gauss.

(1) $H_0 < H_{cr}$: When the input intensity was switched from zero to $I > I_{cr}$ ($\sim 10 \text{ mW}$), the system stayed in the linear state for a time τ_D ($\sim 35 \text{ us}$). For $t = \tau_D$ the sudden transition to the σ_+ or the σ_- state took place. The delay was explained as a result of a critical slowing down (Haken, 1983).

(2) $H_0 > H_{cr}$: When H_0 was increased above a critical value H_{cr} with other parameters fixed, then a build-up of switching between the σ_+ and σ_- states was seen. The pulse train in the σ_+ output

and σ_- output were complementary as in Fig. 3.5. They could easily observe the pulse train for minutes. Repetition rate could be varied between 200 kHz and 13 MHz. They showed that when the laser intensity was changed with other parameters kept fixed, there was a range where self-pulsing was observed, which is consistent with a theoretical result.

They also observed the pulse-shape precisely and found two maxima exist in each pulse as in Fig. 3.5. They proposed to apply the apparatus as a current-controlled oscillator, and demonstrated the experiment of "optical FM signal transmission."

3.5 Conclusions and Discussion

We have predicted that the optical tristable system in Chapter 2 exhibits self-pulsing induced and controlled by a static magnetic field. The self-sustained spin precession is responsible for the phenomenon and can be described by a modified Bloch equation which includes a nonlinearity. The conventional linear Bloch equation having oscillating-magnetic-field terms has been widely used to describe various kinds of resonance phenomena. It is also used as an analog model for an optical transition in two-level atoms. Therefore it is an interesting problem to investigate resonance phenomena in our nonlinear Bloch equation by including oscillating-magnetic-field terms.

Another extension of our equation is possible. We have assumed that the field variables adiabatically follow the atomic variables. When the oscillating frequency is comparable to the cavity response cT/L (~ 100 MHz), the assumption is incorrect and a modification is needed. The interplay between the dynamics for the

field and that for the medium may cause new phenomena.

The first part of the paper is devoted to a discussion of the general principles of the theory of the interaction of a field with a medium. It is shown that the interaction of a field with a medium can be described by a set of equations which are similar to the equations of electrodynamics in a medium. The second part of the paper is devoted to a discussion of the interaction of a field with a medium in the case of a uniform field. It is shown that the interaction of a field with a medium in the case of a uniform field can be described by a set of equations which are similar to the equations of electrodynamics in a medium.

The third part of the paper is devoted to a discussion of the interaction of a field with a medium in the case of a non-uniform field. It is shown that the interaction of a field with a medium in the case of a non-uniform field can be described by a set of equations which are similar to the equations of electrodynamics in a medium. The fourth part of the paper is devoted to a discussion of the interaction of a field with a medium in the case of a field with a time-varying field. It is shown that the interaction of a field with a medium in the case of a field with a time-varying field can be described by a set of equations which are similar to the equations of electrodynamics in a medium.

REFERENCES

- 1. A. Poincaré, *Ann. Chem. Phys.*, **37**, 375 (1905).
- 2. H. Lorentz, *Arch. Neerl.*, **2**, 49 (1892).
- 3. H. Lorentz, *Arch. Neerl.*, **2**, 175 (1892).
- 4. H. Lorentz, *Arch. Neerl.*, **2**, 363 (1892).
- 5. H. Lorentz, *Arch. Neerl.*, **2**, 508 (1892).
- 6. H. Lorentz, *Arch. Neerl.*, **2**, 645 (1892).
- 7. H. Lorentz, *Arch. Neerl.*, **2**, 782 (1892).
- 8. H. Lorentz, *Arch. Neerl.*, **2**, 919 (1892).
- 9. H. Lorentz, *Arch. Neerl.*, **2**, 1056 (1892).
- 10. H. Lorentz, *Arch. Neerl.*, **2**, 1193 (1892).
- 11. H. Lorentz, *Arch. Neerl.*, **2**, 1330 (1892).
- 12. H. Lorentz, *Arch. Neerl.*, **2**, 1467 (1892).
- 13. H. Lorentz, *Arch. Neerl.*, **2**, 1604 (1892).
- 14. H. Lorentz, *Arch. Neerl.*, **2**, 1741 (1892).
- 15. H. Lorentz, *Arch. Neerl.*, **2**, 1878 (1892).
- 16. H. Lorentz, *Arch. Neerl.*, **2**, 2015 (1892).
- 17. H. Lorentz, *Arch. Neerl.*, **2**, 2152 (1892).
- 18. H. Lorentz, *Arch. Neerl.*, **2**, 2289 (1892).
- 19. H. Lorentz, *Arch. Neerl.*, **2**, 2426 (1892).
- 20. H. Lorentz, *Arch. Neerl.*, **2**, 2563 (1892).
- 21. H. Lorentz, *Arch. Neerl.*, **2**, 2700 (1892).
- 22. H. Lorentz, *Arch. Neerl.*, **2**, 2837 (1892).
- 23. H. Lorentz, *Arch. Neerl.*, **2**, 2974 (1892).
- 24. H. Lorentz, *Arch. Neerl.*, **2**, 3111 (1892).
- 25. H. Lorentz, *Arch. Neerl.*, **2**, 3248 (1892).
- 26. H. Lorentz, *Arch. Neerl.*, **2**, 3385 (1892).
- 27. H. Lorentz, *Arch. Neerl.*, **2**, 3522 (1892).
- 28. H. Lorentz, *Arch. Neerl.*, **2**, 3659 (1892).
- 29. H. Lorentz, *Arch. Neerl.*, **2**, 3796 (1892).
- 30. H. Lorentz, *Arch. Neerl.*, **2**, 3933 (1892).
- 31. H. Lorentz, *Arch. Neerl.*, **2**, 4070 (1892).
- 32. H. Lorentz, *Arch. Neerl.*, **2**, 4207 (1892).
- 33. H. Lorentz, *Arch. Neerl.*, **2**, 4344 (1892).
- 34. H. Lorentz, *Arch. Neerl.*, **2**, 4481 (1892).
- 35. H. Lorentz, *Arch. Neerl.*, **2**, 4618 (1892).
- 36. H. Lorentz, *Arch. Neerl.*, **2**, 4755 (1892).
- 37. H. Lorentz, *Arch. Neerl.*, **2**, 4892 (1892).
- 38. H. Lorentz, *Arch. Neerl.*, **2**, 5029 (1892).
- 39. H. Lorentz, *Arch. Neerl.*, **2**, 5166 (1892).
- 40. H. Lorentz, *Arch. Neerl.*, **2**, 5303 (1892).
- 41. H. Lorentz, *Arch. Neerl.*, **2**, 5440 (1892).
- 42. H. Lorentz, *Arch. Neerl.*, **2**, 5577 (1892).
- 43. H. Lorentz, *Arch. Neerl.*, **2**, 5714 (1892).
- 44. H. Lorentz, *Arch. Neerl.*, **2**, 5851 (1892).
- 45. H. Lorentz, *Arch. Neerl.*, **2**, 5988 (1892).
- 46. H. Lorentz, *Arch. Neerl.*, **2**, 6125 (1892).
- 47. H. Lorentz, *Arch. Neerl.*, **2**, 6262 (1892).
- 48. H. Lorentz, *Arch. Neerl.*, **2**, 6399 (1892).
- 49. H. Lorentz, *Arch. Neerl.*, **2**, 6536 (1892).
- 50. H. Lorentz, *Arch. Neerl.*, **2**, 6673 (1892).
- 51. H. Lorentz, *Arch. Neerl.*, **2**, 6810 (1892).
- 52. H. Lorentz, *Arch. Neerl.*, **2**, 6947 (1892).
- 53. H. Lorentz, *Arch. Neerl.*, **2**, 7084 (1892).
- 54. H. Lorentz, *Arch. Neerl.*, **2**, 7221 (1892).
- 55. H. Lorentz, *Arch. Neerl.*, **2**, 7358 (1892).
- 56. H. Lorentz, *Arch. Neerl.*, **2**, 7495 (1892).
- 57. H. Lorentz, *Arch. Neerl.*, **2**, 7632 (1892).
- 58. H. Lorentz, *Arch. Neerl.*, **2**, 7769 (1892).
- 59. H. Lorentz, *Arch. Neerl.*, **2**, 7906 (1892).
- 60. H. Lorentz, *Arch. Neerl.*, **2**, 8043 (1892).
- 61. H. Lorentz, *Arch. Neerl.*, **2**, 8180 (1892).
- 62. H. Lorentz, *Arch. Neerl.*, **2**, 8317 (1892).
- 63. H. Lorentz, *Arch. Neerl.*, **2**, 8454 (1892).
- 64. H. Lorentz, *Arch. Neerl.*, **2**, 8591 (1892).
- 65. H. Lorentz, *Arch. Neerl.*, **2**, 8728 (1892).
- 66. H. Lorentz, *Arch. Neerl.*, **2**, 8865 (1892).
- 67. H. Lorentz, *Arch. Neerl.*, **2**, 9002 (1892).
- 68. H. Lorentz, *Arch. Neerl.*, **2**, 9139 (1892).
- 69. H. Lorentz, *Arch. Neerl.*, **2**, 9276 (1892).
- 70. H. Lorentz, *Arch. Neerl.*, **2**, 9413 (1892).
- 71. H. Lorentz, *Arch. Neerl.*, **2**, 9550 (1892).
- 72. H. Lorentz, *Arch. Neerl.*, **2**, 9687 (1892).
- 73. H. Lorentz, *Arch. Neerl.*, **2**, 9824 (1892).
- 74. H. Lorentz, *Arch. Neerl.*, **2**, 9961 (1892).
- 75. H. Lorentz, *Arch. Neerl.*, **2**, 10098 (1892).
- 76. H. Lorentz, *Arch. Neerl.*, **2**, 10235 (1892).
- 77. H. Lorentz, *Arch. Neerl.*, **2**, 10372 (1892).
- 78. H. Lorentz, *Arch. Neerl.*, **2**, 10509 (1892).
- 79. H. Lorentz, *Arch. Neerl.*, **2**, 10646 (1892).
- 80. H. Lorentz, *Arch. Neerl.*, **2**, 10783 (1892).
- 81. H. Lorentz, *Arch. Neerl.*, **2**, 10920 (1892).
- 82. H. Lorentz, *Arch. Neerl.*, **2**, 11057 (1892).
- 83. H. Lorentz, *Arch. Neerl.*, **2**, 11194 (1892).
- 84. H. Lorentz, *Arch. Neerl.*, **2**, 11331 (1892).
- 85. H. Lorentz, *Arch. Neerl.*, **2**, 11468 (1892).
- 86. H. Lorentz, *Arch. Neerl.*, **2**, 11605 (1892).
- 87. H. Lorentz, *Arch. Neerl.*, **2**, 11742 (1892).
- 88. H. Lorentz, *Arch. Neerl.*, **2**, 11879 (1892).
- 89. H. Lorentz, *Arch. Neerl.*, **2**, 12016 (1892).
- 90. H. Lorentz, *Arch. Neerl.*, **2**, 12153 (1892).
- 91. H. Lorentz, *Arch. Neerl.*, **2**, 12290 (1892).
- 92. H. Lorentz, *Arch. Neerl.*, **2**, 12427 (1892).
- 93. H. Lorentz, *Arch. Neerl.*, **2**, 12564 (1892).
- 94. H. Lorentz, *Arch. Neerl.*, **2**, 12701 (1892).
- 95. H. Lorentz, *Arch. Neerl.*, **2**, 12838 (1892).
- 96. H. Lorentz, *Arch. Neerl.*, **2**, 12975 (1892).
- 97. H. Lorentz, *Arch. Neerl.*, **2**, 13112 (1892).
- 98. H. Lorentz, *Arch. Neerl.*, **2**, 13249 (1892).
- 99. H. Lorentz, *Arch. Neerl.*, **2**, 13386 (1892).
- 100. H. Lorentz, *Arch. Neerl.*, **2**, 13523 (1892).

CHAPTER 4

OPTICALLY BISTABLE SYSTEM WITHOUT A CAVITY

4.1 Introduction

The optical bistability exhibited in all of the systems studied so far can be characterized by the presence of hysteresis, which appears in intensity changes of the output light (transmitted or reflected light) as the incident light intensity is varied. The optical bistability that we propose and study in this chapter is largely different from ordinary bistability. The most striking difference is that this optical bistability has no hysteresis but has symmetry breaking (or a pitchfork bifurcation), for the variation of intensity of the linearly polarized incident light. The optical system has a positive feedback loop for the intensity difference of circularly polarized components of light, not for the light intensity itself as in the ordinary optical bistable systems. When the incident light intensity exceeds a critical value and the differential gain overcomes the loss in the loop, the stable state bifurcates into two symmetrically lying branches called σ_+ and σ_- states. In the σ_+ (σ_-) state the polarization of the light in the cell is almost right (left) circular. At the critical point the system gets into either of these states with equal probability, where no jump in the output occurs. So the bifurcation can be viewed as a second-order phase transition. The jump between two stable branches, which can be observed in ordinary optical bistability, does not occur in the present system, when its input intensity is varied. In the case of optical tristability

(Chapter 2), the symmetry breaking occurs simultaneously with a jump in a doubled hysteresis cycle, and can be viewed as a first-order phase transition. Another interesting feature of this system is that when the polarization plane of the incident light is rotated continuously, a sudden jump from one state to the other occurs. A hysteresis loop appears when we swing the polarization plane.

The optical system to be studied theoretically and experimentally in this chapter is very simple, which has no optical cavity. So careful adjustments of laser frequency to the cavity fringe are not needed. Use of multimode laser is also allowed. It consists of a cell containing atoms with spin in the ground state, which is used as a nonlinear dispersive medium, a $\lambda/8$ plate which converts an polarization state, and a mirror to feedback the transmitted light to the cell. The incident light is near-resonant to the atomic absorption line and linearly polarized. Competitive optical pumping by σ_{\pm} components is caused by the optical feedback through the phenomenon called optically rotatory power (Gozzini, 1962), or (optically induced) Faraday rotation. Two stable states of this system can be characterized by the polarization of output light or the direction of spin polarization of atoms. In Sec. 4.2 we describe about the setup of the optical system, and study its stable states using a simplified atomic model. The present optical bistability is discussed from the point of view of catastrophe theory (Thom, 1975; Zeeman 1977), and we show that it can be explained in context with the cusp catastrophe, similarly to the ordinary bistability with hysteresis (Agrawal and Carmichael, 1979). In Sec. 4.3, we study theoretically on the phenomenon of self-sustained spin precession occurring in this

system when a static magnetic field is applied perpendicularly to the light beam. This results in the modulation of polarization of the output light at about the Larmor frequency. This phenomenon is similar to that in an optically tristable system, which has been theoretically studied in Chapter 3 and recently observed by Mitschke et al. (1983). In Sec. 4.4, we study experimentally about the new type of optical bistability, using sodium vapor and a laser beam tuned at the D_1 line, and we show an evidence of symmetry breaking and pitchfork bifurcation.

4.2 Optical System and Stable States

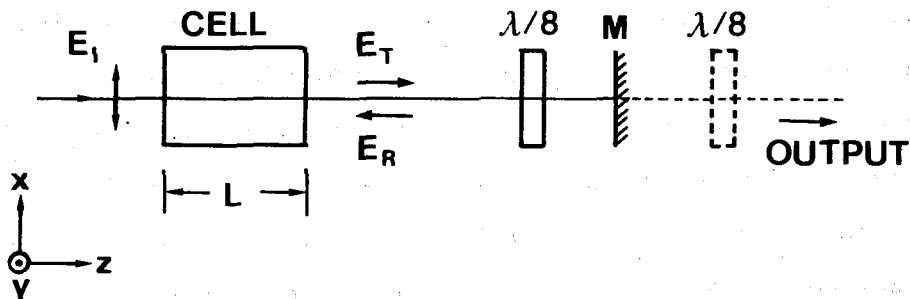


Fig. 4.1 Optical system exhibiting bistability with symmetry breaking, together with the definition of coordinates. The $\lambda/8$ plate shown by dashed lines is used to monitor the field E_T or E_R .

The optical system consists of a cell containing atoms with Zeeman sublevels in the ground state, such as alkali-metal atoms, a $\lambda/8$ plate, and a mirror, as shown in Fig. 4.1. Incident light is linearly polarized and its frequency is near-resonant to the atomic absorption line, i.e. it is in a region of anomalous dispersion. After transmitted through the cell, the light is passed through a

$\lambda/8$ and then reflected back to the cell by a mirror. Since the light beam passes twice the $\lambda/8$ plate, it plays a role of a $\lambda/4$ plate for a single path. So, unless the optical axis of the $\lambda/8$ plate is oriented to the direction parallel or perpendicular to the polarization of the incident light, the backward light is elliptically polarized in general, i.e. the intensities of σ_{\pm} circularly polarized components become different. Because of this intensity difference, the atoms in the cell are optically pumped and atomic spins are oriented parallel or antiparallel to the beam axis. When the spin-polarization is produced in this way, the incident light is subjected to the rotation of polarization because of the difference of refractive indices for the σ_{\pm} components. If the optical axis of the $\lambda/8$ plate is adequately oriented, the rotation of polarization for the incident light beam can increase the intensity difference of circularly polarized components in the backward light. As shown in Fig. 4.1, we take the x and z axes to the directions of polarization and propagation of the incident light, respectively. Let us write θ as the rotation angle of polarization and θ_0 as the angle between the x axis and the direction of optical axis of the $\lambda/8$ plate, which we shall call "offset angle."

A small amount of the light passed through the mirror is applied to another $\lambda/8$ plate shown by dashed lines in Fig. 4.1, which is used to monitor the changes of polarization and intensities of the forward and backward light beams. When the optical axes of two $\lambda/8$ plates are oriented perpendicularly to each other, the phase-retardation is cancelled out, so that the polarization of the output light becomes the same as that of the forward light beam transmitted through the cell. On the other

hand, when they are oriented parallel, the polarization of the output light becomes the same as that of the backward light fed back to the cell).

The atomic system we utilize is essentially the same that was used in Chapters 2 and 3. So we begin with the Bloch equation:

$$\frac{dm_x}{dt} = -Q_0 m_z - (\Gamma + I_+ + I_-) m_x, \quad (4.1a)$$

$$\frac{dm_y}{dt} = -(\Gamma + I_+ + I_-) m_y, \quad (4.1b)$$

$$\frac{dm_z}{dt} = Q_0 m_x - (\Gamma + I_+ + I_-) m_z + (I_+ - I_-), \quad (4.1c)$$

where $\vec{m} = {}^t(m_x, m_y, m_z)$ is the normalized spin polarization in the ground state, Γ is the spin relaxation rate, and I_{\pm} are the σ_{\pm} light intensities which are normalized so as to give the pumping rate. The optical axis is taken along the z axis. The Larmor frequency Q_0 is given by the relation:

$$Q_0 = \gamma H_0, \quad (4.2)$$

where γ and H_0 is the gyromagnetic ratio and the strength of the magnetic field applied along the y axis. The absorption coefficients α_{\pm} and the wavenumbers k_{\pm} for σ_{\pm} light propagating in this medium are given as

$$\alpha_{\pm}(m_z) = \alpha(1 \mp m_z), \quad (4.3a)$$

$$k_{\pm}(m_z) = k_0 + \kappa(1 \mp m_z), \quad (4.3b)$$

where α and κ are the absorption coefficient and the incremental wavenumber for the unpolarized ($m_z = 0$) medium, respectively, and

k_0 is the wavenumber in a vacuum. As in Chapters 2 and 3, we neglect the absorption effect by taking the laser frequency on a far wing of the absorption line. When linearly polarized light is propagated through the polarized ($m_z \neq 0$) medium with a length L , the polarization plane is rotated by an angle θ (Faraday rotation). Hereafter we represent a state of light polarization in the following form:

$$\vec{E} = E_x \hat{x} + E_y \hat{y} = E_+ \hat{e}_+ + E_- \hat{e}_-, \quad (4.4)$$

where $\hat{e}_\pm = (\hat{x} \mp i\hat{y})/\sqrt{2}$. The linear components E_x , E_y and the circular components E_+ , E_- are related by the following relation:

$$\begin{bmatrix} E_x \\ E_y \end{bmatrix} = \frac{1}{\sqrt{2}} \begin{bmatrix} 1 & 1 \\ -i & i \end{bmatrix} \begin{bmatrix} E_+ \\ E_- \end{bmatrix} = D \begin{bmatrix} E_+ \\ E_- \end{bmatrix}, \quad (4.5)$$

Now for the linearly polarized incident light

$$\vec{E}_I = E_0 \hat{x}, \quad (4.6)$$

the transmitted light \vec{E}_T is represented as

$$\begin{aligned} \begin{bmatrix} E_{Tx} \\ E_{Ty} \end{bmatrix} &= D \begin{bmatrix} e^{-ik_+L} & \\ & e^{-ik_-L} \end{bmatrix} D^{-1} \begin{bmatrix} E_0 \\ 0 \end{bmatrix} \\ &= E_0 \begin{bmatrix} \cos\theta \\ \sin\theta \end{bmatrix}, \end{aligned} \quad (4.7)$$

where $\theta = (k_- - k_+)L/2$. We have neglected a common phase factor. The Faraday rotation angle θ is represented in term of m_z as

$$\theta = \kappa m_z L. \quad (4.8)$$

The fast axis of the $\lambda/8$ plate and the x axis form a offset

angle θ_0 . We set an x' axis along the fast axis and a y' axis along the slow axis. In this frame of reference \vec{E}_T is represented as

$$\begin{aligned} \begin{bmatrix} E_{Tx'} \\ E_{Ty'} \end{bmatrix} &= U(-\theta_0) \begin{bmatrix} E_{Tx} \\ E_{Ty} \end{bmatrix} \\ &= E_0 \begin{bmatrix} \cos\bar{\theta} \\ \sin\bar{\theta} \end{bmatrix}, \end{aligned} \quad (4.9)$$

where $\bar{\theta} = \theta + \theta_0$ and

$$U(\theta) = \begin{bmatrix} \cos\theta & -\sin\theta \\ \sin\theta & \cos\theta \end{bmatrix}. \quad (4.10)$$

The polarization state \vec{E}_R of light reflected back to the cell is

$$\begin{aligned} \begin{bmatrix} E_{Rx'} \\ E_{Ry'} \end{bmatrix} &= R \begin{bmatrix} e^{-i\pi/8} & \\ & e^{i\pi/8} \end{bmatrix}^2 \begin{bmatrix} E_{Tx'} \\ E_{Ty'} \end{bmatrix} \\ &= \frac{E_0}{\sqrt{2}} \begin{bmatrix} (1-i)\cos\bar{\theta} \\ (1+i)\sin\bar{\theta} \end{bmatrix}, \end{aligned} \quad (4.11)$$

where R is the reflectivity of the mirror and the squared matrix represents the forward and backward passes through the $\lambda/8$ plate.

The state \vec{E}_R in the circular representation is

$$\begin{aligned} \begin{bmatrix} E_{R+} \\ E_{R-} \end{bmatrix} &= D^{-1}U(\theta_0) \begin{bmatrix} E_{Rx'} \\ E_{Ry'} \end{bmatrix} \\ &= \frac{RE_0}{2} \begin{bmatrix} [\cos\bar{\theta} - \sin\bar{\theta} - i(\cos\bar{\theta} - \sin\bar{\theta})]e^{-i\theta_0} \\ [\sin\bar{\theta} + \sin\bar{\theta} - i(\cos\bar{\theta} + \sin\bar{\theta})]e^{i\theta_0} \end{bmatrix}. \end{aligned} \quad (4.12)$$

Thus we have the σ_{\pm} intensities of the feedback light as

$$I_{R\pm} = |E_{R\pm}|^2 = \frac{RI_0}{2}(1 \pm \sin 2\bar{\theta}), \quad (4.13)$$

where $I_0 = E_0^2$. The total intensities of σ_{\pm} light in the cell is

$$I_{\pm} = E_0^2/2 + I_{R\pm} = (I_0/2)[(R + 1) \pm R \sin 2\bar{\theta}]. \quad (4.14)$$

Substitution of Eq. (4.14) into Eq. (4.1) gives the system equations. In the absence of a magnetic field, it is sufficient to consider only Eq. (4.1c).

$$\frac{dm_z}{dt} = -(\Gamma + 2I_0)m_z + I_0 \sin 2(\kappa L m_z + \theta_0), \quad (4.15)$$

where we have assumed $R = 1$ for simplicity. Firstly we study on the steady state solution of this equation for the case of $\theta_0 = 0$. Apparently $m_z = 0$ is a steady state solution in any cases. The stability of this solution is determined by estimating the derivative of the right-hand side at $m_z = 0$; when it is negative (positive), the solution is stable (unstable). The stability condition is

$$-(\Gamma + 2I_0) + 2I_0\kappa L < 0. \quad (4.16)$$

Consider a case where $\kappa L \gg 1$. When $0 \leq I_0 < I_{cr} = (\Gamma/2)(\kappa L - 1)^{-1}$, the solution $m_z = 0$ is stable and when $I_0 > I_{cr}$, it is unstable. At $I_0 = I_{cr}$, a symmetry breaking bifurcation occurs. To see how the bifurcation takes place we introduce new variables:

$$X = 2\kappa L m_z \ll 1,$$

$$\alpha = I_{cr} - I_0 \ll 1.$$

Substitution of these variables into Eq. (4.15) yields

$$\begin{aligned} \frac{dX}{dt} &= -2\alpha(k_1 - 1)X - (\kappa LI_{cr}/3)X^3 + O(X^5) \\ &= -\partial V_\alpha(X)/\partial X, \end{aligned} \quad (4.17)$$

It is important to note that the coefficient of X^3 term is negative. This means a solution starting near the origin does not run away to the infinity and allows us to neglect the terms higher than X^3 . If the X^3 coefficient is positive, we must include the X^5 term as in the case of optical tristability.

It is easy to see the potential function $V_\alpha(X)$ is identical to Eq. (B.9) with $v_0 = 0$:

$$F_U(X) = X^4 + uX^2, \quad (4.18)$$

which is a normal form to represent a pitchfork bifurcation. Furthermore we can assert, from the discussion in Appendix B, that inclusion of asymmetry gives the cusp catastrophe:

$$F_{UV}(X) = X^4 + uX^2 + v. \quad (4.19)$$

In fact, if we repeat the same procedure as above for the case $\theta_0 \neq 0$, we have a Taylor expansion of Eq. (4.15):

$$\frac{dX}{dt} = a_0\theta_0 - a_1\alpha X + a_2\theta_0 X^2 - a_3 X^3, \quad (4.20)$$

where a_i ($i = 0, \dots, 3$) are positive constants. By a variable transformation $X = X' + a_2\theta_0/3$, the X^2 term can be eliminated;

$$\frac{dX'}{dt} = (a_0/a_3)\theta_0 - (a_1/a_3)\alpha X' - X'^3. \quad (4.21)$$

The correspondence to the cusp catastrophe is clear.

We performed the numerical calculations to obtain the solution

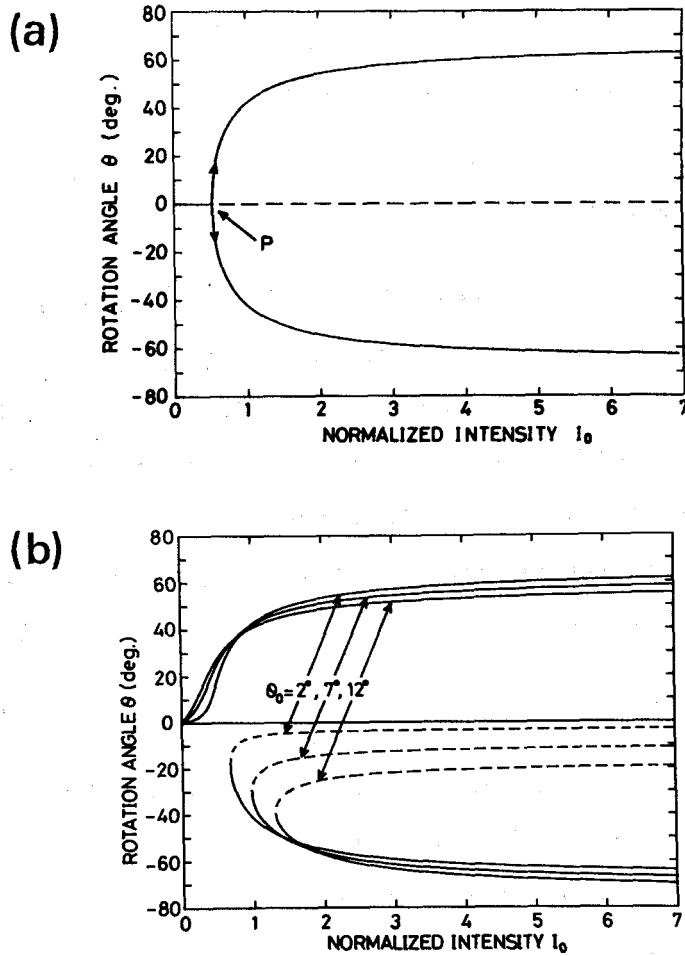


Fig. 4.2 Equilibrium rotation angle θ as a function of incident light intensity I_0 in the case that (a) $\theta_0 = 0$, and (b) $\theta_0 = 2^\circ, 7^\circ$ and 12° . In above cases kl is fixed at 3.5. Dashed lines show the unstable equilibrium values.

quantitatively. Figure 4.2(a) shows the equilibrium values of θ as a function of the incident light intensity I_0 in the case that $\theta_0 = 0$. The stable and unstable values are shown by solid and dotted lines, respectively. When I_0 is increased from zero and exceeds the critical value given by Eq. (4.16), a symmetry breaking takes place and the rotation of polarization occurs toward either of positive or negative direction with equal probability. The upper

and lower branches in Fig. 4.2(a) correspond to the atomic stable states in which spins in the ground state are oriented parallel and antiparallel to the light axis, respectively. It is important to note that a hysteresis cycle cannot be seen in the rotation angle θ as a function of I_0 .

Figure 4.2(b) shows the cases that the offset angle θ_0 is 7° , 12° and 18° . When θ_0 has non-zero value, θ changes monotonously as seen in Fig. 4.2(b), because the amplification of θ becomes asymmetry for the directions of rotation of polarization. Even in these cases, there appears another stable state when I_0 exceeds a critical value, but the system does not get into this state unless it is subjected to additional perturbation to convert the direction of spin polarization.

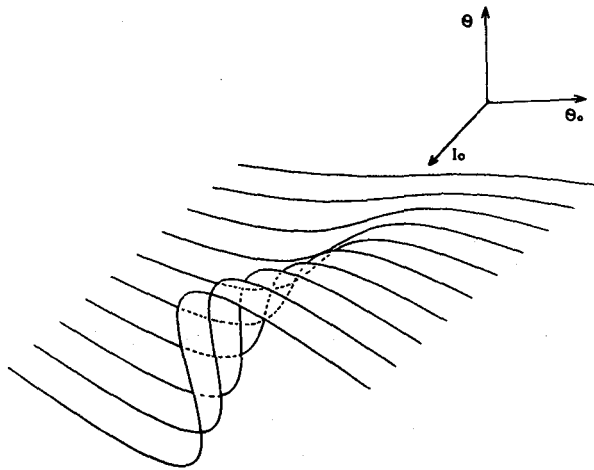


Fig. 4.3 Rotation angle θ as a function of the offset angle θ_0 . The incident light intensity I_0 is varied as a parameter.

The switching between stable states in the bistable region becomes possible when we vary θ_0 . Figure 4.3 shows the calculated rotation angle θ as a function of θ_0 , in which I_0 is

varied as a parameter. In Fig. 4.3, we see that the surface representing (θ, I_0, θ_0) has a close resemblance to the steady state surface of the cusp catastrophe (Thom, 1975; Poston and Stewart, 1978). In this way, we see that the present optical bistability belongs to the same catastrophe as the ordinary one, and different features can be explained by orthogonal cross-sections of the steady-state surface.

4.3 Self-Pulsing by Spin Precession

Let us consider the case where a static magnetic field \vec{H}_0 is applied transversely to the laser beam in Fig. 4.1. In this case, Eqs. (4.1a) and (4.1c) should be considered. It is unnecessary to consider the y component of \vec{m} because it does not couple to m_z nor m_x and decays to zero. Substitution of Eq. (4.15) into Eqs. (4.1a) and (4.1c) gives

$$\frac{dm_x}{dt} = -Q_0 m_x - (\Gamma + 2I_0) m_x, \quad (4.22)$$

$$\frac{dm_z}{dt} = Q_0 m_x - (\Gamma + 2I_0) m_z + I_0 \sin 2\kappa l m_z, \quad (4.23)$$

For simplicity, we have assumed $\theta_0 = 0$. Eliminating m_x from Eqs. (4.22) and (4.23), we obtain the equation of motion for m_z :

$$\frac{d^2 m_z}{dt^2} + f(m_z) \frac{dm_z}{dt} + g(m_z) = 0, \quad (4.24)$$

with

$$f(m_z) = 2(\Gamma + 2I_0) - 2\kappa l I_0 \cos 2\kappa l m_z,$$

$$g(m_z) = [Q_0^2 + (\Gamma + 2I_0)^2]m_z - I_0(\Gamma + 2I_0) \sin 2\kappa l m_z.$$

If we expand the trigonometric functions with respect to m_z up to second order, Eq. (4.24) is reduced to the van der Pol equation. So we can expect that \vec{m} precesses around \vec{H}_0 without any external driving forces. We can apply the theorem on the existence of a limit cycle to Eq. (4.24) (See Appendix C). Using the theorem we can assert that when

$$I_0 > \Gamma(\kappa L - 2)^{-1}, \quad (4.25a)$$

and

$$Q_0 > [(\Gamma + 2I_0)(2(\kappa L - 1)I_0 - \Gamma)]^{1/2}, \quad (4.25b)$$

at least one limit cycle exists for Eq. (4.24). We show in Fig. 4.4 the region in the (I_0, Q_0) plane where the condition are satisfied. A more precise bifurcation structure is drawn in reference to Takens' normal form of vector field (Appendix C).

Figure 4.5 shows the trajectories of \vec{m} calculated numerically by using Eqs. (4.22) and (4.23), in the cases that (a) $\kappa L = 3.5$, $I_0 = 1.0\Gamma$, $Q_0 = 20$, (b) $\kappa L = 3.5$, $I_0 = 3.0\Gamma$, $Q_0 = 45$, and (c) $\kappa L = 3.5$, $I_0 = 3.0\Gamma$ and $Q_0 = 55$. As seen in Fig. 4.5(c), the magnetization, starting from the nearly zero value, spirals out and approaches asymptotically a limit cycle. It must be noted that, when Q_0 is not zero, the growth of m_z is much faster than above case of $\theta_0 = 0$, and the limit cycle becomes asymmetry with respect to the origin $\vec{m} = (0,0)$. The frequency of the spin precession is lower than the Larmor frequency Q_0 . Figure 4.6 shows the precession frequency as a function of Q_0 , in the cases that $\theta_0 = 0$, $\kappa L = 3.5$, and $I_0 = 3.0\Gamma$, 6.0Γ and 9.0Γ . In Fig. 4.6, we see that,

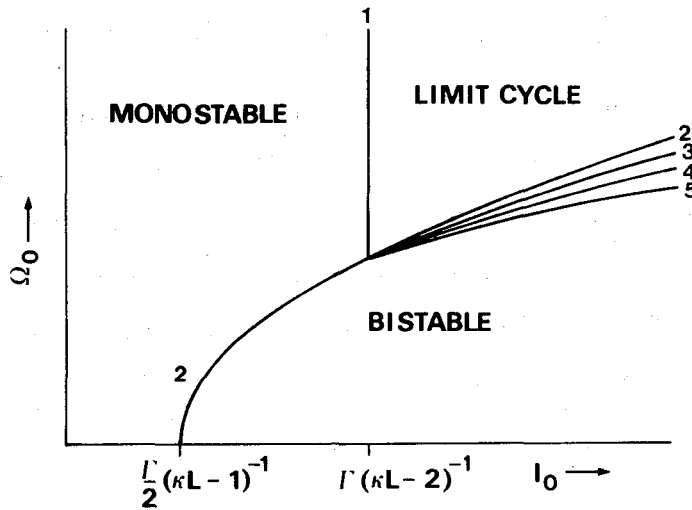


Fig. 4.4 Schematic bifurcation diagram on the (I_0, Q_0) plane. Roughly speaking, it is divided into three regions: a monostable, bistable, and limit-cycle regions. Curves 1 and 2 correspond to the conditions (4.25a) and (4.25b) for the existence of a limit cycle. On the curves 1 and 2, a Hopf bifurcation and a pitchfork bifurcation (symmetric saddle-node connection) take place, respectively. On the curve 3, there appears a Hopf bifurcation of each bistable point. On the curve 4, a saddle connection occurs and two homoclinic orbits are created. On the curve 5, a stable and unstable limit cycles appear (dynamic saddle-node connection). Above the curve 5, a stable limit cycle exists but below the curve 3, two bistable points coexist. Above the curve 3, the limit cycle is a unique attractor. The condition given by the curve 2 is a little severe.

when Q_0 is just above the critical value Q_{cr} , the precession frequency is considerably lower than the Larmor frequency Q_0 (the straight line from the origin), and it approaches asymptotically to Q_0 with the increase of the applied field intensity. The self-sustained spin precession can be observed as the modulation of the rotation angle θ for the forward light beam or as the alternative switching of σ_{\pm} components in the backward beam.

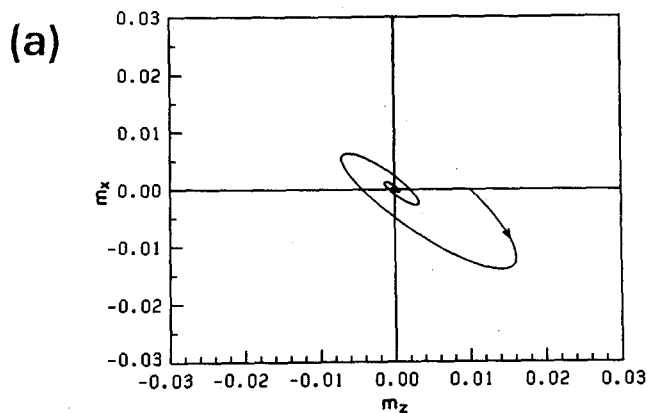
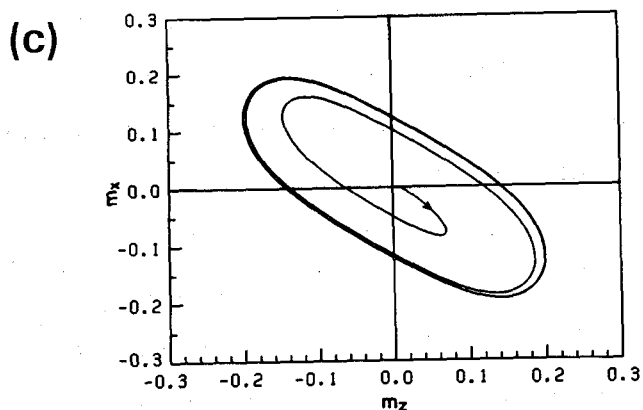
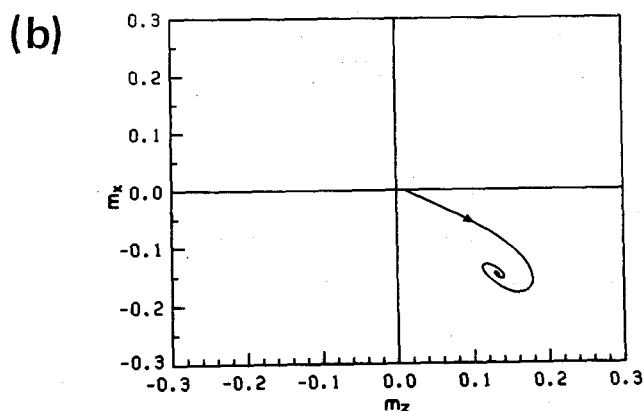


Fig. 4.5 Trajectories of normalized magnetization \vec{m} on a plane perpendicular to the static magnetic field H_0 , in the cases that (a) $I_0 = 1.0\Gamma$, $Q_0 = 20\Gamma$, (b) $I_0 = 3.0\Gamma$, $Q_0 = 45\Gamma$, and (c) $I_0 = 3.0\Gamma$, $Q_0 = 55\Gamma$. In above cases, kL is fixed at 3.5.



4.4 Experiment with Sodium Vapor

An experiment to realize the new type of optical bistability has been carried out by using the optical system schematically shown in Fig. 4.7, in which a $\lambda/4$ plate is used instead of the $\lambda/8$

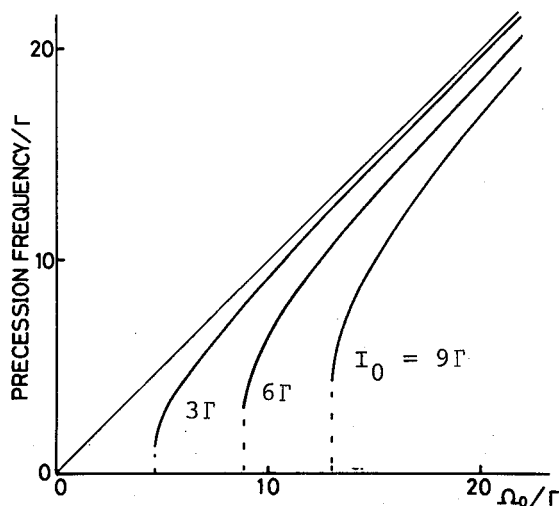


Fig. 4.6 Frequency of steady state precession of \vec{m} as a function of the strength of the applied magnetic field in terms of Ω_0 , for three values of I_0 . The straight line from the origin shows the frequency of free precession.

plate. The light from a cw dye laser, tuned on a wing of the Na- D_1 line, is applied to the sodium cell (heat-pipe oven) with 25 cm length and 3.5 cm i.d. The cell contains helium gas at about 500 torr, at which the pressure broadening of the D_1 line by the helium gas was measured to be about 8 GHz (HWHM). This value is much larger than the Doppler width (~ 1.7 GHz) and the hyperfine splitting in the ground state of sodium (1.7 GHz). So we can neglect the hyperfine optical pumping. In addition, the excited state $3^2P_{1/2}$ is completely mixed at this helium pressure, so that the three-level approximation used in Section 4.2 may be good under the present condition. After passed through the cell, the light beam is transmitted through a $\lambda/4$ plate and then fed back to the cell. The $\lambda/4$ plate for a single optical path is equivalent to the $\lambda/8$ plate in the optical system shown in Fig. 4.1. The incident

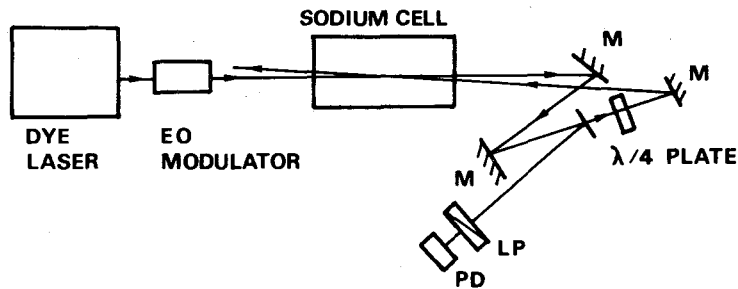


Fig. 4.7 Schematic illustration of experimental setup. Symbols have the following significance: M - mirror, LP - linear polarizer, and PD - photodetector.

light intensity I_0 is varied in the range 0-120 mW by using an electro-optic modulator. The beam diameters of the incident and backward beams were 5 mm and 8 mm, respectively, at the position of the sodium cell. A beam splitter is inserted between the cell and the $\lambda/4$ plate, and the rotation of polarization θ is measured by detecting the intensity of the light passed through a linear polarizer whose optical axis is inclined by 45 degree from the polarization axis of the incident light. Thus, the detected light intensity I_d is given by $I_0 \cos^2(\theta + \pi/4)$, when the absorption of the light can be neglected. The detuning $\Delta\omega$ of the laser frequency from the center of the D_1 line was measured by applying a part of laser output to a Na cell without a buffer gas and to a Fabry-Perot interferometer. In the present experiment, the detuning $\Delta\omega$ was kept constant at 100 GHz, and the cell temperature at 463°K, which gives the sodium density of $\sim 2.3 \times 10^{12} \text{ cm}^{-3}$.

Figure 4.8 shows the experimentally obtained change of the detected light intensity I_d as a function of the incident light intensity I_0 , which is expressed in terms of power (mW). Figure 4.8(a) shows the case that θ_0 is set at the value close to zero

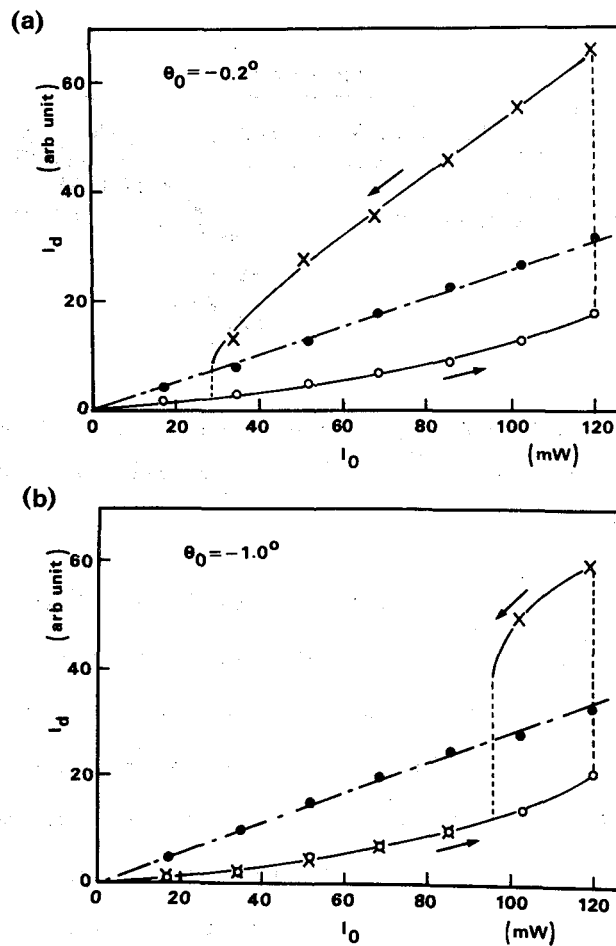


Fig. 4.8 Detected light intensity I_d , which is approximately proportional to $I_0 \cos^2(\theta + \pi/4)$, as a function of the incident light intensity I_0 for (a) $\theta_0 = -0.2^\circ$ and (b) $\theta_0 = -1^\circ$. Black circles shows the case that the backward light is blocked.

($\theta_0 = -0.2^\circ$). As I_0 is increased, I_d changes along the lower branch because the system is not exactly symmetric. At $I_0 = 120$ mW, the switching from the lower branch to the upper one was made by changing θ_0 from the original value to a relatively large positive value and then back to the original value again. After such a procedure, the system can be put on the upper branch. As I_0 is decreased in this situation, I_T changes along the upper branch

and a small jump back to the lower branch takes place at $I_0 = 26$ mW. The straight dash-dotted line from the origin shows the plots of I_d in the case that the backward beam is blocked. When θ_0 is carefully adjusted to zero, we could observe the phenomenon of symmetry breaking in I_d , i.e. the random choice of its change along the upper or lower branch in each scan of I_0 . But it was difficult to keep such a condition for a minute. Figure 4.8(b) shows the similar plots of I_d as a function of I_0 , in the case that $\theta_0 = -1^\circ$. The switching from the lower to upper branches at $I_0 = 120$ mW was made by changing θ_0 as mentioned above.

In order to verify the theoretical prediction that the present system behaves with hysteresis when θ_0 is varied, we have measured

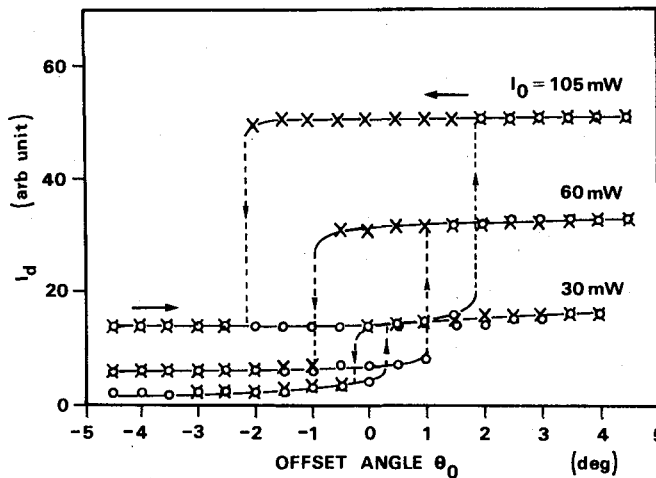


Fig. 4.9 Detected light intensity I_d as a function of the offset angle θ_0 for incident light intensities $I_0 = 30, 60$ and 105 mW.

I_d as a function of the offset angle θ_0 , keeping I_0 constant. The results are shown in Fig. 4.9, for the cases that $I_0 = 30, 60$ and 105 mW. In Fig. 4.9, we see clearly a hysteresis cycle in $I_d(\theta_0)$, whose bistable region spreads out for larger values of I_0 . The

critical value of I_0 to obtain a hysteresis cycle was about 20 mW.

4.5 Conclusions and Discussion

In this chapter we have studied on a simple optically bistable system with no optical cavity and found that the behavior of this system is largely different from ordinary optical bistability reported so far. As incident light intensity I_0 is varied, the present system behaves with pitchfork bifurcation (or symmetry-breaking), which is in contrast with the ordinary optical bistability with hysteresis. We have shown that the present optical bistability can well be explained in context with the cusp catastrophe similarly to the ordinary one, different features being attributable to the different (orthogonal) cross-sections of the steady state surface of the cusp catastrophe. In the present system, a hysteresis cycle can be obtained when one varies the offset angle θ_0 of the $\lambda/8$ plate (or the $\lambda/4$ plate in the system shown in Fig. 4.7). Namely, both of the first and second order phase transitions can be observed by varying respectively the quantities θ_0 and I_0 . In a ferromagnetic material, for example, hysteresis and pitchfork bifurcation in magnetization are observed when magnetic field intensity is varied and when the temperature is varied in the vicinity of the Curie point, respectively.

Theoretical study has been made on the behavior of the present system under a static magnetic field applied perpendicularly to the beam axis, and we have found that the magnetization produced spontaneously by symmetry breaking precesses around the field without any external periodic forces.

In the theoretical analysis presented in this chapter, we have

neglected the loss of light intensity by the absorption. Such simplification may be valid when the laser frequency is tuned on the far wing of the absorption line, as in the present experiment. When the light absorption cannot be neglected, the incident light is subjected to the circular dichroism, in addition to the rotation of polarization, which makes the polarization elliptical as it is propagated in the optically pumped medium. Numerical calculations were made in such cases, and we found that the light absorption modifies quantitatively the rotation angle θ or the magnetization m_z and critical incident light intensity I_{cr} from those presented in this chapter, but it does not cause important changes in physics involved. We found that, when the absorption loss is less than about 10 % for a single path, i.e. the circular dichroism is not important and the effect of light absorption can be well described by a homogeneous loss introduced in the feedback loop.

We have carried out the experiments using sodium vapor, and we have been able to obtain the evidence that the system shown in Fig. 4.7 behaves with symmetry breaking, or pitchfork bifurcation, when the offset angle θ_0 is zero. Furthermore, a hysteresis cycle has been observed when θ_0 is varied, as predicted by the theory. Experiments using the simpler system shown in Fig. 4.1 are now under way in our laboratory, and preliminary results show that the behavior is quite similar to that reported in this paper.

It must be pointed out that the present optical bistability has some similarities to the optical tristability, the behavior of which was theoretically studied in Chapter 2 and recently observed by Cecchi et al. (1982) and Mitschke et al. (1983) in the experiments using sodium vapor. Similarly to the present case, the optically tristable system has a positive feedback loop for the

intensity differences of two circularly polarized components of light and it exhibits symmetry breaking and self-pulsing in a static magnetic field. In the case of optical tristability and also in the case of ordinary bistability, the optical feedback is achieved by using a Fabry-Perot cavity and differential gain is obtained by using the slope of the resonance of cavity. Three stable states observed at the same incident light intensity can be described in terms of atomic spin states: spin oriented parallel, antiparallel to the beam axis, and at random. The random spin state is unstable in the bistable region of the present case, as seen in Fig. 4.2(a). The important thing to note is that the symmetry breaking takes place simultaneously with a jump in a doubled hysteresis cycle in the optical tristability, and such features can be explained in context with the butterfly catastrophe.

The requirement for the laser spectrum to obtain the present optical bistability is not so severe. We have to avoid the strong absorption at the central region of the resonance line, but it is enough to tune the laser frequency roughly in a relatively wide range on the far wing. In the case of optical tristability, the laser frequency must be tuned both on wings of atomic absorption line and to a foot of a sharp resonance of optical cavity. So, the single-mode and highly frequency-stabilized laser is required.

CHAPTER 5

CHAOS IN AN ACOUSTIC SYSTEM

5.1 Introduction

The chaotic or turbulent behavior seen in a physical system which is governed by deterministic equations has attracted intense interest recently. Ikeda et al. (1980) have pointed out that chaotic behavior can occur in an optically bistable system which is described by a differential-difference equation. By the differential-difference equation we mean a differential equation with delayed argument; namely an equation in the following form

$$\frac{dX(t)}{dt} = f(t, X(t), X(t - t_R)), \quad (5.1)$$

where $t_R > 0$ represents a delay time. The mathematical treatment of such equations is much more difficult than that of an ordinary differential equation because it is a kind of functional equation. But it often appears when we analyze a feedback control system because the existence of delay in the feedback loop is not rare. In physiological control system (homeostasis), such delay is unavoidable. The delay or lag time causes instabilities when one raises the feedback gain to improve the time response of the system. When a strong nonlinearity exists in the feedback loop, chaotic instabilities also occur. Some attempts have been made to ascribe some kinds of diseases to chaotic instabilities in physiological control systems (Mackey and Glass, 1977).

According to Ikeda's proposal, Gibbs et al. (1981) have

observed such chaos in an optical hybrid device with a delay in the feedback. In the recent article they showed their system takes the period-doubling route to chaos (Hopf et al., 1982). It is surprising that the period-doubling scenario seems to be realized in many different physical systems.

In this chapter we report the observation of Ikeda type instability and novel period-doubling bifurcations in a simple acoustic system composed of a microphone, a nonlinear circuit, an amplifier, and a loudspeaker.

5.2 A Differential-Difference Equation

Here we derive Ikeda's equation (Ikeda, 1979) for some simplified model; a ring cavity containing a very thin nonlinear

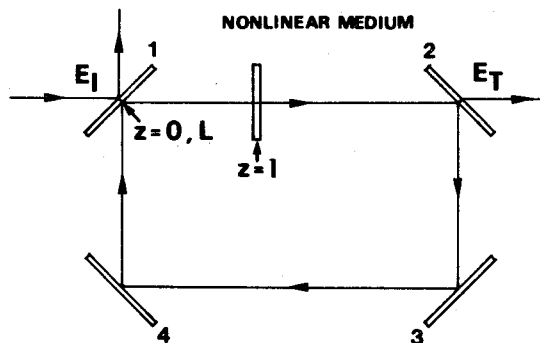


Fig. 5.1 Ring cavity containing a thin dielectric medium.

dielectric medium (Fig. 5.1). The position z is measured from mirror 1 along the optical path and the total length of the ring is L . Mirrors 1 and 2 have a reflectivity R and mirror 3 and 4 are perfectly reflecting. The slowly varying envelope of the electric field $\mathcal{E}(t, z)$ satisfies the boundary conditions:

$$\mathcal{E}(t, 0) = (1 - R)^{1/2} \mathcal{E}_I + \sqrt{R} \mathcal{E}(t, L), \quad (5.2a)$$

$$\mathcal{E}(t, L) = \sqrt{R} \mathcal{E}(t - \frac{L-1}{c}, 1 + 0) e^{-ik(L-1)}, \quad (5.2b)$$

$$\mathcal{E}(t, 1 + 0) = \mathcal{E}(t, 1 - 0) e^{i\theta(t)}, \quad (5.2c)$$

$$\mathcal{E}(t, 1 - 0) = \mathcal{E}(t - \frac{1}{c}, 0) e^{-ikl}, \quad (5.2d)$$

where $\mathcal{E}(t, 1 \neq 0)$ is the electric field at the input (output) of the medium, \mathcal{E}_I is the amplitude of the incident light. Equation (5.2c) means the phase shift caused by the medium is $\theta(t)$. From these equations we have

$$\mathcal{E}(t, 0) = (1-R)^{1/2} \mathcal{E}_I + R \mathcal{E}(t - \frac{L-1}{c}, 0) e^{-i(kL - \theta(t - \frac{L-1}{c}))}. \quad (5.3)$$

As for the dielectric medium we assume the dynamical equation:

$$d\theta(t)/dt = -\gamma\theta(t) + B|\mathcal{E}(t, 1)|^2, \quad (5.4)$$

where γ is the relaxation rate of the medium. This equation means that the medium has a quadratic dependence of refractive index on the electric field amplitude. Introducing new variables $E(t) = \sqrt{B} \mathcal{E}(t, 0)$, $A = \sqrt{B(1-R)} \mathcal{E}_I$, $B = R$, $t_R = L/c$, and $\varphi(t) = \theta(t - (L-1)/c)$, we have Ikeda's equation:

$$E(t) = A + BE(t - t_R) \exp(i[\varphi(t) - \varphi_0]), \quad (5.5a)$$

$$\gamma^{-1} d\varphi(t)/dt = -\varphi(t) + |E(t - t_R)|^2, \quad (5.5b)$$

where φ_0 is the cavity mistuning parameter.

In the case where $B \ll 1$, $A^2 B \sim O(1)$, Eqs. (5.5) are simplified as

$$\gamma^{-1} d\varphi(t)/dt = -\varphi(t) + A^2(1 + 2B \cos[\varphi(t - t_R) - \varphi_0]), \quad (5.6)$$

and $E(t)$ is given by $|E(t)|^2 = A^2(1 + 2B \cos[\varphi(t - t_R) - \varphi_0])$. This equation is essentially the same as that for the acoustic system we study in this chapter.

5.3 Experimental Setup

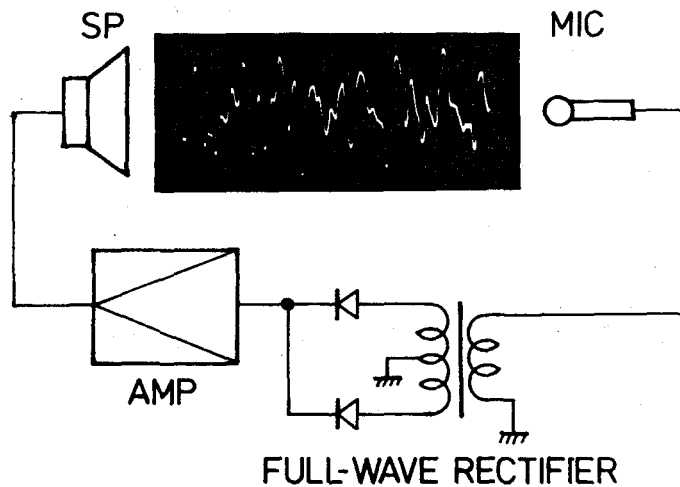


Fig. 5.2 Experimental setup. A microphone (MIC), a full-wave rectifier, an amplifier (AMP), and a loudspeaker (SP) form a feedback loop. An example of the chaotic-sound waveform is also shown.

The experimental setup of our acoustic system is shown in Fig. 5.2. The time delay t_R which plays a key role in inducing instabilities corresponds to the propagation time of sound from the speaker to the microphone which are faced about 13 cm apart ($t_R \sim 0.37$ ms). The other key element is a nonlinear circuit which has at least one peak in its input vs output characteristic curve. The most popular and easily constructed circuit having such a peak is a

full-wave rectifier.

We could hear chaotic oscillation when the amplifier gain was high enough, whereas without the rectifier only periodic oscillations could be observed. In the following experiment to observe the period-doubling bifurcations we used a rectifier with operational amplifiers (Graeme, 1973) which has more precise characteristics than the conventional two-diode rectifier in Fig. 5.2. The output V_y and the input V_x are related by the equation $V_y = -|V_x + V_{x0}| + V_{y0}$, where V_{x0} and V_{y0} are the input and output offset voltages respectively. As described later, adjustments of the offsets are needed to observe the period-doubling bifurcations.

By the analogy of our system to those in Refs. 1-3, we introduce the differential-difference equation

$$\tau^{-1} \frac{d}{dt} x(t) = -x(t) + \mu F_1(x(t-t_R)), \quad (5.7)$$

with

$$F_1(x) = -|x + 0.5| + 0.5, \quad (5.8)$$

where $x = V/2V_0$, V is the voltage fed to the speaker, V_0 is the input offset of the rectifier reduced to the speaker voltage, and μ is the loop gain. The response time τ^{-1} of the amplifier was set at about 0.15 ms.

In the experiment we set $V_{y0} = V_{x0}$ so that the condition $F_1(0) = 0$ is satisfied, which assures that $x = 0$ is an equilibrium point. The small-amplitude oscillation is expected to be almost symmetric with respect to the equilibrium point and to have a small dc component. Thus we can neglect the effect that the dc component cannot pass through the feedback loop in the actual system.

Equation (5.7) has the nonlinearity F_1 with a sharp peak

whereas Eq. (5.6) treated by Ikeda et al. (1980) and Gibbs et al. (1981) have round smooth peaks which are approximated by a quadratic function. In the theory of one-dimensional maps, these two types of function may be viewed as representatives (Ott, 1981).

5.4 Experimental Results

Our system shows various modes of oscillation, such as periodic oscillation with period $\sim 2(t_R + \tau^{-1})$ (~ 1.04 ms), oscillations with much smaller period, oscillations modulated with long period (~ 10 ms), chaotic oscillation, or intermittent chaotic oscillation, some of which are not expected from Eq. (5.7). Perhaps this is because we have neglected in Eq. (5.7) the low-frequency response of the system, phase shifts of the loudspeaker and the microphone, and the room acoustics. The appearance of each mode depends complicatedly on parameters such as the amplifier gain or the position of the microphone. However near the threshold we could observe the period-doubling bifurcations to chaos with good reproducibility.

We show an example of such bifurcations in Fig. 5.3. As the amplifier gain is increased, periodic oscillation (Fig. 5.3(a)) begins, which we may call "period-two" oscillation, for its period is about $2(t_R + \tau^{-1})$. Next the period doubling to period four (Fig. 5.3(b)) occurs. The bifurcation to period-eight (Fig. 5.3(c)) follows, but careful adjustment is needed to observe it. Usually the period-four seems to bifurcate directly to the chaotic oscillation (Fig. 5.3(d)).

Sometimes in the course of the bifurcations, low-frequency

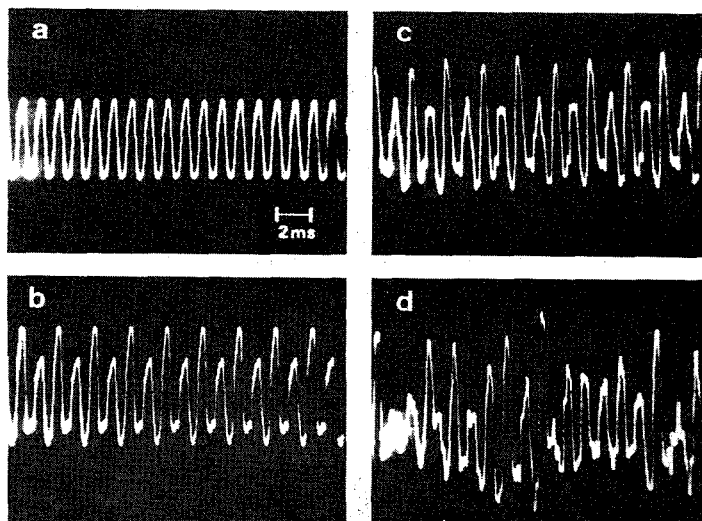


Fig. 5.3 The output voltage of the microphone. As the amplifier gain increased, (a) period-two, (b) period-four, (c) period-eight, and (d) chaotic oscillation appear successively.

oscillation (~ 100 Hz) begins to be superimposed and the bifurcation series is interrupted. Such a low-frequency instability can be removed by decreasing the low-frequency gain of the amplifier.

Figure 5.4 shows the bifurcation diagram obtained experimentally. The horizontal axis of a cathode-ray tube (CRT) is swept by the ramp voltage applied to the voltage-controlled amplifier (VCA) which is inserted in the feedback loop to vary the parameter μ slowly. The output of the microphone is applied to the vertical axis.

The horizontal trace on the left means that no oscillation takes place for small values of μ . Next we see the period-two oscillation builds suddenly up to a level determined by the offset of the rectifier. The top peaks and the bottom peaks of the period-two waveform (Fig. 5.3(a)) are seen as bright edges, whose

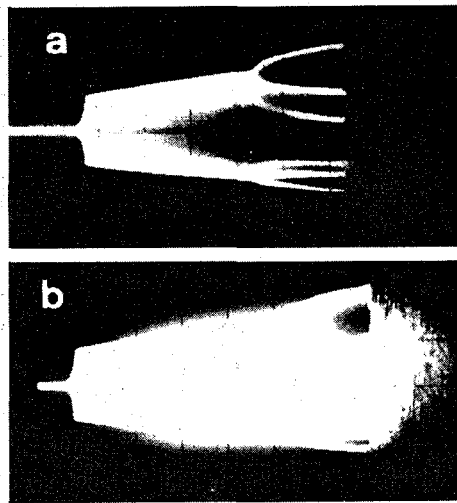


Fig. 5.4 (a) Bifurcation diagram, i.e., output voltage vs loop gain μ which is swept by VCA. (b) Same as (a) except the beam intensity of the CRT is increased to see the chaotic region.

separation corresponds to the amplitude of the oscillation. The enhancement of the edges takes place because the vertically oscillating beam-spot of the CRT moves slowly there.

As μ is increased one finds each edge splits into two branches which correspond to the four principal peaks of the period-four waveform in Fig. 5.3(b). The inmost two excess branches due to the subpeaks are also seen. The interval of the period-eight is too narrow to observe.

Next there comes the chaotic region which can hardly be seen in Fig. 5.4(a) for no enhancement on the CRT occurs. Increasing the beam intensity we can see the chaotic region (Fig. 5.4(b)).

5.5 Comparison with Theory

Let us return to Eq. (5.7). In the limit $t_{R1} \ll 1$, namely

when the time response of the system is extremely fast, Eq. (5.8) is reduced to a difference equation, or a one-dimensional map:

$$x_{n+1} = \mu F_1(x_n). \quad (5.9)$$

It is well known that when F_1 is replaced by a quadratic function such as $F_2 = -x(x - 1)$, the bifurcation diagram shows a series of pitchfork bifurcations at $\mu = \mu_k$ with period doubling by 2^k , $k = 1, 2, \dots$. There is an accumulation point μ_∞ to which $\{\mu_k\}$ converges, above which the chaotic behavior appears. This is a route to chaos seen in various physical systems (Appendix D). Another feature seen in the diagram is band merging or inverse bifurcation of the chaotic bands. As μ is increased, the chaotic bands merge in pairs successively until fully developed chaos appears. Schematically the bifurcations can be summarized as follows: $P_0 \rightarrow P_1 \rightarrow \dots \rightarrow (\text{onset of chaos}) \rightarrow \dots \rightarrow P_{(1)} \rightarrow P_{(0)}$, where P_k and $P_{(k)}$ represent the region of period- 2^k and that of period- 2^k chaos respectively.

For the map F_1 , which contains the absolute value function, the bifurcation diagram is quite different. In Fig. 5.5(a), we plotted the iterative values of x_n of Eq. (5.9) for each μ . We can see the bifurcations: $P_0 \rightarrow (\text{onset of chaos}) \rightarrow \dots \rightarrow P_{(1)} \rightarrow P_{(0)}$. Namely, the bifurcation points μ_k ($k = 1, 2, \dots$) are degenerate to a point $\mu = 1$. Thus the period-doubling bifurcations can't be seen and chaotic oscillation begins suddenly. The period-doubling bifurcations are observed experimentally in our system in spite of the nonlinearity F_1 . Perhaps it is because the condition $t_R \tau \gg 1$ to reduce Eq. (5.7) to Eq. (5.9) is not satisfied in our case.

We solved Eq. (5.7) numerically to see the effect of finite response time τ^{-1} on the bifurcation diagram. The diagrams in Fig.

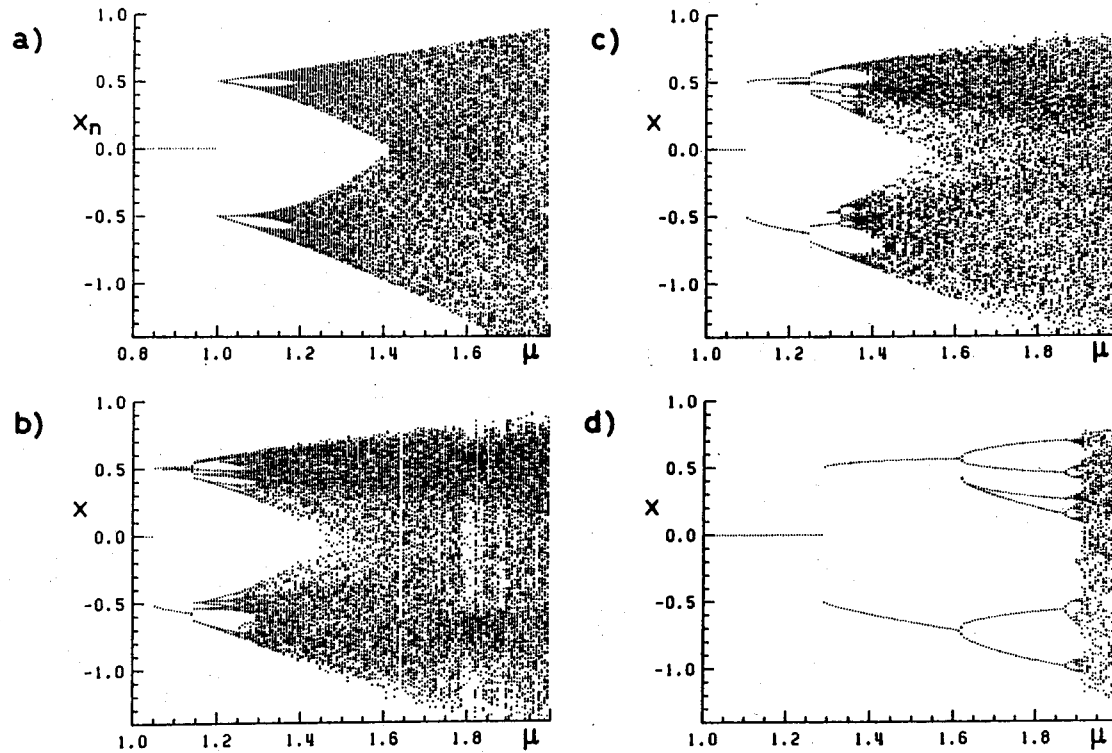


Fig. 5.5 (a) Bifurcation diagram for the difference equation (5.9): 150 successive plots of x_n after preiteration for each μ . Bifurcation diagrams for the differential-difference equation (5.7) with (b) $t_R \gamma = 9.0$, (c) $t_R \gamma = 6.0$, (d) $t_R \gamma = 3.0$. The figures are obtained by plotting the peak values of the stationary solution during $50t_R$ for each μ .

5.5(b)-(d) were obtained as follows. For each μ , we calculated the stationary solution $x(t)$ to Eq. (5.7) during $50t_R$. Then we picked up times t_p where $dx/dt(t_p) = 0$ and plotted the values $x(t_p)$. Although, as in the diagram obtained experimentally, there appear spurious branches due to subpeaks in $x(t)$, we can see how the bifurcations proceed as μ increased.

In the case of $t_R\gamma = 9.0$, the diagram (Fig. 5.5(b)) is fairly close to Fig. 5.5(a) except for the portion just after the first bifurcation. There appears the period-two region (P_1). The width of the upper branch comes from the subpeaks of the waveform not from the chaotic behavior. Above the second bifurcation we can see some band mergings of the chaotic oscillation as in Fig. 5.5(a).

It is interesting to note that the chaotic regime is changed to the ordered regime by the effect of γ . The newly appeared region may be $P_{(1)}$ not P_1 . The discrimination between them by numerical methods is very difficult but there is a reason to believe that it is P_1 as described later.

As increasing $t_R\gamma$, we can see the P_1 region extends and the transition to chaos is delayed. We also see the bifurcation to P_1 and that to P_2 (Fig. 5.5(c)). We note Fig. 5.5(d) for $t_R\gamma = 3$ is qualitatively similar to the diagram obtained in our experiment where $t_R\gamma$ is estimated to be ~ 2.5 .

The period-doubling bifurcations seen in Fig. 5.5(d) convince us that the newly appeared region is P_k ($k = 1, 2, 3$) rather than $P_{(k)}$ because the latter bifurcate inversely as μ is increased.

Another interesting feature in Fig. 5.5 is that as $t_R\gamma$ is decreased the periodic regions (P_k) extend at the expense of the chaotic regions ($P_{(k)}$). In Fig. 5.5(a) we see only P_0 as periodic region, whereas in Fig. 5.5(d) there seems only $P_{(0)}$ as chaotic

region.

5.6 Concluding Remarks

In summary, we have observed the Ikeda type instability in a simple acoustic system. The system bifurcates to chaos through some period doublings. The numerical analysis well explains the novel bifurcation diagram observed experimentally and shows that the bifurcation structure is sensible to the time response of the system. One of the matters to be clarified is the detailed structures near the onset of chaos, for example, whether the bifurcation series is truncated or not, and if not, what is the value of the Feigenbaum constant.

Inclusion of the low-frequency response to Eq. (5.7) is expected to give a better description of our system. It should be generalized as (Schumacher, 1983)

$$y(t) = \int_{-\infty}^t G(t - \tau)F(y(\tau))d\tau, \quad (5.10)$$

where $y(t)$ is the voltage output of the microphone, $F(y)$ is the nonlinear function, and $G(t)$ is the overall impulse response from the amplifier input to the microphone output. The impulse response satisfies

$$G(t) = 0 \quad (t \leq t_R). \quad (5.11)$$

Schumacher (1981) used the same type of equation in the analysis of autonomously oscillating musical instruments such as a flute and a violin.

CHAPTER 6

SYMMETRY-RECOVERING CRISES IN OPTICAL BISTABILITY

6.1 Introduction

The phenomenon of chaos has been the subject of intense interest in the last few years. It is now recognized as a common phase of a nonlinear dynamical system in addition to the conventional phases of stationary equilibrium and periodic (or quasi-periodic) oscillation. Since Ikeda et al. (1980) have predicted chaotic behaviors in an optically bistable system, many theoretical and experimental studies have been made (Ikeda and Akimoto, 1982; Ikeda et al., 1982; Gibbs et al., 1981; Hopf et al., 1982; Derstine et al., 1982; Derstine et al., 1983; Carmichael et al., 1983; Carmichael, 1983; Nakatsuka et al., 1983). Optical system is a suitable method with which to study nonlinear phenomena including chaos because it has tractable theoretical models and precise experiments are possible. If necessary, we can add moderate complexities to it (Poston et al., 1982; Moloney and Gibbs, 1982; McLaughlin, 1983). Along this line, we have proposed an optical system which utilizes interactions between right- and left-circularly polarized light beams through a $J = 1/2$ to $J = 1/2$ transition (Kitano et al., 1981a; Chapter 2). We have shown that symmetry breaking and optical tristability are possible for this system. Since then, various kind of phenomena have been predicted (Carmichael et al., 1983; Carmichael, 1983; Savage et al., 1982; Arecchi et al., 1983) and some of them have been demonstrated experimentally (Cecchi et al., 1982; Mitschke et al., 1983; Sandle

et al., 1983).

In Chapter 4, we proposed a new version of such polarization-related bistable system that utilizes optically induced Faraday effect and needs no optical cavity (Yabuzaki et al., 1983). We also performed the experiment by using a sodium cell and a multi-mode dye laser tuned to a wing of the D_1 line (Yabuzaki et al., 1984). An interesting feature of the system is that it exhibits the most typical pitchfork bifurcation which breaks the polarization symmetry. Namely the symmetry-breaking bifurcation is of a supercritical type, while in the tristable system discussed in Chapter 2, it is of a subcritical type. In this chapter we investigate the delay-induced chaos in this optical system. When we increase the input light intensity passing over the first bifurcation, a chaotic state having polarization asymmetry appears. If we increase the intensity still more, fully developed symmetric chaos is reached. Thus we are interested in the bifurcation which lies between those two states. As we will see later, the symmetry recovering occurs through a sudden change of the chaotic attractors. Recently Grebogi et al. (1982; 1983) have introduced a new class of bifurcation named "crises of chaos," where the size of chaotic attractor suddenly changes. We will show that in our case the symmetry is recovered through the crisis.

In Sec. 6.2, we show the setup of the system and derive the system equation which is a one-dimensional differential-difference equation having symmetry with respect to the exchange of two circular polarizations. In Sec. 6.3, we discuss a one-dimensional-map model and show a simple example of symmetry-recovering crisis. In Sec. 6.4, we describe the experimental setup of an electronic circuit to simulate the optical system. In the

experiment we observe three distinct types of symmetry-recovering crises. In Sec. 6.5, we introduce a two-dimensional-map model to explain the experimental results. Although the model seems to be oversimplified to approximate our system in an infinite-dimensional space, it can reproduce all three types of crises. We present the strange attractors near crises for each type, and discuss how they recover the symmetry. As we will see, unstable fixed points play important roles in crises. So we show the classification of fixed points of two-dimensional map in Appendix E. Finally, we summarize our results and discuss the remaining questions.

6.2 System Equation

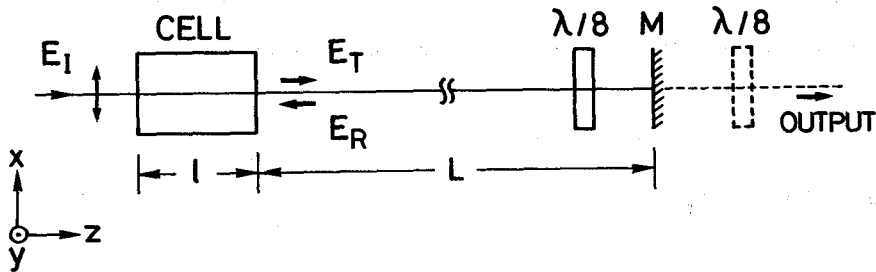


Fig. 6.1 Schematic illustration of the optically bistable system without an optical cavity.

We consider an optically bistable system shown in Fig. 6.1. It is largely the same as the one in Chapter 4 except that a delay in the feedback is introduced by taking a large distance L between the cell and the mirror (M). Following the model adopted for the previous chapters we consider spin-1/2 atoms which are optically pumped by the incident and the reflected light beams which are

tuned to the wing of the resonance line. The state of the ensemble of atoms can be characterized by the magnetization component M_z along the optical axis, which is proportional to the population difference between $m_j = 1/2$ and $m_j = -1/2$ sublevels in the ground state. The time evolution of M_z is described by the Bloch equation:

$$\frac{dM_z}{dt} = -(\Gamma + I_+ + I_-)M_z + (I_+ - I_-)M_0, \quad (6.1)$$

where Γ is the relaxation rate of the magnetization and I_{\pm} are the σ_{\pm} light intensities which are normalized so as to give pumping rates. If I_+ (I_-) is large enough compared to I_- (I_+) and Γ , all atoms are oriented along the $+z$ ($-z$) direction and the maximum polarization $M_z = M_0$ ($-M_0$) is attained.

The absorption coefficients α_{\pm} and the wavenumber k_{\pm} for σ_{\pm} light are determined by the normalized magnetization component $m_z = M_z/M_0$ as

$$\alpha_{\pm} = \alpha(1 \mp m_z), \quad (6.2)$$

$$k_{\pm} = k_0 + \kappa(1 \mp m_z), \quad (6.3)$$

where α and κ are the absorption coefficient and the incremental wavenumber for the unpolarized ($m_z = 0$) medium respectively, and k_0 is the wavenumber in a vacuum. In the dispersion regime we can neglect the absorption losses.

The polarization plane of the linearly polarized incident light is rotated by an angle θ when the difference between k_+ and k_- exists (Faraday rotation). If we represent the incident light

field as $\vec{E}_I = \sqrt{I_0} \hat{x}$, the transmitted field \vec{E}_T is given by

$$E_T = \sqrt{I_0} (\hat{x} \cos \theta + \hat{y} \sin \theta), \quad (6.4)$$

$$\theta(t) = (k_- - k_+)l/2 = m_z(t)\kappa l, \quad (6.5)$$

where l is the length of the cell and \hat{x} and \hat{y} are the unit vectors.

The transmitted light is reflected by the mirror M set at a distance L and is fed back to the cell. Thus the feedback is delayed by the amount $t_R = 2L/c$. In the feedback path, a $\lambda/8$ plate is inserted whose optic axis is oriented to the x axis. By its action, the polarization state of the light fed back to the cell becomes

$$\vec{E}_R = \sqrt{I_{R+}} \hat{e}_+ + \sqrt{I_{R-}} \hat{e}_-, \quad (6.6)$$

$$I_{R\pm} = RI_0 [1 \pm \sin 2\theta(t - t_R)]/2, \quad (6.7)$$

where $\hat{e}_\pm = (\hat{x} \mp i\hat{y})/\sqrt{2}$ and R is the reflectivity of the mirror. The σ_\pm components of the reflected light suffer complementary modulations according to $\sin 2\theta(t - t_R)$. Experimentally, the polarization state of \vec{E}_R can be observed by monitoring the output light transmitting through the mirror M and an auxiliary $\lambda/8$ plate. We can also monitor the polarization state \vec{E}_T by setting the fast axes of two $\lambda/8$ plates to form right angles. From Eqs. (6.7) and (6.5) we have the light intensities in the cell

$$I_{\pm} = (I_0/2) [(1 + R) \pm R \sin 2\kappa l m_z(t - t_R)]. \quad (6.8)$$

Substitution Eq. (6.8) into Eq. (6.1) gives the system equation:

$$\frac{dm_z}{dt} = -(\Gamma + 2I_0)m_z(t) + I_0 \sin 2\kappa l m_z(t - t_R), \quad (6.9)$$

where we set $R = 1$. Changing the time scale by $t' = \gamma^{-1}(\Gamma + 2I_0)t$ and introducing a new variable $X(t') = 2\kappa l m_z(t)$, we have a normalized form:

$$\gamma^{-1} \frac{dX}{dt'} = -X(t') + \mu \sin X(t' - t_R'), \quad (6.10)$$

where $\mu = 2\kappa l I_0 / (\Gamma + 2I_0)$ and $t_R' = \gamma^{-1}(\Gamma + 2I_0)t_R$. In the case $\Gamma \gg I_0$, μ is proportional to I_0 and t_R' is independent of I_0 . In the experiment we can vary $t_R'\gamma$ by changing the length L or the relaxation rate Γ . Hereafter we drop the primes in t' and t_R' . When $t_R'\gamma = 0$, Eq. (6.10) is an ordinary differential equation in one dimension, while in the limit $t_R'\gamma \gg 1$, the system can be described by a difference equation as described in the next section. Therefore the parameter $t_R'\gamma$ represents whether Eq. (6.10) is close to a difference equation or to a differential equation.

Note that Eq. (6.10) is invariant under the transformation $X \rightarrow -X$, which corresponds to the exchange of the roles of the spin-up and -down atoms, and the right- and left-circular polarized light.

6.3 One-Dimensional-Map Model

In the limiting case $t_R'\gamma \gg 1$, we can formally reduce Eq. (6.10) to the difference equation:

$$X_{n+1} = \mu \sin X_n, \quad (6.11)$$

which defines an iteration of one dimensional map. As is well known (Ikeda, 1979; Hopf et al., 1982; Chapter 5), this equation give an adequate qualitative prediction for the bifurcation structure for Eq. (6.10) with $t_{R\gamma} \gg 1$.

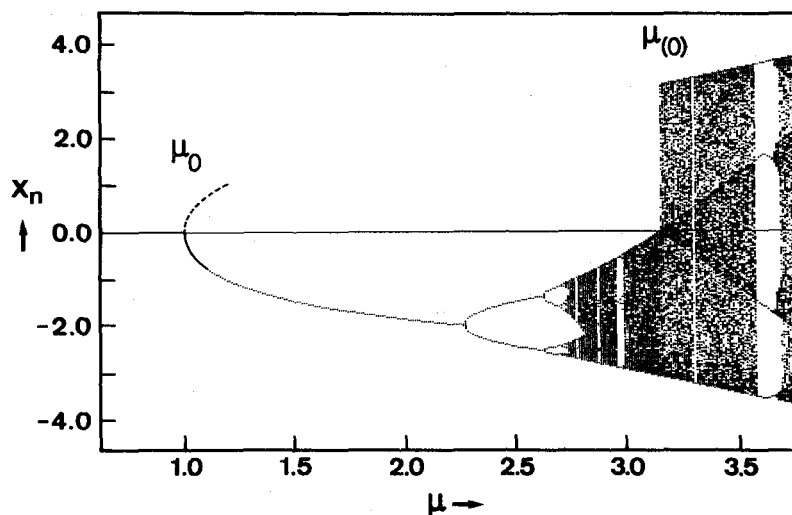


Fig. 6.2 Bifurcation diagram for the map, Eq. (6.11). For a given value of μ , an initial point is chosen and its orbit is plotted after preiteration to avoid transient phenomena. The same procedure is repeated for slightly increased value of μ , where the last point is used as the initial value. At $\mu = \mu_0 = 1$, a symmetry-breaking bifurcation occurs. For $\mu > \mu_0$, only the negative branch is pictured. The positive branch can be obtained by the transformation $X \rightarrow -X$. At $\mu = \mu_{(0)}$, a symmetry recovering is seen.

Figure 6.2 shows the bifurcation diagram for Eq. (6.11). For $\mu < \mu_0 = 1$, there exists only one stable fixed point $X = 0$. At $\mu = \mu_0$ a pitchfork bifurcation occurs at which the solution $X = 0$ becomes unstable and a symmetry-breaking transition takes place. This symmetry breaking can be seen also for the case $t_{R\gamma} = 0$ (Chapter 4). We pictured in Fig. 6.2 only the negative branch

after the bifurcation. As μ increases, each asymmetric branch undergoes period doublings followed by chaos. For $\mu < \mu_{(0)}$, the chaotic orbit is confined to the regions $X > 0$ or $X < 0$, namely, the output state is chaotic but still elliptically polarized to either direction. At $\mu = \mu_{(0)}$, the chaotic band suddenly doubles its width. There the two oppositely polarized bands collide to form a single band. Thus the symmetry broken at $\mu = \mu_0$ is recovered at $\mu = \mu_{(0)}$.

The sudden change may be viewed as "crisis" of chaos named by Grebogi et al. (1982; 1983). The crisis occurs when a strange attractor collides with a coexisting unstable fixed point or periodic orbit. In our case the situation is somewhat degenerate due to the symmetry, namely, a strange attractor collides with an unstable fixed point $X = 0$ and the other coexisting strange attractor simultaneously. We call the phenomenon "symmetry recovering crisis."

Figures 6.3(a) and (b) show examples of chaotic orbits for cases before ($\mu < \mu_{(0)}$) and after ($\mu > \mu_{(0)}$) the crisis. The short time behaviors are the same for both cases, but in the latter crossover to the other polarized state occurs sometimes. According to Grebogi et al. (1982; 1983), the average lifetime τ_{av} of each polarized state is estimated as

$$\tau_{av} \sim (\mu - \mu_{(0)})^{-1/2}. \quad (6.12)$$

We confirmed the estimation numerically.

6.4 Simulation by Analog Circuit

In order to see how the symmetry recovering crises for Eq.

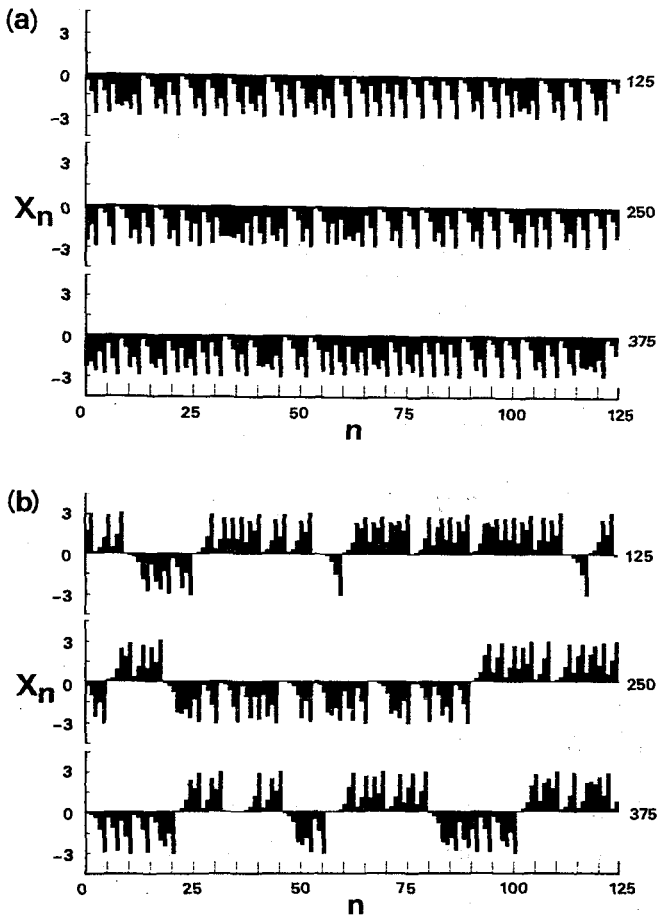


Fig. 6.3 Waveforms of Eq. (6.11) for (a) $\mu = 3.11$ (before the crisis) and (b) $\mu = 3.17$ (after the crisis). Bar graph of X_n as a function of n for 375 iteration after preiteration.

(6.10) appear we constructed an analog circuit which simulates Eq. (6.10). Figure 6.4 shows the experimental setup. The nonlinear function $\sin X$ in Eq. (6.10) is approximated by $X - X^3$ and realized by two analog multipliers (Intersil ICL8013) and an operational amplifier. The delay t_R is given by a digital delay line equipped with a 12-bit A-D, a D-A converter, and a 4096-word buffer. The cutoff frequency γ of the low-pass filter is set at 2 Hz when we record waveforms on a strip chart recorder. We can conveniently find bifurcation points or crises on a CRT instead of the recorder by setting $\gamma \sim 10^2 - 10^3$ Hz and shortening t_R correspondingly.

By changing t_R , we could find three distinct types of

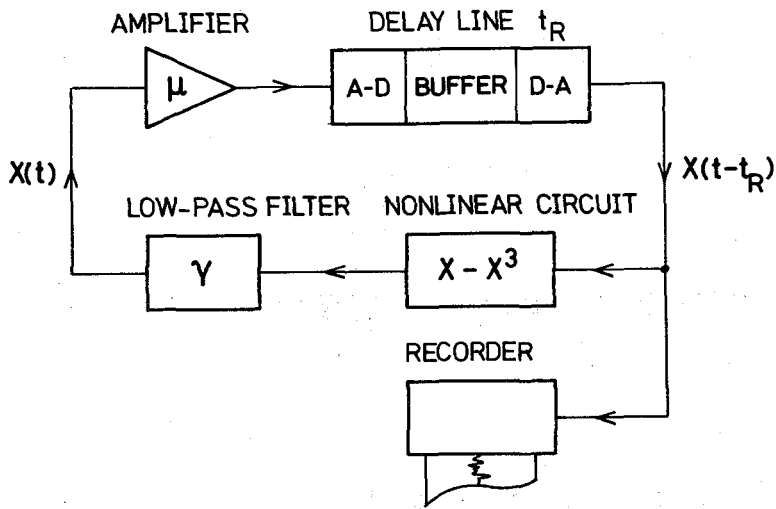


Fig. 6.4 Experimental setup. The analog circuit simulates the differential-difference equation (6.10).

symmetry-recovering crises. We named Type I, II, and III according to the order of the values t_R for which each type was observed. The critical value $\mu_{(0)}$ for crisis decreases as t_R increases.

Type I: Before the crisis, rather regular pulsing is observed (Fig. 6.5(a)). We can see damped oscillations near $X = 0$ between the pulses, whose durations are different from pulse to pulse. Such oscillation is not observed when μ is far below $\mu_{(0)}$ and appears as μ approaches $\mu_{(0)}$. After the crisis (Fig. 6.5(b)), the crossover to the other polarized state necessarily occurs through the damped oscillation. Thus the oscillation may be viewed as a precursor for the crisis and also as a crossover transient.

Type II: The waveform before the crisis (Fig. 6.6(a)) is fairly random. The bursts of periodic oscillation are precursors for the crisis. They appear at random and their duration is also random. After the crisis (Fig. 6.6(b)), the crossover occurs

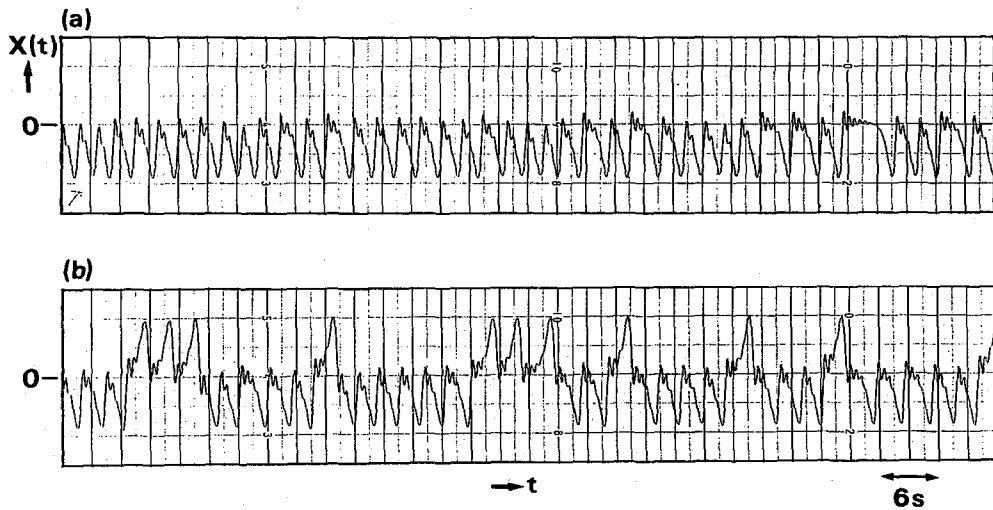


Fig. 6.5 Waveforms (a) before and (b) after the symmetry-recovering crisis of Type I. Parameters: $t_R = 0.41$ s, $\gamma = 2.0$ Hz, (a) $\mu = 4.26$; (b) $\mu = 4.38$.

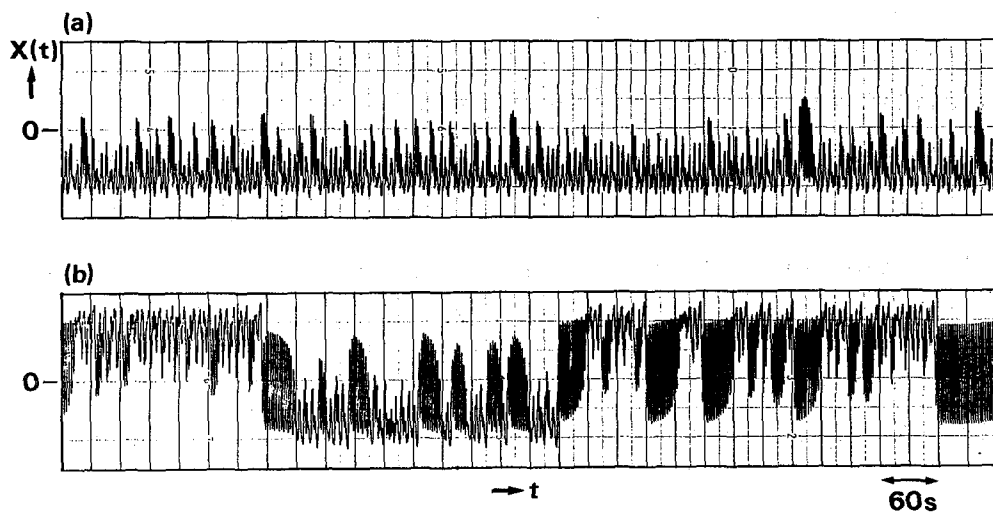


Fig. 6.6 Waveforms (a) before and (b) after Type II crisis. Parameters: $t_R = 2.05$ s, $\gamma = 2.0$ Hz, (a) $\mu = 2.96$; (b) $\mu = 3.02$.

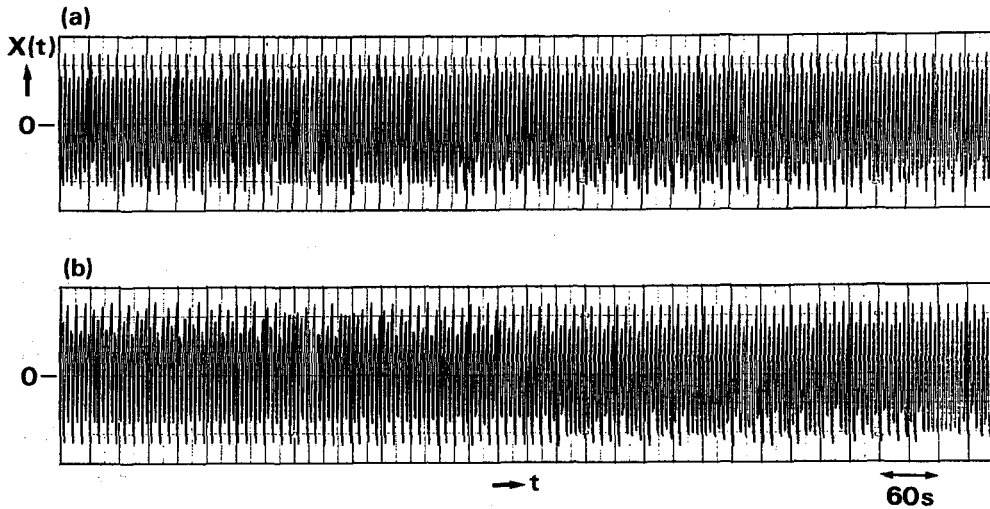


Fig. 6.7 Waveforms (a) before and (b) after Type III crisis. Parameters: $t_R = 4.10$ s, $\gamma = 2.0$ Hz, (a) $\mu = 2.77$; (b) $\mu = 2.79$.

through the burst of oscillation.

Type III: At a glance there seems to be no differences between Figs. 6.7(a) and 6.7(b). However the waveform in Fig. 6.7(a) shows period-4 chaos which has an asymmetry with respect to X ; the upper boundary is flat while the lower is not. In the middle of Fig. 6.7(b) we can see a crossover. No marked precursory phenomena nor crossover transients are seen for this type.

6.5 Two-Dimensional-Map Model

By the analog-circuit simulation we have confirmed symmetry-recovering crises exist for Eq. (6.10), as predicted by the one-dimensional-map model. However, the waveforms at the three types of crises were very different from that for the one-

dimensional map. In this section we introduce a two-dimensional difference equation and show the three types of crises occur for the equation with appropriate values of parameters.

We formally discretize Eq. (6.10) as

$$\gamma^{-1} \frac{X_{n+1} - X_n}{\Delta t} = -X_n + \mu F(X_{n-N}), \quad (6.13)$$

where N is an integer, $\Delta t = t_R/N$, $X_n = X(n\Delta t)$, and $F(X) = X(1 - X^2)$. By introducing a parameter $\alpha = \gamma\Delta t$, we obtain the following $(N + 1)$ -dimensional difference equation:

$$X_{n+1} = (1 - \alpha)X_n + \alpha\mu F(X_{n-N}), \quad (6.14)$$

In the limit $\alpha \rightarrow 0$, N and $t_R = \text{constant}$, Eq. (6.14) approximates the differential equation (6.10) with $t_R = 0$. For the case $\alpha = 1$, Eq. (6.14) reduces to the one-dimensional difference equation (6.11). So α is a parameter which connects a difference equation and a differential equation as $t_R\gamma$ does in Eq. (6.10).

Here we crudely set $N = 1$ in Eq. (6.14) and obtain a two dimensional difference equation (Kawakami, 1979):

$$X_{n+1} = (1 - \alpha)X_n + \alpha\mu F(Y_n), \quad (6.15a)$$

$$Y_{n+1} = X_n, \quad (6.15b)$$

where $Y_n = X_{n-1}$. The equation is invariant under the transformation $(X, Y) \rightarrow (-X, -Y)$.

Surprisingly we could find the three types of crises in this oversimplified equation. In Figs. 6.8, 6.9, and 6.10, we show the waveforms near the crises. The clear correspondences to Figs. 6.5;

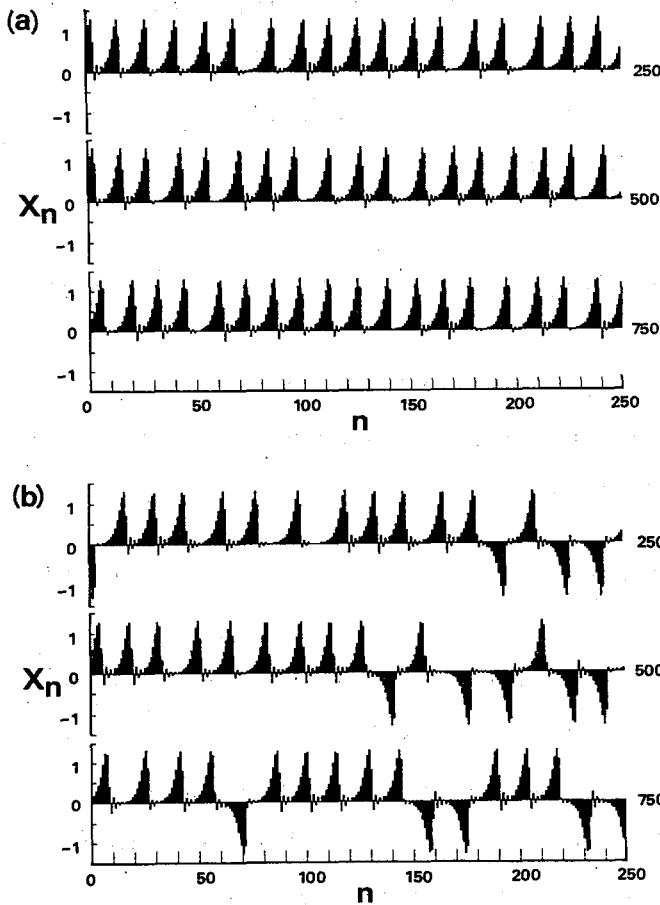


Fig. 6.8 Calculated waveforms (a) before and (b) after Type I crisis. Graph of X_n of Eq. (6.15) for 750 iteration after preiteration. Parameters: $\alpha = 0.1$, (a) $\mu = 10.24$; (b) $\mu = 10.30$.

6.6, and 6.7 are seen. Especially the same precursors and crossover transients appear for Types I and II. Type I was found for smaller values of α (near differential-equation limit), Type III was for $\alpha \lesssim 1$ (near difference-equation limit), and Type II was in the middle. The order is consistent with the results in the previous section.

As described in Sec. 6.3, for the one-dimensional map, the symmetry recovering crisis is undergone when a strange attractor collides with an unstable fixed point and the other strange attractor. Here we investigate the situation for the two-dimensional cases. Figure 6.11, 6.12, and 6.13 show the strange

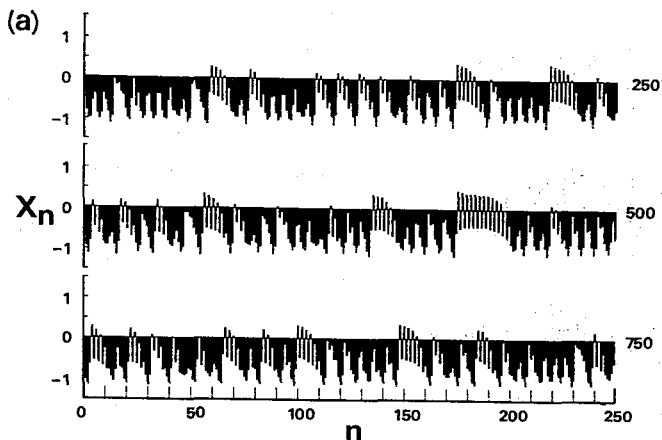
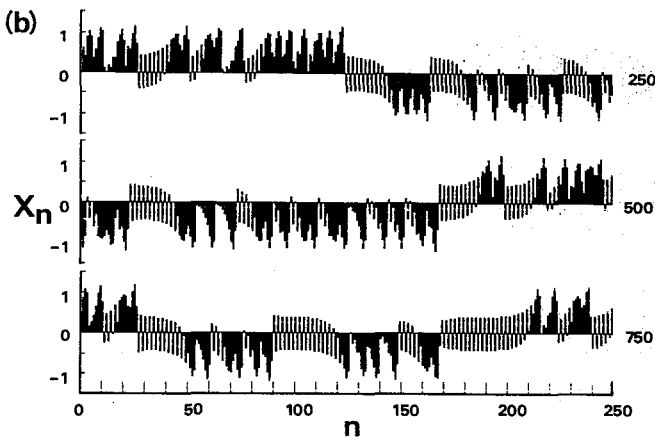


Fig. 6.9 Calculated waveforms (a) before and (b) after Type II crisis. Parameters: $\alpha = 0.5$, (a) $\mu = 3.54$; (b) $\mu = 3.57$.



attractors near the crises of Type I, II, and III respectively.

Type I: Figure 6.11(a) shows the strange attractor just before the crisis. The other coexisting attractor is obtained by the transformation $(X, Y) \rightarrow (-X, -Y)$. The two limit-cycle like attractors are about to touch each other near the origin. A round trip of the cycle forms a pulse in Fig. 6.8. At $\mu = \mu_{(0)}$, two attractors are merged and for $\mu < \mu_{(0)}$, an orbit on an attractor can go over to the other.

Figure 6.11(b) is an enlargement of part of Fig. 6.11(a). The two attractors are clearly separated. The regular structure of the attractors is a reflection of the existence of a fixed point $(0,0)$.

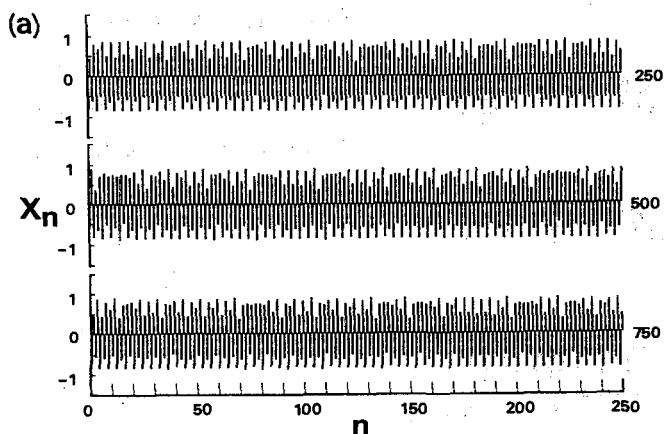
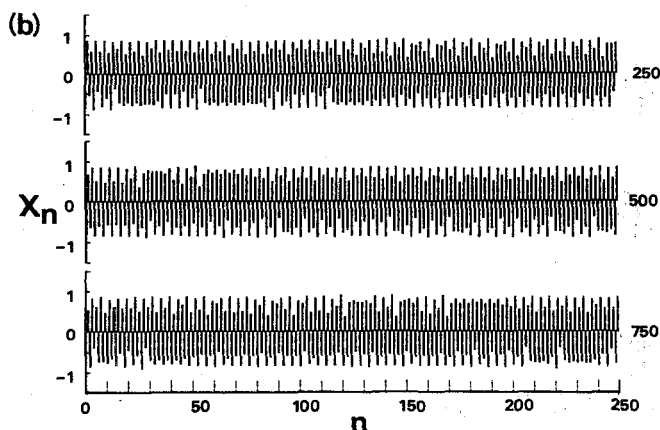


Fig. 6.10 Calculated waveforms (a) before and (b) after Type III crisis. Parameters: $\alpha = 0.85$, (a) $\mu = 2.944$; (b) $\mu = 2.946$.



of Eq. (6.15). By the stability analysis, we can see that the eigenvalues ρ_1, ρ_2 of the linearized map at $(0,0)$ satisfy the relations: $-1 < \rho_1 = -0.66 < 0, 1 < \rho_2 = 1.56$. The corresponding eigenvectors are $\vec{u}_1 = -0.66\hat{x} + \hat{y}, \vec{u}_2 = 1.56\hat{x} + \hat{y}$. According to the classification of the fixed points in Appendix D, the point $(0,0)$ is DR^1 for these parameter values. To simplify the situation, we consider a composite map $T^{(2)} = T \circ T$ where T is a map defined by Eq. (6.15). The point is a saddle (D^2) for $T^{(2)}$ since $0 < \rho_1^2 < 1 < \rho_2^2$. We use schematic illustrations in Fig. 6.14 to give general discussions. The point S is a saddle, and C_s and C_u are the stable and unstable invariant curves respectively. The eigenvectors \vec{u}_1

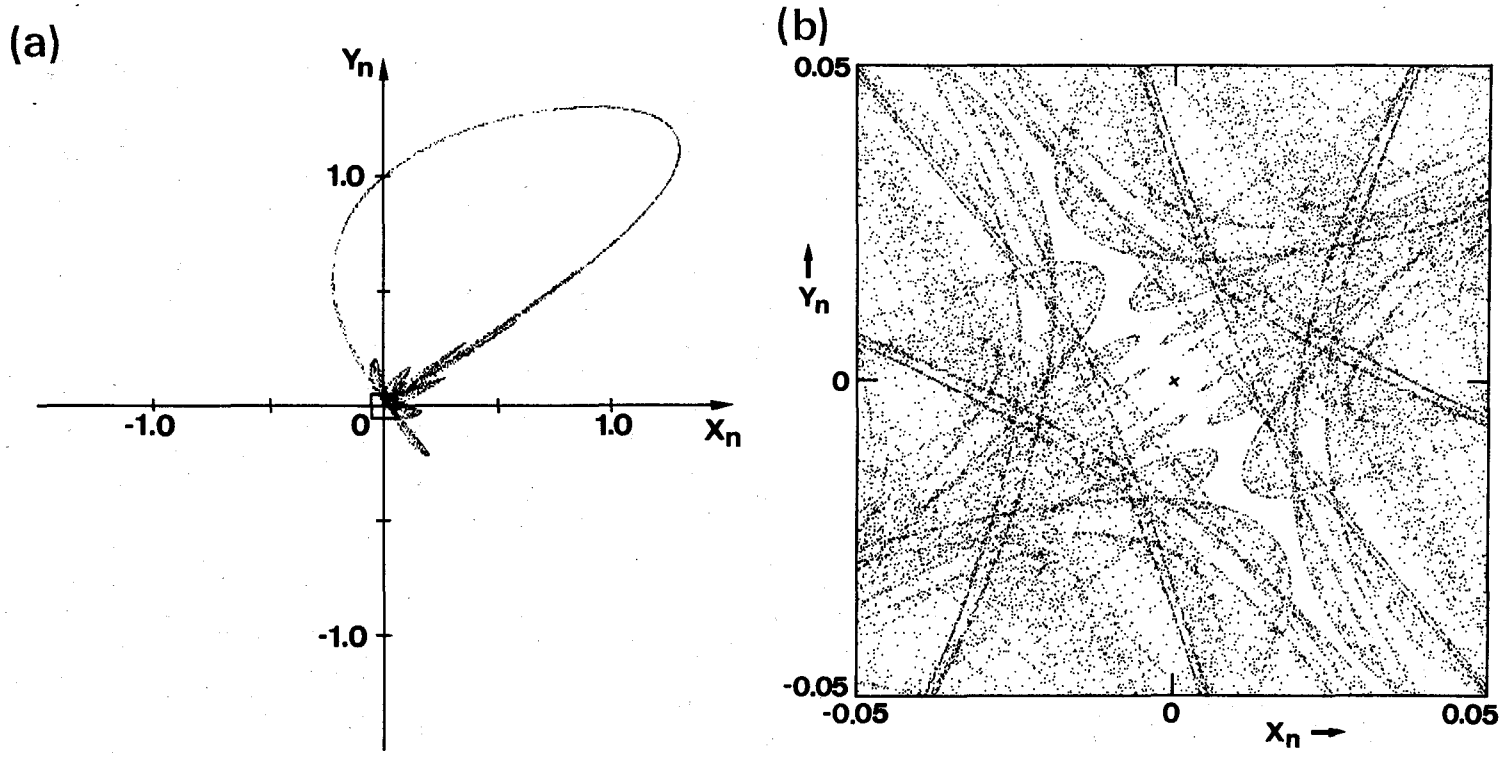


Fig. 6.11 (a) Chaotic attractor for Eq. (6.15) before Type I crisis. An initial point is chosen and its orbit is plotted after preiteration. The other coexisting attractor is obtained by the transformation $(X, Y) \rightarrow (-X, -Y)$. Parameters: $\alpha = 0.1, \mu = 10.24$.
 (b) Blowup of the boxed region in (a). Both coexisting attractors are plotted. A cross represents an unstable fixed point at $(0, 0)$. Parameters: $\alpha = 0.1, \mu = 10.244$.

and \vec{u}_2 are tangent to C_S and C_U at S . When $\mu < \mu_{(0)}$ (Fig. 6.14(a)), C_S is also the boundary separating the basins of attraction for the two attractors. The region R_1 , which is mapped from somewhere in the attractor, is mapped to R_2 , to R_3 , ..., successively, and at last repelled back along C_U . When the crisis is reached, R_1 touches the boundary C_S , as a result, R_i ($i = 2, 3, \dots$) touch C_S and R_∞ touches to S . As seen in Fig. 6.14(b), for $\mu \gtrsim \mu_{(0)}$, points in R_1 over C_S are repelled over to the other attractors along C_U after some iterations of the map.

Near the crisis, a point mapped close to C_S in R_1 will need many iterations to be repelled away from S , namely, the orbit is trapped to S temporarily. If S is a period- n point (a fixed point for $T^{(n)}$), one will observe n -periodic oscillation with some duration. Such phenomena will be seen as precursor of crisis when $\mu \lesssim \mu_{(0)}$ and as crossover transient when $\mu \gtrsim \mu_{(0)}$.

Type II: A wide-spread attractor is seen in Fig. 6.12(a). The other coexisting attractor lies symmetrically. The touch occurs near period-2 points (± 0.39 , ∓ 0.39), whose stability is D^2 . Figure 6.12(b) show a blowup, where we see the same structure as in Fig. 6.14(a). We can hardly see the regular structure in Fig. 6.12(a) because μ is not so close to $\mu_{(0)}$. The bursts of oscillation seen in Fig. 6.9 mean that the orbit is trapped to the period-2 points. The closer the point is dropped to the stable invariant curve, the longer the regular oscillation continues.

Type III: The situation is rather complicated than in Types I and II. Before the crisis, two four-piece strange attractors are coexisting. In Fig. 6.13(a), only the attractor (A_1, A_2, A_3, A_4) is pictured. The other attractor (A_1', A_2', A_3', A_4') is obtained

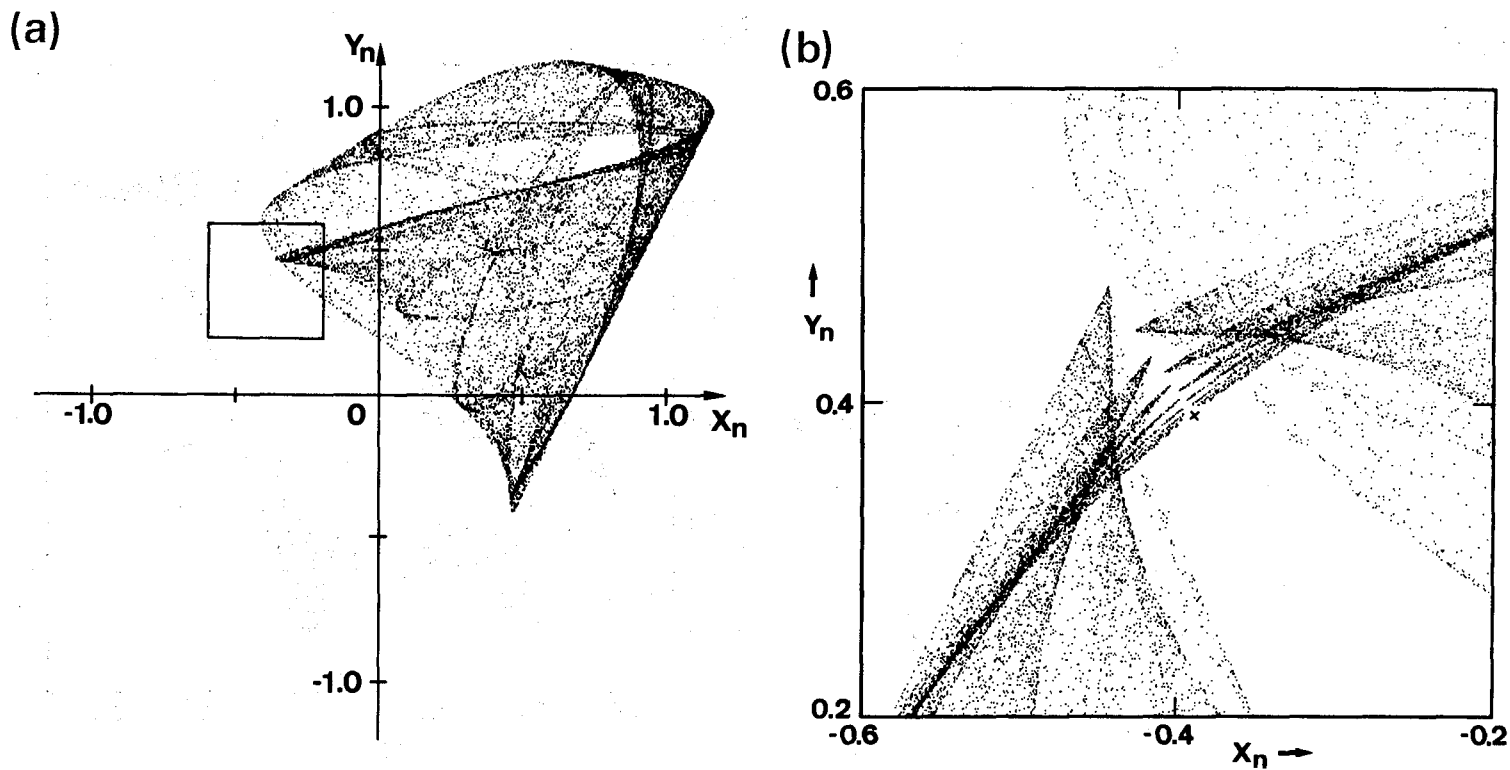


Fig. 6.12 (a) Chaotic attractor for Eq. (6.15) before Type II crisis. The other coexisting attractor is obtained by the transformation $(X, Y) \rightarrow (-X, -Y)$. Parameters: $\alpha = 0.5$, $\mu = 3.51$.

(b) Blowup of the boxed region in (a). Both coexisting attractors are plotted. Parameter μ is closer to $\mu_{(0)}$ than in (a). A cross represents one of unstable period-2 points at $(\pm 0.39, \mp 0.39)$. Parameters: $\alpha = 0.5$, $\mu = 3.541$.

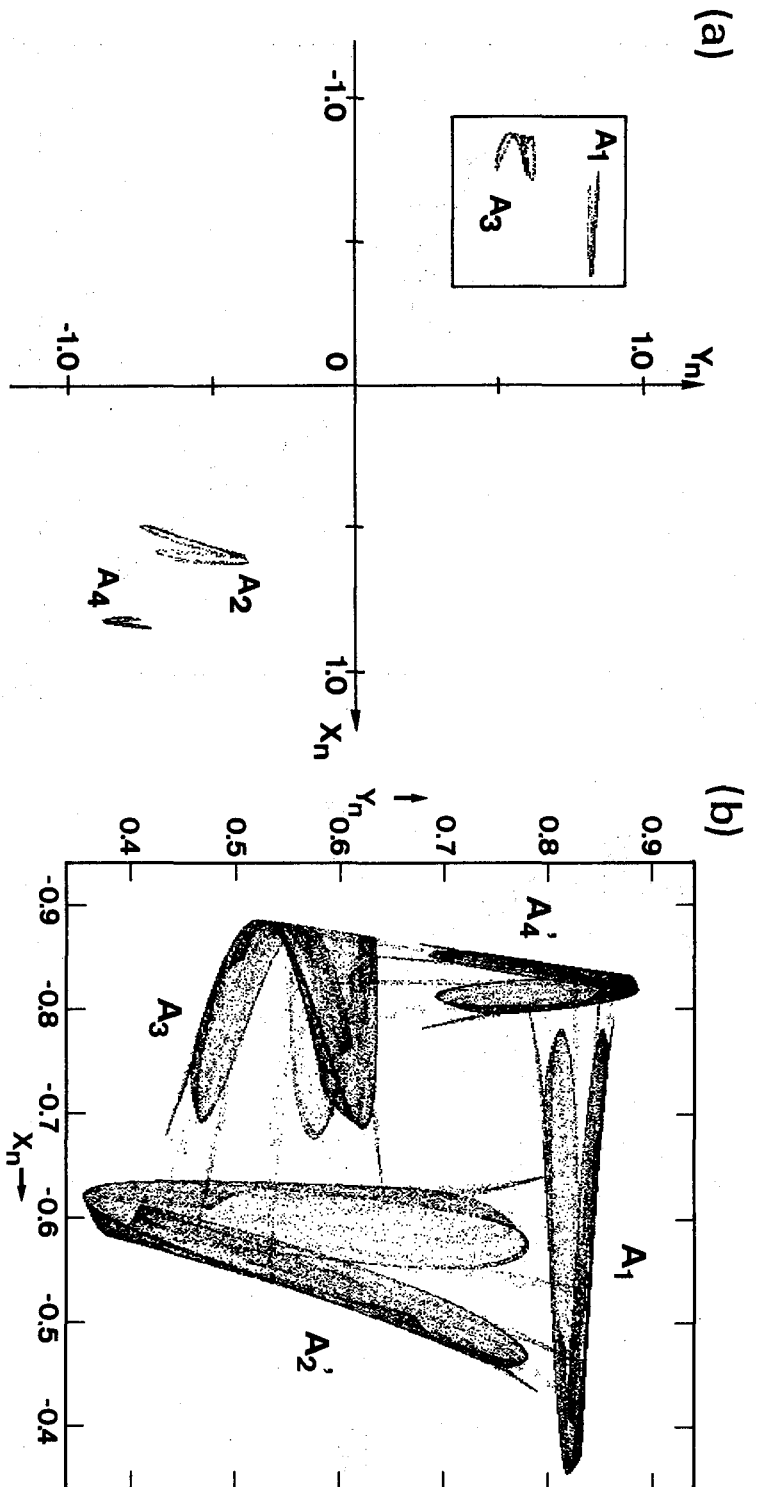


Fig. 6.13 (a) Four-piece chaotic attractor (A_1, A_2, A_3, A_4) for Eq. (6.15) before Type III crisis. The other coexisting attractor (A_1', A_2', A_3', A_4') is obtained by the transformation $(X, Y) \rightarrow (-X, -Y)$. Parameters: $\alpha = 0.85$, $\mu = 2.93$.

(b) Blowup of the boxed region in (a). Parameter μ is above the critical value for the crisis, therefore attractor pieces are merged to form a two-piece attractor. Parameters: $\alpha = 0.5$, $\mu = 2.946$.

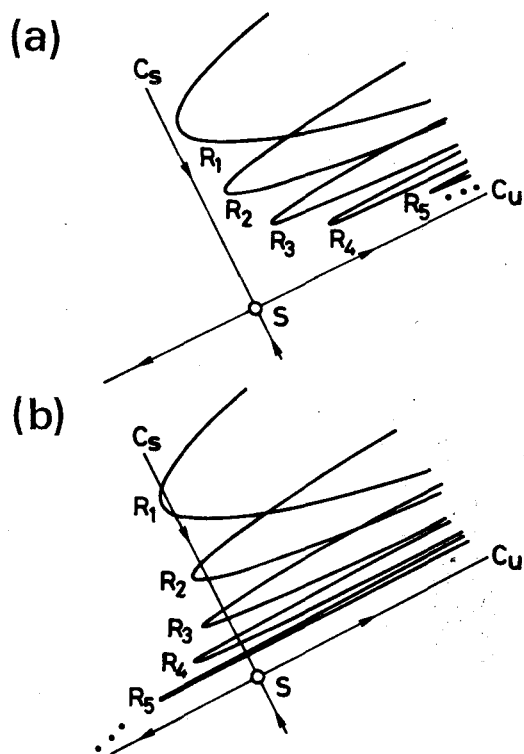


Fig. 6.14 Schematic illustration for crisis of chaotic attractor through a saddle point S. (a) Before and (b) after the crisis, the regions R_i are mapped to R_{i+1} . C_s and C_u represent the stable and unstable invariant curves of S respectively.

by the transformation $(X, Y) \rightarrow (-X, -Y)$. An orbit cycles as $A_1 \rightarrow A_2 \rightarrow A_3 \rightarrow A_4 \rightarrow A_1$ or as $A_1' \rightarrow A_2' \rightarrow A_3' \rightarrow A_4' \rightarrow A_1'$, and gives period-4 chaos as in Fig. 6.10(a). The flat boundary in the waveform comes from the fact that the attractor pieces A_4 and A_4' have narrower width in the X direction than the other pieces.

After the crisis occurs, the two attractors are merged as seen in Fig. 6.13(b). To see how the merging occurs a further blowup is given in Fig. 6.15. Between A_3 and A_2' , there exists an invariant curve C, which forms a part of the basin boundary before the crisis. We can see that the regions R_i ($i = 1, 2, \dots$) are mapped to R_{i+1} by $T^{(4)}$. In the course of iterations of the map, the regions are stretched in the direction across the curve C, and their tips are attracted to A_2' . The regions R_i ($i > 12$) can't be seen for the points are so dispersed by the stretching.

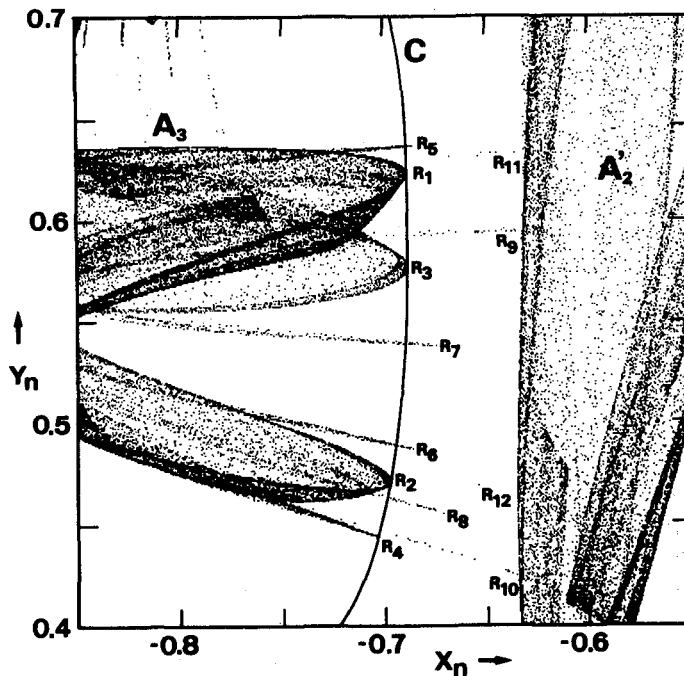


Fig. 6.15 Blowup of part between A_3 and A_2' of Fig. 6.13(b). Parameter μ is above $\mu_{(0)}$. The regions R_i are mapped to R_{i+1} by $T^{(4)}$. C represents an unstable invariant curve. Parameters: $\alpha = 0.85$, $\mu = 2.2447$.

The configuration of R_i along C can be understood as follows. Restriction $T^{(4)}$ to the invariant curve C gives a one-dimensional unimodal map which exhibits period-2 chaos. So the configuration of R_i is somewhat erratic, although we can group them into (R_{2n-1}) and (R_{2n}) ($n = 1, 2, \dots$).

It is seen, from the theory of unimodal map, that there exist infinite numbers of unstable fixed points on C; one UR^4 , two UR^8 , four UR^{16} , ... Therefore we may say the crisis occurs through UR^k ($k = 2n$, $n = 0, 1, 2, \dots$). Here, however, we are tempted to modify the Grebogi's definition of crises as "a collision of a chaotic attractor to the basin boundary."

6.6 Conclusions

In summary we have investigated the symmetry-recovering crises

of chaos in a spin-related optically bistable system. Through the crises, chaotic states having the polarization asymmetry, which is inherited from the first bifurcation, jumps back to a symmetric state. We have found three distinct types of the crises by changing the parameter $t_{R\gamma}$. All of the waveforms near these crises are very different from that for the one-dimensional-map model which has been used to analyze differential-difference equations such as Eq. (6.10). Whereas a two-dimensional-map model we introduced gives good qualitative explanations to the three types of crises.

As Grebogi et al. (1982; 1983) said, crises occurs when a chaotic attractor collides with an unstable fixed point or an unstable periodic orbit. In our cases of Types I, II, and III, collisions to the unstable fixed points of types DR^1 , D^2 , and UR^{4k} ($k = 2^n$) occur. For Types I and II unstable fixed point has a stable invariant curve in addition to an unstable invariant curve. The stable curve forms a part of the basin boundary which separate the paired chaotic attractors before the crisis. Along the stable invariant curve, regular structures are formed just before and after the crisis. For Type III, a one-dimensional map on the invariant curve, which yields chaos, gives marked structure to the strange attractors near the crisis.

Perhaps there exist other types of symmetry-recovering crises than those we treated here. (For example Fig. 3(c) in Arecchi and Lisi (1982) suggests another type which is close to Type III.) Some of them may need models in higher dimensions. Even for such cases, types of the unstable fixed point will characterize the crises. Statistical behavior near each crisis such as Eq. (6.12) should be investigated.

Finally we estimate experimental parameters to observe the phenomena in an all-optical system. The Na system of Chapter 4 with which we have observed the symmetry-breaking bifurcation should be modified. The delay t_R can be provided by an optical fiber with sufficient length L . We see from Eq. (6.10) and the requirement $t_R \gamma \gtrsim 1$ that the required power density I_0 is inversely proportional to t_R , or L . For $L = 1$ km ($t_R = 6$ μ s), I_0 is estimated to be $1 \sim 10$ W/mm², which is not unrealistic value considering the use of a multi-mode laser.

CHAPTER 7

CONCLUSIONS

In this thesis, theoretical and experimental studies have been made on the nonlinear phenomena which appear in the spin-related optically bistable and tristable systems. It has been shown that inclusion of polarization effects brings various new features which are not seen in the conventional bistable systems. In particular, the symmetry with respect to the light polarization plays an important role.

In Chapter 1, we have presented a short review of the theoretical and experimental studies on optical bistability. We have mentioned some phenomena which attract attentions and pointed out that the optical bistability is acquiring importance as a model to study nonlinear dynamics. We have also described an optical pumping process by using a simple atomic model and showed that it brings about nonlinearity in optical characteristics of the medium.

In Chapter 2, we have investigated the static behavior of a Fabry-Perot cavity containing atoms with degenerate Zeeman sublevels in the ground state. It has been shown that when the intensity of the linearly polarized incident light is increased, a symmetry-breaking bifurcation occurs at a critical level. Above the threshold, the output light turns to be circularly polarized in either direction. The symmetry breaking is of a subcritical type and therefore a double-loop hysteresis appears. The behavior of the system can be interpreted in terms of the butterfly catastrophe, when we vary the right- and left-circular components of the input

light independently.

In Chapter 3, we have predicted that the optically tristable system in Chapter 2 exhibits self-pulsing induced and controlled by a static magnetic field. The self-sustained spin precession is responsible for the phenomenon and can be described by a modified Bloch equation which includes a nonlinearity.

In Chapter 4, we have studied on a simple optically bistable system with no optical cavity and found that the behavior of this system is largely different from ordinary optical bistability reported so far. As incident light intensity I_0 is varied, the present system behaves with pitchfork bifurcation (or symmetry-breaking), which is in contrast with the ordinary optical bistability with hysteresis. We have shown that the present optical bistability can well be explained in context with the cusp catastrophe similarly to the ordinary one, different features being attributable to the different (orthogonal) cross sections of the steady state surface of the cusp catastrophe. In the present system, a hysteresis cycle can be obtained when one varies the offset angle θ_0 ; the angle between the optic axis of the $\lambda/8$ plate and the polarization plane of the incident light.

Theoretical study has been made on the behavior of the system under a static magnetic field applied perpendicularly to the beam axis, and we have found that the magnetization produced spontaneously by symmetry breaking precesses around the field without any external periodic forces.

We have carried out the experiments using sodium vapor, and we have been able to obtain the evidence that the system shows symmetry breaking, or pitchfork bifurcation, when the offset angle θ_0 is zero. Furthermore, a hysteresis cycle has been observed when

θ_0 is varied, as predicted by the theory.

In Chapter 5, we have observed the Ikeda type instability in a simple acoustic system which can be regarded as an acoustic analogue of optically bistable system. The system bifurcates to chaos through some period doublings. The numerical analysis well explains the novel bifurcation diagram observed experimentally and shows that the bifurcation structure is sensible to the time response of the system.

In Chapter 6, we have investigated the symmetry-recovering crises of chaos in the spin-related optically bistable system. Through the crises, chaotic states having the polarization asymmetry, which is inherited from the first bifurcation, jumps back to a symmetric state. We have found three distinct types of the crises by changing the parameter $t_{R\gamma}$. All of the waveforms near these crises are very different from that for the one-dimensional-map model which has been used to analyze difference-differential equations. A two-dimensional-map model introduced has been found to give good qualitative explanations to the three types of crises.

Crisis occurs when a chaotic attractor collides with an unstable fixed point or an unstable periodic orbit. In our cases of Types I, II, and III, collisions to the unstable fixed points of types DR^1 , D^2 , and UR^{4k} ($k = 2^n$) occur. For Types I and II unstable fixed point has a stable invariant curve in addition to an unstable invariant curve. The stable curve forms a part of the basin boundary which separates the paired chaotic attractors before the crisis. Along the stable invariant curve, regular structures are formed just before and after the crisis. For Type III, a one dimensional map on the invariant curve, which yields chaos, gives

marked structure to the strange attractors near the crisis.

APPENDIX A

OPTICAL PUMPING IN FOUR-LEVEL ATOMS

In this appendix we set up the atomic model from the first principles to treat the optical pumping process rigorously. We begin with an equation of motion of the density matrix for atoms with a $J = 1/2 \rightarrow 1/2$ transition (four-level model), which are irradiated by σ_+ and σ_- light simultaneously. The equation can be reduced to the Bloch equation for the ground-state spin \vec{m} when the light intensities are not so strong. We also show that in the absence of magnetic fields it can be reduced to the rate equation for the ground state populations N_+ and N_- .

When the atoms are pumped by two beams propagating in opposite directions, we must take the standing-wave structure into account. We show that a spatially averaged Bloch equation can be used in the cases where an atom moves many wavelengths before its spin evolves appreciably.

We also discuss on the propagation of light through the spin-polarized medium. We see that the circular dichroism and the circular birefringence are proportional to the spin component along the wave vector.

A.1 Optical Pumping in Four-Level Atoms

In order to formulate optical pumping process, we consider an ensemble of atoms with a $J=1/2 \rightarrow J=1/2$ transition, which is homogeneously broadened, namely all the atoms have a same transition frequency ω_0 . The state of each atom can be represented

by a density matrix:

$$\rho = \begin{bmatrix} \rho_{g+g+} & \rho_{g+g-} & \rho_{g+e+} & \rho_{g+e-} \\ \rho_{g-g+} & \rho_{g-g-} & \rho_{g-e+} & \rho_{g-e-} \\ \rho_{e+g+} & \rho_{e+g-} & \rho_{e+e+} & \rho_{e+e-} \\ \rho_{e-g+} & \rho_{e-g-} & \rho_{e-e+} & \rho_{e-e-} \end{bmatrix}, \quad (\text{A.1})$$

where the diagonal element ρ_{ii} represents the probability that we find an atom in the level $|i\rangle$ and the conservation law asserts

$$\sum_i \rho_{ii} = 1 \quad (i = g+, g-, e+, e-). \quad (\text{A.2})$$

The off-diagonal elements ρ_{ij} ($i \neq j$) represent the coherence between the levels $|i\rangle$ and $|j\rangle$, and satisfy following relations:

$$\rho_{ji}^* = \rho_{ij} \quad (i, j = g+, g-, e+, e-). \quad (\text{A.3})$$

As will be seen later, the coherence between Zeeman sublevels of the ground or excited states is related to the transverse magnetic-dipole moment, whereas the coherence between the ground and excited states, such as $\rho_{g+,e+}$, $\rho_{g+,e-}$, ... is related to the electric-dipole moment oscillating at the optical frequency.

The time evolution of ρ can be described by the equation of motion:

$$i\hbar \frac{d\rho}{dt} = [\mathcal{X}, \rho] + i\hbar \left[\frac{d\rho}{dt} \right]_{\text{relax}}, \quad (\text{A.4})$$

where \mathcal{X} is the Hamiltonian and $(d\rho/dt)_{\text{relax}}$ represents the relaxation due to the spontaneous decay or atomic collisions. The Hamiltonian \mathcal{X} is decomposed as follows:

$$\mathcal{X} = \mathcal{X}_0 + \mathcal{X}_m + \mathcal{X}_{\text{opt}}, \quad (\text{A.5})$$

where \mathcal{X}_0 is the unperturbed Hamiltonian. The terms \mathcal{X}_m and \mathcal{X}_{opt}

represent the perturbations due to external magnetic fields and light fields respectively. The unperturbed Hamiltonian X_0 is represented as

$$X_0 = \begin{bmatrix} 0 & & & \\ & 0 & & \\ & & \hbar\omega_0 & \\ & & & \hbar\omega_0 \end{bmatrix}. \quad (\text{A.6})$$

The magnetic Hamiltonian X_m under a static magnetic field \vec{H}_0 is

$$X_m = -\gamma \vec{J} \cdot \vec{H}_0 = -\frac{\hbar}{2} \gamma \begin{bmatrix} \vec{\sigma} & 0 \\ 0 & \vec{\sigma} \end{bmatrix} \vec{H}_0, \quad (\text{A.7})$$

where γ is the gyromagnetic ratio and \vec{J} is the angular momentum operator. The vector $\vec{\sigma}$ is composed of three 2x2 matrices σ_x , σ_y , and σ_z which are Pauli's spin matrices:

$$\sigma_x = \begin{bmatrix} 0 & 1 \\ 1 & 0 \end{bmatrix}, \quad \sigma_y = \begin{bmatrix} 0 & -i \\ i & 0 \end{bmatrix}, \quad \sigma_z = \begin{bmatrix} 1 & 0 \\ 0 & -1 \end{bmatrix}. \quad (\text{A.8})$$

For simplicity, we assume that the magnetic field \vec{H}_0 is applied along the y axis, i.e. $\vec{H}_0 = \hat{y}(0, H_0, 0)$.

Under the electric-dipole-interaction approximation, X_{opt} can be written as

$$X_{\text{opt}} = -\vec{p} \cdot \vec{E}(t), \quad (\text{A.9})$$

where \vec{p} is the dipole moment operator and \vec{E} is the electric field of the laser beam, which is propagated along the z axis. With use of the circular basis vector, \vec{E} is represented as

$$\vec{E}(t) = \hat{e}_+ \mathcal{E}_+(t) e^{i\omega t} + \hat{e}_- \mathcal{E}_-(t) e^{i\omega t} + \text{c.c.}, \quad (\text{A.10})$$

where $\mathcal{E}_+(t)$ and $\mathcal{E}_-(t)$ are the complex amplitudes of σ_+ and σ_- components of light respectively, and ω is the frequency of the laser. The circular basis vectors \hat{e}_\pm are defined as follows:

$$\hat{e}_{\pm} = (\hat{x} \mp i\hat{y})/\sqrt{2}. \quad (\text{A.11})$$

The dipole moment \vec{p} for a $J=1/2 \rightarrow 1/2$ transition is (Condon and Shortley, 1970)

$$\vec{p} = p \begin{bmatrix} \hat{z}' & \hat{e}_+ \\ \hat{e}_- & -\hat{z}' \\ \hat{z}' & \hat{e}_+ \\ \hat{e}_- & -\hat{z}' \end{bmatrix}, \quad (\text{A.12})$$

where p is the modulus of the dipole moment and $\hat{z}' = \hat{z}/\sqrt{2}$.

From Eqs. (A.10) and (A.12), χ_{opt} becomes

$$\chi_{\text{opt}} = -p \begin{bmatrix} \xi_- e^{+i\omega t} \\ \xi_+ e^{+i\omega t} \\ \xi_+^* e^{-i\omega t} \\ \xi_-^* e^{-i\omega t} \end{bmatrix}. \quad (\text{A.13})$$

Here we have used a 'rotating-wave approximation,' namely neglected the influence of the σ_+ light to $\Delta m = -1$ transition and σ_- to $\Delta m = +1$.

The relaxation term $(dp/dt)_{\text{relax}}$ in Eq. (A.4) is introduced phenomenologically. Each component is given as follows:

$$\rho_{g+g+}: 1/3\gamma_e \rho_{e+e+} + 2/3\gamma_e \rho_{e-e-} - \Gamma_g/2(\rho_{g+g+} - \rho_{g-g-}), \quad (\text{A.14a})$$

$$\rho_{g-g-}: 1/3\gamma_e \rho_{e-e-} + 2/3\gamma_e \rho_{e+e+} - \Gamma_g/2(\rho_{g-g-} - \rho_{g+g+}), \quad (\text{A.14b})$$

$$\rho_{e+e+}: -\gamma_e \rho_{e+e+} - \Gamma_e/2(\rho_{e+e+} - \rho_{e-e-}), \quad (\text{A.14c})$$

$$\rho_{e-e-}: -\gamma_e \rho_{e-e-} - \Gamma_e/2(\rho_{e-e-} - \rho_{e+e+}), \quad (\text{A.14d})$$

$$\dot{\rho}_{g+g-} = -\Gamma_g \rho_{g+g-} \quad (\text{A.14e})$$

$$\dot{\rho}_{e+e-} = -\Gamma_e \rho_{e+e-}, \quad (\text{A.14f})$$

$$\dot{\rho}_{giej} = -\gamma_{eg} \rho_{giej} \quad (i, j = +, -), \quad (\text{A.14g})$$

where γ_e and γ_{eg} are the rate for the spontaneous and collisional decay of the population and that of the optical coherence, respectively. We have assumed the relaxation processes are isotropic. We have also assumed the relaxation in the Zeeman multiplets of the ground state and the excited state are isotropic (Manabe, 1979; Omont, 1977) and their rates are Γ_g and Γ_e , respectively.

Now we can write down the equation of motion (A.4) explicitly by using Eqs. (A.5) and (A.14);

$$\begin{aligned} \dot{\rho}_{g+g+} = & \frac{1}{3}\gamma_e \rho_{e+e+} + \frac{2}{3}\gamma_e \rho_{e-e-} - \frac{1}{2}\Gamma_g (\rho_{g+g+} - \rho_{g-g-}) \\ & + \frac{Q_0}{2} (\rho_{g-g+} + \rho_{g+g-}) - ig(\mathcal{E}_- e^{i\omega t} \rho_{e-g+} - \mathcal{E}_-^* e^{-i\omega t} \rho_{g+e-}), \end{aligned} \quad (\text{A.15a})$$

$$\begin{aligned} \dot{\rho}_{e+e+} = & -\gamma_e \rho_{e+e+} - \frac{1}{2}\Gamma_e (\rho_{e+e+} - \rho_{e-e-}) \\ & + \frac{Q_0}{2} (\rho_{e-e+} + \rho_{e+e-}) - ig(\mathcal{E}_+^* e^{-i\omega t} \rho_{g-e+} - \mathcal{E}_+ e^{i\omega t} \rho_{e+g-}), \end{aligned} \quad (\text{A.15b})$$

$$\begin{aligned} \dot{\rho}_{g+g-} = & -\Gamma_g \rho_{g+g-} + \frac{Q_0}{2} (\rho_{g-g-} - \rho_{g+g+}) \\ & - ig(\mathcal{E}_- e^{i\omega t} \rho_{e-g-} - \mathcal{E}_+^* e^{-i\omega t} \rho_{g+e+}), \end{aligned} \quad (\text{A.15c})$$

$$\begin{aligned} \dot{\rho}_{ete-} = & -\Gamma_e \rho_{ete-} + \frac{Q_0}{2} (\rho_{e-e-} - \rho_{ete+}) \\ & - ig(\xi_+^* e^{-i\omega t} \rho_{g-e-} - \xi_- e^{i\omega t} \rho_{e+g+}), \end{aligned} \quad (\text{A.15d})$$

$$\begin{aligned} \dot{\rho}_{g+e+} = & -\gamma_{eg} \rho_{g+e+} + i\omega_0 \rho_{g+e+} + \frac{Q_0}{2} (\rho_{g-e+} + \rho_{g+e-}) \\ & - ig(\xi_- \rho_{e-e+} - \xi_+ \rho_{g+g-}) e^{i\omega t}, \end{aligned} \quad (\text{A.15e})$$

$$\begin{aligned} \dot{\rho}_{g-e+} = & -\gamma_{eg} \rho_{g-e+} + i\omega_0 \rho_{g-e+} + \frac{Q_0}{2} (\rho_{g+e+} + \rho_{g-e-}) \\ & - ig\xi_+ (\rho_{ete+} - \rho_{g-g-}) e^{i\omega t}, \end{aligned} \quad (\text{A.15f})$$

where $g = p/\hbar$, $\dot{} = d/dt$, and $Q_0 = \gamma H_0$. Alternation between + and - in subscripts gives three more independent equations. (For Eqs. (A.15a) and (A.15b), Q_0 should be replaced by $-Q_0$ additionally.)

Hereafter such alternation is assumed implicitly. If we introduce $\tilde{\rho}_{giej}$ as $\rho_{giej} = \tilde{\rho}_{giej} e^{i\omega t}$, ($i, j = +, -$), Eqs. (A.15e) and (A.15f) become

$$\begin{aligned} \dot{\tilde{\rho}}_{g+e+} = & [-\gamma_{eg} + i\delta] \tilde{\rho}_{g+e+} + \frac{Q_0}{2} (\tilde{\rho}_{g-e+} + \tilde{\rho}_{g+e-}) \\ & - ig(\xi_- \rho_{e-e+} - \xi_+ \rho_{g+g-}), \end{aligned} \quad (\text{A.16a})$$

$$\begin{aligned} \dot{\tilde{\rho}}_{g-e+} = & [-\gamma_{eg} + i\delta] \tilde{\rho}_{g-e+} + \frac{Q_0}{2} (\tilde{\rho}_{g+e+} + \tilde{\rho}_{g-e-}) \\ & - ig\xi_+ (\rho_{ete+} - \rho_{g-g-}). \end{aligned} \quad (\text{A.16b})$$

where $\delta = \omega_0 - \omega$. In the rate-equation limit $\gamma_{eg} \gg (1/\xi_i)(\partial\xi_i/\partial t)$, ($i = +, -$), we can set $d\tilde{\rho}_{giej}/dt = 0$, ($i, j = +, -$) and obtain

$$\tilde{\rho}_{g+e+} = ig[-\gamma_{eg} + i\delta]^{-1}(\mathcal{E}_- \rho_{e-e+} - \mathcal{E}_+ \rho_{g+g-}), \quad (\text{A.17a})$$

$$\tilde{\rho}_{g-e+} = ig[-\gamma_{eg} - i\delta]^{-1} \mathcal{E}_+ (\rho_{e+e+} - \rho_{g+g+}). \quad (\text{A.17b})$$

We have also assumed $\gamma_{eg} \gg Q_0$. Substitution Eqs. (A.17) into Eqs. (A.15a)-(A.15c) yields

$$\begin{aligned} \dot{\rho}_{g+g+} = & \frac{1}{3}\gamma_e \rho_{e+e+} + \frac{2}{3}\gamma_e \rho_{e-e-} - \frac{1}{2}\Gamma_g (\rho_{g+g+} - \rho_{g-g-}) \\ & + \frac{Q_0}{2}(\rho_{g-g+} + \rho_{g+g-}) - 2g^2 |\mathcal{E}_-|^2 L(\delta, \gamma_{eg}) \rho_{g+g+}, \end{aligned} \quad (\text{A.18a})$$

$$\begin{aligned} \dot{\rho}_{g+g-} = & -\Gamma_g \rho_{g+g-} + \frac{Q_0}{2}(\rho_{g-g-} - \rho_{g+g+}) \\ & - 2g^2 [(|\mathcal{E}_+|^2 + |\mathcal{E}_-|^2) L(\delta, \gamma_{eg}) \\ & - i(|\mathcal{E}_+|^2 - |\mathcal{E}_-|^2) D(\delta, \gamma_{eg})] \rho_{g+g-}, \end{aligned} \quad (\text{A.18b})$$

$$\begin{aligned} \dot{\rho}_{e+e+} = & -\gamma_e \rho_{e+e+} - \frac{1}{2}\Gamma_e (\rho_{e+e+} - \rho_{e-e-}) \\ & + \frac{Q_0}{2}(\rho_{e-e+} + \rho_{e+e-}) + 2g^2 |\mathcal{E}_+|^2 L(\delta, \gamma_{eg}) \rho_{g-g-}, \end{aligned} \quad (\text{A.18c})$$

where $L(x,y) = y/(x^2 + y^2)$, $D(x,y) = x/(x^2 + y^2)$. We have neglected some terms including ρ_{e+e+} and ρ_{e-e-} assuming $\gamma_e \gg g^2 |\mathcal{E}_\pm|^2$.

Furthermore if we assume $\gamma_e \gg \rho_{eiej}^{-1} (d/dt) \rho_{eiej}$, ($i, j = +, -$) then we can write ρ_{e+e+} and ρ_{e-e-} in terms of ρ_{g+g+} and ρ_{g-g-} as follows:

$$\dot{\rho}_{e+e+} = 2g^2 \frac{(\Gamma_e + \gamma_e) |\mathcal{E}_+|^2 \rho_{g-g-} + \Gamma_e |\mathcal{E}_-|^2 \rho_{g+g-}}{\gamma_e (2\Gamma_e + \gamma_e)} L(\delta, \gamma_{eg}) \quad (\text{A.19})$$

Substituting of Eq. (A.19) into Eq. (A.18a), we have

$$\begin{aligned} \dot{\rho}_{g+g+} = & -\frac{1}{2}\Gamma_g (\rho_{g+g+} - \rho_{g-g-}) + \frac{Q_0}{2} (\rho_{g-g+} + \rho_{g+g-}) \\ & + 2fg^2 L(\omega_0 - \omega, \gamma_{eg}) (|\mathcal{E}_+|^2 \rho_{g-g-} - |\mathcal{E}_-|^2 \rho_{g+g+}), \end{aligned} \quad (\text{A.20})$$

where

$$f = \frac{\Gamma_e / \gamma_e + 3/2}{2(\Gamma_e / \gamma_e) + 1}, \quad (\text{A.21})$$

is pumping efficiency which we shall set 1/2 assuming $\Gamma_e / \gamma_e \gg 1$, hereafter.

Equations (A.18b) and (A.20) are the equations of motion reduced to the ground state. The first and second terms of each equation represent the Zeeman relaxation and the spin precession due to the external magnetic field, respectively. The first and second terms in the brackets of Eq. (A.18b) represent the spin relaxation due to optical excitation and the light shift, respectively. The third term of Eq. (A.20) represents the optical pumping.

Here we introduce new variables by $\vec{m} = {}^t(m_x, m_y, m_z)$ = $\text{Tr}[\rho_g \vec{\sigma}]$, where

$$m_x = \rho_{g+g-} + \rho_{g-g+}, \quad (\text{A.22a})$$

$$m_y = (\rho_{g-g+} - \rho_{g+g-})/i, \quad (\text{A.22b})$$

$$m_z = \rho_{g+g+} - \rho_{g-g-}, \quad (\text{A.22c})$$

where ρ_g is the density matrix reduced to the ground state.

Equations (A.18b) and (A.20) become the well-known Bloch equation:

$$\dot{m}_x = -(\Gamma_g + P_+ + P_-)m_x - Q_0 m_z + Q_{LS} m_y, \quad (\text{A.23a})$$

$$\dot{m}_y = -(\Gamma_g + P_+ + P_-)m_y - Q_{LS} m_x, \quad (\text{A.23b})$$

$$\dot{m}_z = -(\Gamma_g + P_+ + P_-)m_z + Q_0 m_x + (P_+ - P_-), \quad (\text{A.23c})$$

where

$$P_{\pm} = 2fg^2 L(\delta, \gamma_{eg}) |\mathcal{E}_{\pm}|^2, \quad (\text{A.24})$$

$$Q_{LS} = 2g^2 D(\delta, \gamma_{eg}) (|\mathcal{E}_+|^2 - |\mathcal{E}_-|^2). \quad (\text{A.25})$$

Using vector notation, we obtain

$$\frac{d\vec{m}}{dt} = \vec{m} \times \vec{Q}_0 - \Gamma_g \vec{m} - P_+ (\vec{m} - \hat{z}) - P_- (\vec{m} + \hat{z}), \quad (\text{A.26})$$

where $\vec{Q}_0 = {}^t(0, Q_0, Q_{LS})$. In the cases which we concern in this thesis, the light-shift term can be neglected.

In the absence of a magnetic field, from Eq. (A.20) we have a rate equation for the ground-state populations N_{\pm} :

$$\dot{N}_{\pm} = -\frac{1}{2}\Gamma_g (N_{\pm} - N_{\mp}) + (P_{\pm} N_{\mp} - P_{\mp} N_{\pm}), \quad (\text{A.27})$$

with

$$N_{\pm} = N \rho_{g\pm g\pm},$$

where N is the atomic density.

The macroscopic magnetization \vec{M} per unit volume can be expressed in terms of \vec{m}

$$\vec{M} = \frac{\gamma \hbar}{2} N \vec{m}, \quad (\text{A.28})$$

and the z component can be represented as

$$M_z = \frac{\gamma \hbar}{2} (N_+ - N_-), \quad (\text{A.28})$$

A.2 Spatially Averaged Bloch Equation

When the atoms are pumped simultaneously by a forwardly propagating beam $E_{F\pm}$ and a backwardly propagating beam $E_{B\pm}$, we must consider the standing-wave effect. Namely the pumping rates P_{\pm} in Eq. (A.26) becomes to depend on z;

$$P_{\pm}(z) = 2fg^2L(\delta, \gamma_{eg})(|E_{F\pm}|^2 + |E_{B\pm}|^2 + f_{\pm}(z)), \quad (\text{A.29})$$

where f_{\pm} are rapidly oscillating functions of z and vanish when they are averaged over an interval much longer than the wavelength.

We must spatially average Eq. (A.26) having z dependence because the atoms in vapor moves rapidly. The average is taken over many wavelengths.

$$\begin{aligned} d\langle \vec{m} \rangle / dt = \langle \vec{m} \rangle \times \hat{Q}_0 - \Gamma_g \langle \vec{m} \rangle - \langle P_+ \rangle (\langle \vec{m} \rangle - \hat{z}) \\ - \langle P_- \rangle (\langle \vec{m} \rangle + \hat{z}), \end{aligned} \quad (\text{A.30})$$

where $\langle \cdot \rangle$ represents a spatially averaged quantity. The terms $\langle P_{\pm} \vec{m} \rangle$ can be decomposed as $\langle P_{\pm} \rangle \langle \vec{m} \rangle$, because the atoms move many wavelengths before \vec{m} changes appreciably. (Typically thermal velocity $v \sim 500$ m/s and the wavelength $\sim 0.5 \mu\text{m}$. So an atom takes

1 ns to traverse a wavelength, whereas it takes at least 1 μ s for $\langle \vec{m} \rangle$ to shift appreciably under the conditions we concern.) The spatially averaged pumping rate is

$$\langle P_{\pm} \rangle = 2fg^2L(\delta, \gamma_{eg})(|\mathcal{E}_{F\pm}|^2 + |\mathcal{E}_{B\pm}|^2). \quad (\text{A.31})$$

So we may consider that the atoms are pumped, on the average, by the sum of the forward and the backward light intensities.

A.3 Light Propagation in a Spin-Polarized Medium

In this section we shall study on the optical characteristics of a spin-polarized medium. At first we calculate the induced electric-dipole moment

$$\vec{P}(t) = (P_+ \hat{e}_+ + P_- \hat{e}_- + P_z \hat{e}_z) e^{i\omega t} + \text{c.c.} \quad (\text{A.32})$$

by an external electric field

$$\vec{E}(t) = (\mathcal{E}_+ \hat{e}_+ + \mathcal{E}_- \hat{e}_- + \mathcal{E}_z \hat{e}_z) e^{i\omega t} + \text{c.c.}, \quad (\text{A.33})$$

in the case where \vec{m} or ρ_{gigj} , ($i, j = +, -$) is given, and the excited-state population is negligibly small. The dielectric susceptibility tensor χ is given by the relation:

$$\begin{bmatrix} P_+ \\ P_- \\ P_z \end{bmatrix} = \begin{bmatrix} \chi_{++} & \chi_{+-} & \chi_{+z} \\ \chi_{-+} & \chi_{--} & \chi_{-z} \\ \chi_{z+} & \chi_{z-} & \chi_{zz} \end{bmatrix} \begin{bmatrix} \mathcal{E}_+ \\ \mathcal{E}_- \\ \mathcal{E}_z \end{bmatrix}. \quad (\text{A.34})$$

In terms of ρ , \vec{P} is given as an expectation value of the electric-dipole operator \vec{p} .

$$\begin{aligned} \vec{P}(t) &= N \text{Tr}[\rho \vec{p}] \\ &= Np[\tilde{\rho}_{g-e+} \hat{e}_+ + \tilde{\rho}_{g+e-} \hat{e}_+ + (\tilde{\rho}_{g+e+} - \tilde{\rho}_{g-e-}) \hat{z}] e^{i\omega t} + \text{c.c.} \end{aligned} \quad (\text{A.35})$$

Repeating the same procedure from Eq. (A.1) to Eq. (A.17), we can express $\tilde{\rho}_{giej}$ in terms of ρ_{gkgl} ($i, j, k, l = +, -$);

$$\begin{bmatrix} P_+ \\ P_- \\ P_z \end{bmatrix} = C \begin{bmatrix} \rho_{g-g-} & 0 & \rho_{g-g+}/\sqrt{2} \\ 0 & \rho_{g+g+} & -\rho_{g+g-}/\sqrt{2} \\ \rho_{g+g-}/\sqrt{2} & -\rho_{g-g+}/\sqrt{2} & 1/2 \end{bmatrix} \begin{bmatrix} \mathcal{E}_+ \\ \mathcal{E}_- \\ \mathcal{E}_z \end{bmatrix}, \quad (\text{A.36})$$

where $C = iNpg(-\gamma_{eg} + i\delta)^{-1}$. In terms of \vec{m} , we can have an equivalent relation:

$$\vec{P} = C(\vec{E} + i\vec{m} \times \vec{E}), \quad (\text{A.37})$$

or

$$x_{ij} = C(\delta_{ij} + i\epsilon_{ijk} m_k), \quad (\text{A.38})$$

where δ_{ij} and ϵ_{ijk} are Kronecker's δ and Eddington's ϵ , respectively.

When we consider a wave propagating in the z direction, we can neglect the components x_{iz} and x_{zi} ($i = x, y, z$ or $+, -, z$). It is because the z components of the susceptibility cannot affect the propagation of light in first order, since the z component of the induced polarization does not reradiate light in the z direction (Happer, 1972; Landau and Lifshitz, 1960). So we have

$$\begin{aligned} P_{\pm} &= x_{\pm} \mathcal{E}_{\pm} = C \rho_{g\mp g\mp} \mathcal{E}_{\pm} \\ &= (C/2)(1 \mp m_z) \mathcal{E}_{\pm}, \end{aligned} \quad (\text{A.39})$$

where $x_{\pm} = x_{\pm\pm}$.

From Maxwell's equation we have the dispersion relation:

$$k_{c\pm}^2 = \frac{\omega^2}{c^2}(1 + 4\pi\chi_{\pm}), \quad (\text{A.40})$$

with

$$k_{c\pm} = k_{\pm} - i\alpha_{\pm}, \quad (\text{A.41})$$

where k_{\pm} and α_{\pm} are the wavenumbers and the absorption coefficients for σ_{\pm} light. When $|\chi_{\pm}| \ll 1$, namely when the field envelope does not change appreciably over a wavelength, we have from Eqs. (A.40) and (A.41);

$$\alpha_{\pm} = -2k_0\pi\text{Im}(\chi_{\pm}) = \alpha(1 \mp m_z), \quad (\text{A.42a})$$

$$k_{\pm} = k_0(1 + 2\pi\text{Re}(\chi_{\pm})) = k_0 + \kappa(1 \mp m_z), \quad (\text{A.42b})$$

where

$$\alpha = \pi k_0 N p g L(\delta, \gamma_{eg}), \quad (\text{A.43a})$$

$$\kappa = \pi k_0 N p g D(\delta, \gamma_{eg}). \quad (\text{A.43b})$$

It should be noted that if we choose ω on the wing region of the absorption line (i.e. $\delta \gg \gamma_{eg}$), then

$$\frac{\kappa}{\alpha} \sim \frac{\delta}{\gamma_{eg}} \gg 1, \quad (\text{A.44})$$

and we can neglect the absorption and can consider the atoms as a dispersive medium.

APPENDIX B

CATASTROPHE

B.1 Thom's Theorem

In this appendix we describe Thom's theorem on the classification of elementary catastrophes in physical context. We set up a model called a "static model." The system equation is given by

$$\frac{dx}{dt} = -\text{grad}_x F(x, u), \quad (\text{B.1})$$

where $x = {}^t(x_1, \dots, x_n) \in M \subset \mathbb{R}^n$, $u = {}^t(u_1, \dots, u_r) \in C \subset \mathbb{R}^r$ and $F: M \times C \rightarrow \mathbb{R}$ is a smooth (infinitely differentiable) function. The variable x is usually called behavior (or state) and u is called control (or parameter). A static model can be viewed as an r -parameter family of smooth functions. As easily seen a stable steady state of the system (B.1) corresponds to a minimal point of F with respect to x for a fixed u . Generally two or more stable states coexist for given parameter values. As the parameter u is changed slowly, at some point, the number of minimal points decreases or increases. The set of such points in C is called the bifurcation set which is denoted by B . A sudden change of steady state (catastrophe) may occur when parameters are changed continuously through B (See Fig. B.1). It should be noted that only the qualitative shape of the function $F(x, u)$ governs the behavior of the system. (In fact, Fig. B.1 was drawn with a free hand.) If models F and G are qualitatively the same, the study on

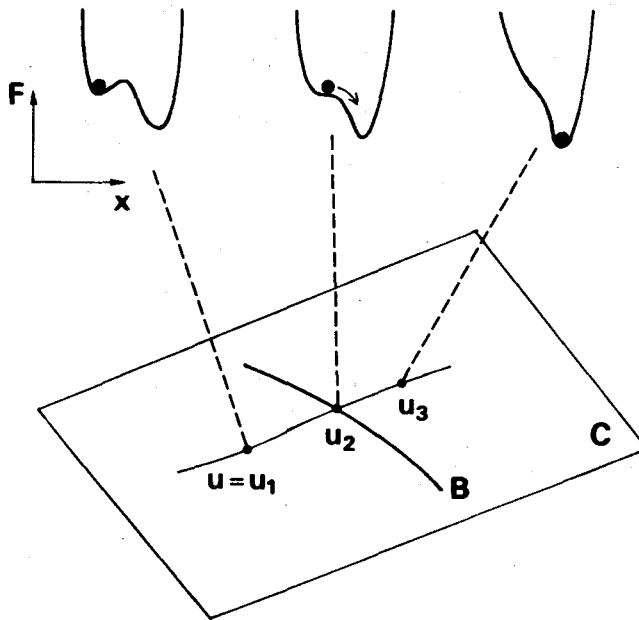


Fig. B.1 Example of a static model.

either of them is sufficient. The equivalence between F and G are stated mathematically as follows;

Definition: There exist a diffeomorphism (smooth and reversible map) $h: C \rightarrow C$, a diffeomorphism $H_u: M \rightarrow M$ parametrized by $u \in C$, and a smooth map $a: C \rightarrow \mathbb{R}$, such that

$$F(x, u) = G(H_u(x), h(u)) + a(u), \tag{B.2}$$

and $H(x, u) = H_u(x)$ defines a smooth map $H: M \times C \rightarrow M$.

If a model F is changed qualitatively by a small perturbation p, then such model is inappropriate to describe the phenomena in the real world where unpredictable perturbations are unavoidable. So we can restrict our attentions to models which do not have such property. The restriction is described as

Definition: If a model $F: M \times C \rightarrow \mathbb{R}$ is equivalent to any model $F + p: M \times C \rightarrow \mathbb{R}$, then F is structurally stable model.

Now we can state Thom's theorem as follows:

Theorem: A structurally stable static model $F: M \times C \rightarrow \mathbb{R}$ ($M \subset \mathbb{R}^n$, $C \subset \mathbb{R}^r$) for any n and for all $r \leq 4$, is equivalent to one of the following models with normal forms:

(1) Non-critical

$$x, \quad (\text{B.3a})$$

(2) Nondegenerate critical, or Morse

$$Q(x_1, \dots, x_n), \quad (\text{B.3b})$$

(3) The fold

$$x^3 + ux + Q(x_2, \dots, x_n), \quad (\text{B.3c})$$

(4) The cusp

$$\pm x^4 + ux^2 + vx + Q(x_2, \dots, x_n), \quad (\text{B.3d})$$

(5) The swallowtail

$$x^5 + ux^3 + vx^2 + wx + Q(x_2, \dots, x_n), \quad (\text{B.3e})$$

(6) The butterfly

$$\pm x^6 + tx^4 + ux^3 + vx^2 + wx + Q(x_2, \dots, x_n), \quad (\text{B.3f})$$

(7) The hyperbolic umbilic

$$x^3 + y^3 + wxy + ux + vy + Q(x_3, \dots, x_n), \quad (\text{B.3g})$$

(8) The elliptic umbilic

$$x^3 - xy^2 + w(x^2 + y^2) + ux + vy + Q(x_3, \dots, x_n), \quad (\text{B.3h})$$

(9) The parabolic umbilic

$$\pm(x^2y + y^4) + tx^2 + wy^2 + ux + vy + Q(x_3, \dots, x_n), \quad (B.3i)$$

where $t(x_1, \dots, x_n) \in M$, $x = x_1$, $y = x_2$, and $t(u_1, \dots, u_r) \in C$, $u = u_1$, $v = u_2$, $w = u_3$, and $t = u_4$. The function $Q(x_1, \dots, x_n)$ is of a form:

$$\sum_{j=i}^n \pm x_j^2$$

In the cases (1) and (2), the catastrophe does not occur. In the former, F does not have an equilibrium point. In the latter, $x = 0$ is a stable equilibrium point if Q takes the form $\sum_{i=1}^n x_i^2$.

The other seven cases represent the elementary catastrophes. It should be noted that if $Q = \sum_{j=i}^n x_j^2$, the stable equilibrium points lie in the subspace $x_1 = \dots = x_n = 0$, where the catastrophe occurs. We can, therefore, neglect the term Q . This greatly reduces the degrees of freedom of the system. Even if we have a large system on $M = \mathbb{R}^{1984}$, $C = \mathbb{R}$, for example, what we have to investigate is a one-parameter family $x^3 + ux$ (the fold).

B.2 Examples

Here we take up two examples, fold and cusp, and describe how the catastrophe takes place there.

Fold: when $u < 0$, the function $x^3 + ux$ has two extrema $x_c = \sqrt{u/3}$, and $-\sqrt{u/3}$; one is stable and the other unstable. When $u > 0$, it has no extrema. So the catastrophe occurs at $u = 0$. We plot the extrema as functions of u in Fig. B.2(a). The upper and the lower half of the parabola correspond to the stable and the unstable equilibrium point, respectively. The parabola is the catastrophe manifold, which is defined as a subset of $M \times C$ on

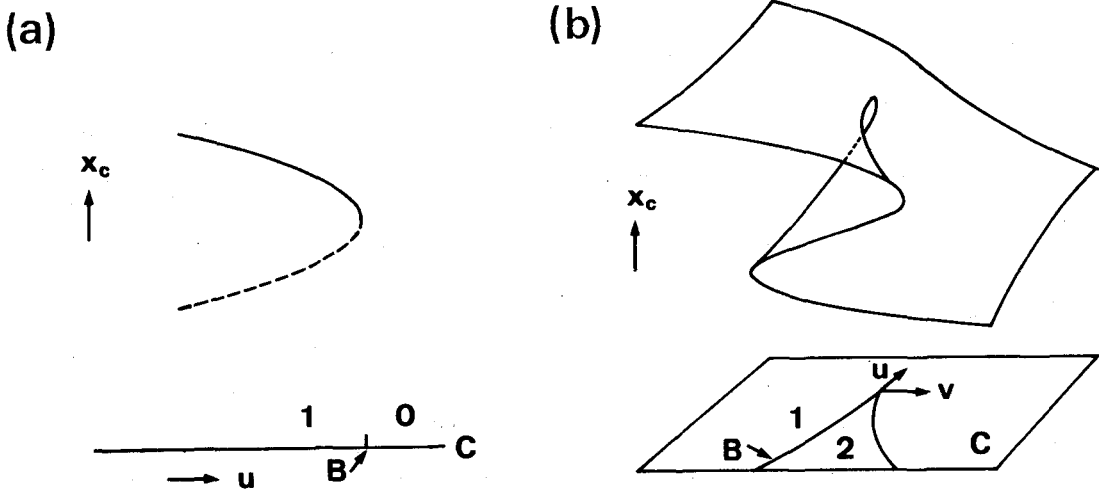


Fig. B.2 Catastrophe manifolds and bifurcation sets of (a) fold, and (b) cusp catastrophes. The numbers of stable equilibrium points are also shown.

which $\text{grad}_x F(x, u) = 0$ is satisfied. The set $B = \{0\}$ is the bifurcation set where the catastrophe takes place.

Cusp: In this case, C is two-dimensional ($r = 2$). The catastrophe manifold and the bifurcation set are pictured in Fig. B.2(b).

Now we discuss the implications of the theorem using the two examples above mentioned. Consider a one-parameter family:

$$F_v(x) = x^4 + u_0 x^2 + vx, \quad (\text{B.4})$$

which is reduced from the normal form of the cusp by setting $u = u_0 = \text{const}$. The equilibrium point x_c satisfies the relation for a given value of $v = v_c$:

$$\left. \frac{\partial F_v}{\partial x} \right|_{x = x_c} = 4x_c^3 + 2u_0 x_c + v = 0. \quad (\text{B.5})$$

To investigate the local structure of the equilibrium point, we introduce new variables X and V by

$$x = x_c + X,$$

$$v = v_c + V.$$

Equation (B.4) becomes

$$\begin{aligned} F_{v_c+V}(x_c + X) &= X^4 + 4x_c X^3 + (6x_c^2 + u_0)X^2 + VX + (X^0 \text{ term}) \\ &= G_V(X). \end{aligned} \tag{B.6}$$

Consider the following three cases:

(1) $u_0 > 0$: The coefficient of X^2 is positive and therefore the local behavior of $G_V(X)$ is equivalent to $+X^2$, which means x_c is nondegenerate critical point. In fact, the higher-order terms X^3 and X^4 can be eliminated by a transformation given in the theorem, when the second-order term is not zero. The first-order term can be eliminated by $X \rightarrow X - V/2(6x_c^2 + u_0)$. So the parameter V is a dummy parameter in this case.

(2) $u_0 < 0$: We must consider three cases where the coefficient of X^2 is positive, negative, and zero. In the first and second cases, $G_V(X)$ is equivalent to $+X^2$ and $-X^2$ respectively. In the third case, we must take X^3 term into account. Apparently the equation:

$$G_V(X) = 4x_c X^3 + VX + (X^0 \text{ term}), \tag{B.7}$$

gives the fold.

(3) $u_0 = 0$: Two cases where the coefficient of X^2 is positive and zero are possible. In the former case $G_V(X)$ is equivalent to $+X^2$ as described above. In the latter, the X^2 and X^3 terms vanish;

$$G_V(X) = X^4 + VX + (X^0 \text{ term}). \tag{B.8}$$

This one-parameter family is structurally unstable. The family corresponds to the line on the (u,v) -plane passing the point of the cusp. It is easy to make the line not to pass there by a small perturbation.

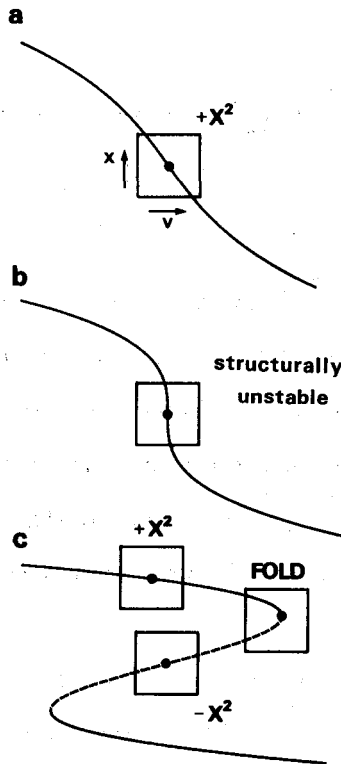


Fig. B.3 One-parameter families reduced from the cusp $x^4 + ux^2 + vx$ by setting $u = u_0 = \text{const.}$
 (a) $u_0 > 0$, (b) $u_0 = 0$,
 (c) $u_0 < 0$.

We summarize the three cases (1)–(3) in Fig. B.3, where catastrophe manifolds are pictured.

We consider the other one-parameter families buried in the cusp:

$$F_u(x) = x^4 + ux^2 + v_0x, \quad (\text{B.9})$$

where v_0 is a fixed constant. The above analysis can be applied to this case and the result is shown in Fig. B.4. Again the one-parameter family which passes the cusp point ($v_0 = 0$) is structurally unstable.

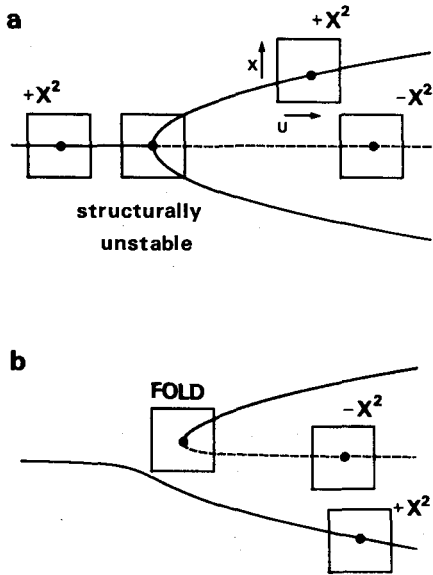


Fig. B.4 One-parameter families reduced from the cusp $x^4 + ux^2 + vx$ by setting $v = v_0 = \text{const.}$
 (a) $v_0 = 0$, (b) $v_0 \neq 0$.

From these examples, we can get the feeling that catastrophe typically encountered in a one-parameter family is the fold; a sudden disappearance (or appearance) of a stable state and an unstable state in pair. If the other type of catastrophe appears in a one-parameter family, the family is structurally unstable; in other words, it is not typical. More generally, Thom's theorem assures that in r -parameter families ($r \leq 4$) we cannot see any types of catastrophe other than the seven elementary catastrophes.

B.3 Remarks

Here we make some remarks which should be considered when we apply the theorem to our systems.

- (1) Localness: The boxes in Figs. B.3 and B.4 represent the

set $M \times C$. If we extend the height of the box of the fold in Fig. B.3(c) to contain the other branch, the figure in the box cannot be corresponded to the fold structure in Fig. B.2(a). This means the localness of the theorem. Similarly when we extend the parameter range C to contain the other fold, the correspondence also breaks. It should be noted, however, the whole structure in Fig. B.3(c) is not a patch-work of the one-parameter families but a cross-section of the catastrophe manifold of the cusp. The cusp point ($x = u = v = 0$) determines the configuration of critical points in Fig. B.3. So even when we treat an r -parameter family, consideration of an r' -parameter family ($r' > r$) is sometimes needed, namely, we must include some hidden parameters.

(2) *Symmetry*: Although a one-parameter family:

$$F_u(x) = x^4 + ux^2, \quad (\text{B.10})$$

is structurally unstable (Fig. B.4(a)), it frequently appears in text books and is referred as a pitchfork bifurcation. It appears when the system has a symmetry with respect to the transformation $x \rightarrow -x$. Strictly speaking, such system may have some imperfections and behaves as in Fig. B.4(b); namely a symmetric system is structurally unstable or not generic. Even so, the pitchfork bifurcation is meaningful because it approximates the situation. A more positive attitude is possible. Haken (1981) said,

"At the risk of provoking mathematicians I should nevertheless mention that in my opinion conclusions based on generic properties may be different for mathematicians and physicists. The reason for this lies in the fact that in mathematical sense generic refers to a typical property for solutions of a large class of different equations. On the other hand in physics we deal with specific

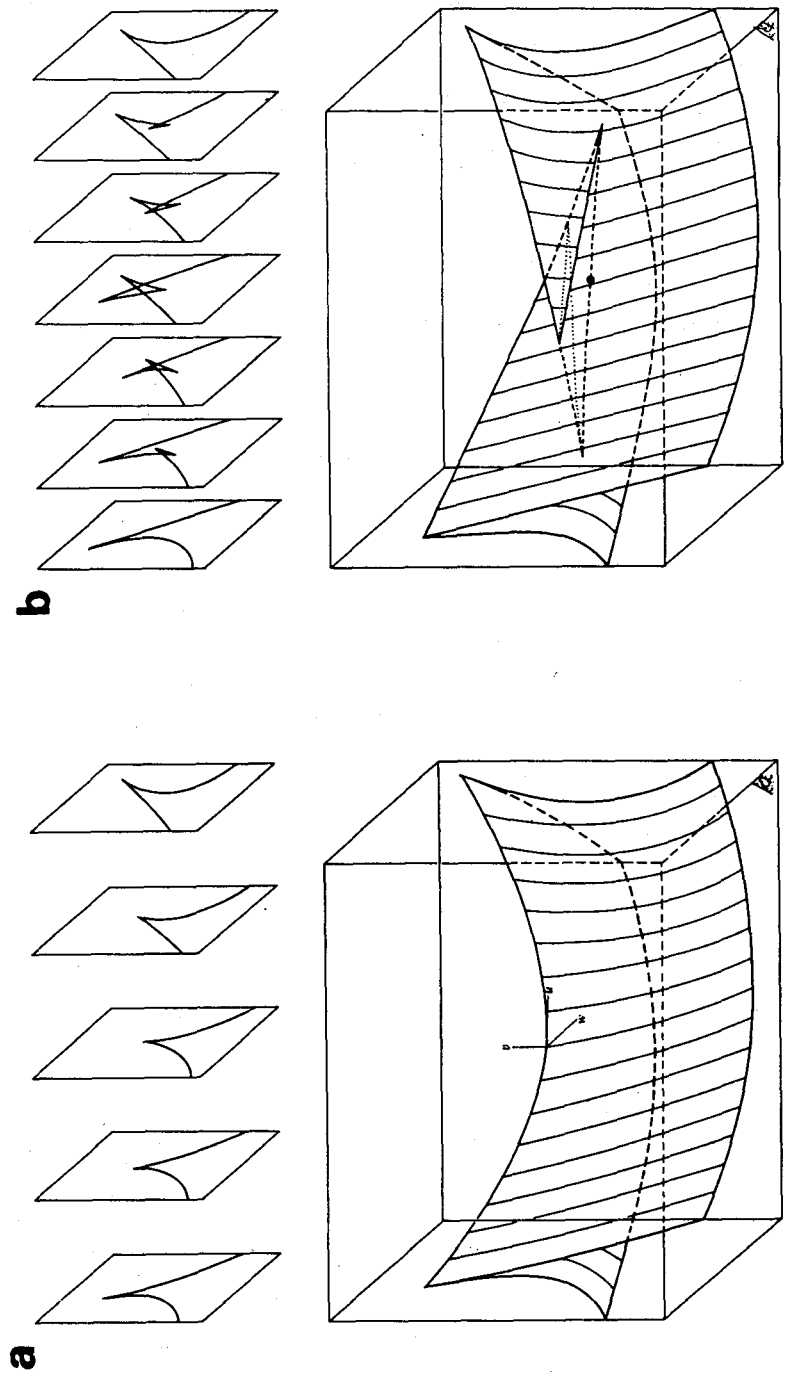


Fig. B.5 Bifurcation set for the butterfly when (a) $t > 0$, (b) $t < 0$ (from Thom, 1975).

equations bringing out specific laws and having, more or less obvious, symmetry properties. Thus in my opinion the laws of nature are highly non-generic and it is just the aim of physics to explain why such laws have such and such specific properties.'

Finally we present the bifurcation set for the butterfly:

$$x^6 + tx^4 + ux^3 + vx^2 + wx, \quad (\text{B.11})$$

for cases $t > 0$ (Fig. B.5(a)) and $t < 0$ (Fig. B.5(b)). It is used in Chapter 2.

APPENDIX C

BIFURCATION IN MODIFIED BLOCH EQUATION

In this appendix we investigate bifurcation phenomena seen in the modified Bloch equation (4.24).

C.1 Liénard's Method

At first, we present a sufficient condition for the existence of a limit cycle in a certain class of differential equation called Liénard's equation (Nemytskii and Stepanov, 1960). Liénard's equation has the following form:

$$\frac{d^2x}{dt^2} + f(x)\frac{dx}{dt} + g(x) = 0. \quad (\text{C.1})$$

Introducing a new variable $y = (dx/dt) + F(x)$ where

$$F(x) = \int_0^x f(x)dx, \quad (\text{C.2})$$

we obtain the equations

$$dx/dt = y - F(x), \quad (\text{C.3a})$$

$$dy/dt = -g(x). \quad (\text{C.3b})$$

For this system we have a theorem on the existence of a limit cycle.

Theorem: Suppose that

1. $g(x)$ satisfies

$$xg(x) > 0 \text{ for } x \neq 0, \int_0^{\infty} g(x)dx = \infty.$$

2. $F(x)$ is single valued for $-\infty < x < +\infty$, satisfies a Lipschitz condition in every finite intervals and $xF(x) < 0$ for $x \neq 0$ and $|x|$ sufficiently small.

3. There exist constants N, k, k' ($k' < k$) such that $F(x) \geq k$ for $x > N$, $F(x) \leq k'$ for $x < -N$.

Then the system (C.1) admit at least one limit cycle.

C.2 Takens' Normal Form

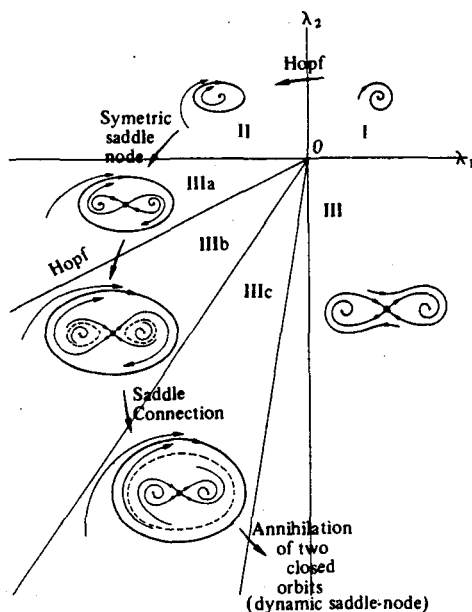


Fig. C.1 Bifurcation set of Takens' normal form (from Abraham and Marsden, 1978).

The qualitative bifurcations of Eq. (4.24) can be analyzed more precisely. Takens (1973) has classified certain generic or stable bifurcations of two-parameter families of vector fields on the plane. Our system can be reduced to one of the normal forms:

$$dx/dt = y, \quad (C.4a)$$

$$dy/dt = -\lambda_2 x - \lambda_1 y - x^3 - x^2 y. \quad (C.4b)$$

At the point $\lambda_1 = \lambda_2 = 0$, the linear part has degenerate singularities. The point corresponds to the crossing of the critical lines 1 and 2 in Fig. 4.4. The bifurcation diagram for Eq. (C.4) is given in Fig. C.1. Phase portrait in each region is also shown. The correspondence to Fig. 4.4 is clear.

APPENDIX D

CHAOS

D.1 Introduction

In this appendix, we give a short review on chaos and introduce some terms used in Chapters 5 and 6. By the term "chaos," we mean an irregular motion of a dynamical system which is, however, governed by deterministic equations. The seeming contradiction prevents people from studying chaos substantially for a long time, although it was known to some people (e.g. Poincaré).

In 1963, Lorenz showed that a simple equation system:

$$\frac{dx}{dt} = -\alpha(x - y), \quad (\text{D.1a})$$

$$\frac{dy}{dt} = -xz + rx - y, \quad (\text{D.1b})$$

$$\frac{dz}{dt} = xy - bz, \quad (\text{D.1c})$$

exhibits an irregular (non-periodic) motion for some values of parameters α , b , and r . The Lorenz equation was reduced from a fluid-convection problem and the irregular motion is connected to the turbulence. In Fig. D.1 we show an example of the trajectory in the (x, y, z) space. Any solutions originating from different initial points, eventually attracted to the two-leaf structure. The cross-section of the attractor is very complicated, namely, no matter how much we magnify a part, we can see some structures (Mandelbrot, 1982). So it is called a "strange attractor."

We have correspondences between the attractors and the steady-

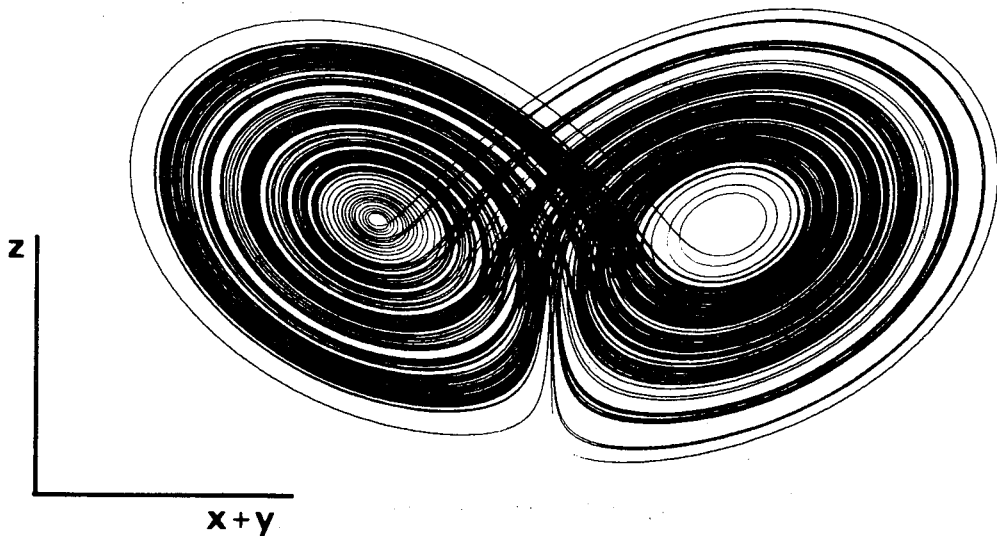


Fig. D.1 A trajectory of the Lorenz equation with $\sigma = 10$, $b = 8/3$, $r = 28$.

state solutions listed below:

- fixed point ————— stationary equilibrium
- limit cycle ————— periodic motion
- torus ————— multiply periodic motion
- strange attractor — aperiodic motion (turbulence)

Ruelle and Takens (1971) offered a possible mechanism by which turbulent solutions to the Navier-Stokes equations could appear. They showed that, as the system parameter is varied, the bifurcations progress as follows: fixed point \rightarrow limit cycle \rightarrow torus \rightarrow strange attractor. They also showed on the basis of quite general argument that such bifurcation scheme is not so rare, in other words, the occurrence of strange attractor is not special affairs.

Here we introduce the Poincaré map which is a useful tool to

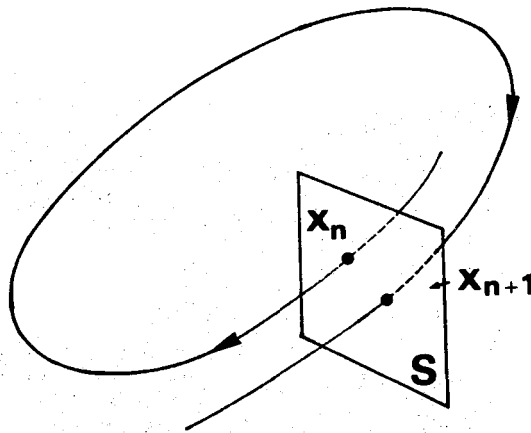


Fig. D.2 Poincaré map.

investigate the bifurcations of a periodic orbit. Consider a differential equation in a three-dimensional space and a surface S transverse to the orbits (Fig. D.2). An orbit starting from x_n on S hits S again at x_{n+1} . Such a correspondence defines a map from S to S :

$$x_{n+1} = F(x_n). \quad (\text{D.2})$$

We can draw many informations from the Poincaré map instead of the original differential equation. For example, if x is a fixed point of the map F then we know the orbit through x is a closed orbit. Aside from above point of view, Eq. (D.2) with discrete time n (difference equation) has its importances. The dynamics of biological populations can be described by Eq. (D.2) where n represents the generation (May, 1976). Mathematically, a one-dimensional map is rather simple and many rigorous results on chaos are obtained (Collet and Eckmann, 1980).

To get an insight into the mechanism which generates chaos, we

consider a one-dimensional map:

$$x_{n+1} = 1 - 2|x_n - 1/2|, \quad (D.3)$$

where $x_n \in [0,1]$. We can easily see that if the initial condition has an uncertainty $\pm\epsilon$, then after $m \sim \log_2(1/\epsilon)$ iteration of the map, we will have essentially no clue as to where x lies in the interval $[0,1]$. For example, for $\epsilon \sim 10^{-12}$, $m = 40$ (Ott, 1981). This sensitive dependence on the initial condition is one of the criteria for chaos. We show another way to see how erratically a sequence (x_0, x_1, x_2, \dots) is generated by Eq. (D.3). From the sequence we make a binary sequence (b_0, b_1, b_2, \dots) where b_n is defined as

$$b_n = \begin{cases} 0 & (x_n \in [0, 1/2)) \\ 1 & (x_n \in [1/2, 1]). \end{cases}$$

In Fig. D.3, we show the sequences as functions of initial value x_0 . When $x_0 = 0.3$, for instance, we have a sequence $(0, 1, 0, 0, 1, 1, \dots)$. In Fig. D.3 we can find any binary sequence (even if it is given from coin tosses).

D.2 Roads to Chaos

In Appendix B, we have seen the bifurcations of fixed points, such as a saddle-node connection and a pitchfork bifurcation, and, in Appendix C, the bifurcations lying between periodic motion and a stationary state such as a Hopf bifurcation (Marsden and McCracken, 1976), a coalescence of stable and unstable limit cycles, and a saddle connection. In the course of nature, a bifurcation (or a sequence of bifurcations) which lies between a non-chaotic state and a chaotic state should be investigated. Such bifurcation is

doubly periodic motion (in f_1 and f_2). Then it is likely that through the third bifurcation the system possesses a strange attractor.

Feigenbaum: An infinite sequence of subharmonic bifurcations appear at μ_1, μ_2, \dots . The ratio $(\mu_{i+1} - \mu_i)/(\mu_i - \mu_{i-1})$ approaches a constant $\delta = 4.66920\dots$ (Feigenbaum constant) as i tends to infinity. Above the accumulation point μ_∞ , one will see aperiodic behavior.

Pomeau-Manville: As the parameter μ is varied over a critical value μ_c , one sees intermittently turbulent behavior of random duration with laminar phases of mean duration $\sim (|\mu - \mu_c|^{-1/2})$ in between.

D.3 Bifurcations in One-Dimensional Maps

To see the examples of the scenarios, we consider a family of one-dimensional maps:

$$x_{n+1} = \mu x_n (1 - x_n). \quad (\text{D.4})$$

We show the bifurcation diagram in Fig. D.4 which is obtained as follows. For a given value of μ , we choose an initial value x_0 and iterate the mapping (D.4) until the transient behavior settles down. Then we plot successive values x_n . The procedure is repeated for each μ . In Fig. D.4, typical period-doubling bifurcations to chaos are seen. At $\mu = \mu_0$, a bifurcation takes place from a stationary state ($x_{n+1} = x_n$) to a period-2 oscillation ($x_{n+2} = x_n$), and at $\mu = \mu_1$, a bifurcation from the period-2 to a period-4 ($x_{n+4} = x_n$). Generally, at $\mu = \mu_k$, a bifurcation from a

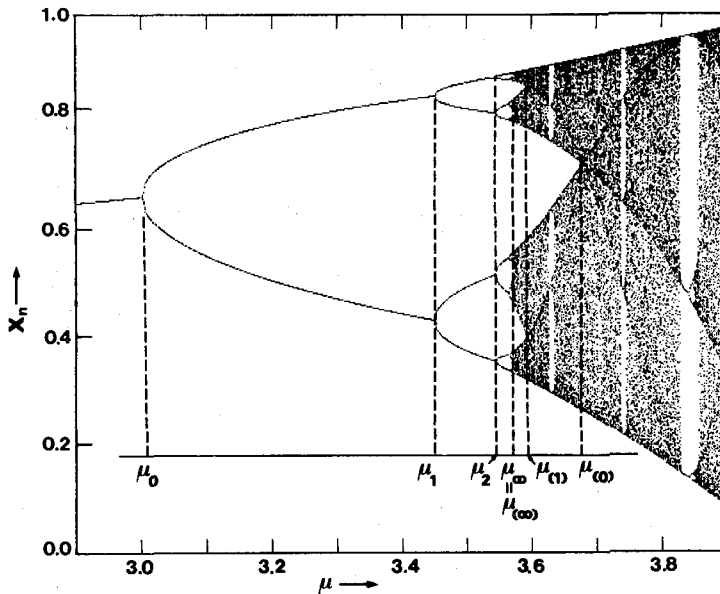


Fig. D.4 Bifurcation diagram of Eq. (D.4).

period- 2^k to a period- 2^{k+1} oscillation occurs. Above the accumulation point μ_∞ , the system oscillates aperiodically. Using a method of renormalization group in statistical mechanics, Feigenbaum (1978) showed that a ratio $(\mu_{n+1} - \mu_n)/(\mu_n - \mu_{n-1})$ approaches a constant $\delta = 4.66920\dots$ asymptotically. The remarkable point is that the constant does not depend on the choice of the family of mapping.

Above μ_∞ , a series of reverse bifurcations at $\mu = \mu_{(k)}$ appears. A state between $\mu_{(k)}$ and $\mu_{(k-1)}$ is called a period- 2^k chaos, where the orbit drops in the 2^k bands in cyclic and therefore a kind of order remains. A series $\{\mu_{(n)}\}$ has the same universal property as $\{\mu_n\}$.

Another marked feature of the bifurcation diagram is the existence of windows in the chaotic region, where the periodic motion reappears. In Fig. D.5 we show a blowup of a window. At

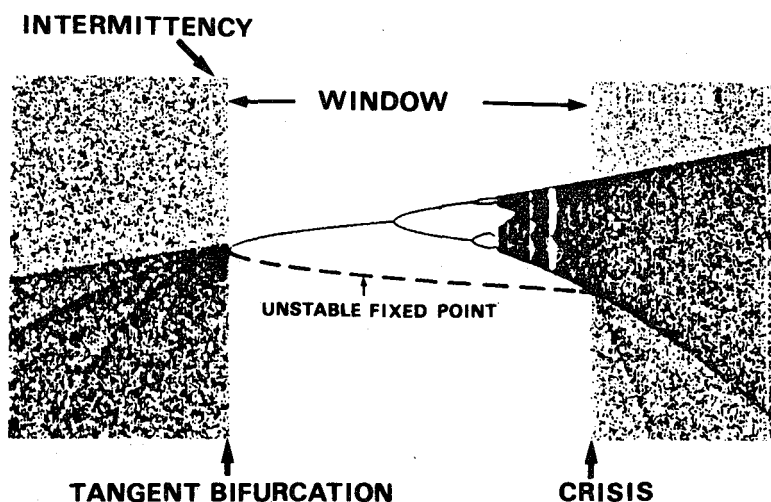


Fig. D.5 Magnified view of window.

the left edge, a stable periodic orbit appears through a tangent bifurcation (a saddle-node connection) with an unstable periodic orbit. The bifurcation is preceded by the intermittency, namely when we decrease μ across the left boundary, chaotic oscillation intermitted by periodic motion with random duration appears. The window is closed by a crisis (Grebogi et al., 1982; 1983) as μ is increased. The crisis is a bifurcation of a chaotic attractor, which appears when an unstable fixed point (or an unstable periodic orbit) collides to the attractor. In the case of Fig. D.5, the unstable periodic orbit created at the left edge of the window collides with the chaotic attractor which is bifurcated from the stable periodic orbit.

APPENDIX E

CLASSIFICATION OF A FIXED POINT OF 2D MAP

The stability of a fixed point of a two-dimensional map T can be characterized by the eigenvalues ρ_1 and ρ_2 of the linearized map (Kawakami and Kobayashi, 1979; Kawakami, 1979; Guckenheimer and Holmes, 1982). If $|\rho_1| \neq 1$ and $|\rho_2| \neq 1$, the fixed point is called simple, or hyperbolic. A fixed point is called orientation preserving when $\rho_1\rho_2 > 0$ and orientation reversing when $\rho_1\rho_2 < 0$. An orientation preserving simple fixed point is classified as

Completely stable (S): $|\rho_1| < 1, |\rho_2| < 1$

Completely unstable (U): $|\rho_1| > 1, |\rho_2| > 1$

Directly unstable (D): $0 < \rho_1 < 1 < \rho_2$

Inversely unstable (I): $\rho_1 < -1 < \rho_2 < 0$

and an orientation reversing fixed point is classified as

Completely stable (SR): $|\rho_1| < 1, |\rho_2| < 1$

Completely unstable (UR): $\rho_1 < -1, \rho_2 > 1$

Directly unstable (DR): $-1 < \rho_1 < 0, 1 < \rho_2$

Inversely unstable (IR): $\rho_1 < -1, 0 < \rho_2 < 1$.

We can extend the above notation to n -periodic points, namely, if an n -periodic point P is a fixed point DR of the map $T^{(n)}$, for example, then we denote P as DR^n .

REFERENCES

- Abraham, R. and J. E. Marsden, 1978, Foundations of Mechanics, (Benjamin, Reading).
- Agrawal, G. P. and H. J. Carmichael, 1979, Phys. Rev. A 19, 2074.
- Agrawal, G. P. and C. Flytzanis, 1981, Phys. Rev. A 24, 3173.
- Arecchi, F. T. and F. Lisi, 1982, Phys. Rev. Lett. 49, 94.
- Arecchi, F. T., J. Kurman, and A. Politi, 1983, Opt. Commun. 44, 421.
- Areshev, I. P., T. A. Murina, N. N. Rosanov, and V. K. Subashiev, 1983, Opt. Commun. 47, 414.
- Bhaskar, N. D., M. Hou, B. Suleman, and W. Happer, 1979, Phys. Rev. Lett. 43, 519.
- Bonifacio, R. and L. A. Lugiato, 1976, Opt. Commun. 19, 172.
- Bonifacio, R. and L. A. Lugiato, 1978a, Phys. Rev. A 18, 1129.
- Bonifacio, R. and L. A. Lugiato, 1978b, Lett. Nuovo Cimento 21, 510.
- Bonifacio, R., L. A. Lugiato, and M. Gronchi, 1979, in Laser Spectroscopy IV, edited by H. Walther and K. W. Rothe (Springer, Berlin).
- Bowden, C. M., M. Ciftan, and H. R. Robl (eds.), 1981, Optical Bistability (Plenum, New York).
- Carmichael, H. J., C. M. Savage, and D. F. Walls, 1983, Phys. Rev. Lett. 50, 163.
- Carmichael, H. J., 1983, in Laser Physics, Lecture Notes in Physics 182, edited by J. D. Harvey and D. F. Walls (Springer, Berlin) p. 64.
- Cecchi, S., G. Giusfredi, E. Petriella, and P. Salieri, 1982, Phys.

- Rev. Lett. 49, 1928.
- Collet, P. and J. P. Eckmann, 1980, Iterated Maps on the Interval as Dynamical Systems (Birkhauser, Boston).
- Condon, E. U. and G. H. Shortley, 1970, The Theory of Atomic Spectra (Cambridge Univ. Press, Cambridge).
- Dehmelt, H. G., 1957, Phys. Rev. 1924, 1924.
- Derstine, M. W., H. M. Gibbs, F. A. Hopf, and D. L. Kaplan, 1982, Phys. Rev. A 26, 3720.
- Derstine, M. W., H. M. Gibbs, F. A. Hopf, and D. L. Kaplan, 1983, Phys. Rev. A 27, 3200.
- Eckmann, J. -P., 1981, Rev. Mod. Phys. 53, 643.
- Feigenbaum, M. J., 1978, J. Stat. Phys. 19, 25.
- Gibbs, H. M., S. L. McCall, and T. N. C. Venkatesan, 1976, Phys. Rev. Lett. 36, 1135.
- Gibbs, H. M., S. L. McCall, A. C. Grossard, A. Passner, W. Wiegman, and T. N. C. Venkatesan, 1979, in Laser Spectroscopy IV, edited by H. Walther and K. W. Rothe (Springer, Berlin).
- Gibbs, H. M., F. A. Hopf, D. L. Kaplan, and R. L. Shoemaker, 1981, Phys. Rev. Lett. 46, 474.
- Giglio, M., S. Musazzi, and U. Perini, 1981, Phys. Rev. Lett. 47, 243.
- Gozzini, A., 1962, C. R. Acad. Sci. (Paris) 255, 1905.
- Graeme, J. G., 1973, Applications of Operational Amplifiers (McGraw-Hill, New York).
- Grebogi, C., E. Ott, and J. A. York, 1982, Phys. Rev. Lett. 48, 1507.
- Grebogi, C., E. Ott, and J. A. York, 1983, Physica 7D, 181.
- Guckenheimer, J. and P. Holmes, 1982, Nonlinear Oscillations, Dynamical Systems and Bifurcations of Vector Fields (Springer,

Berlin).

Haken, H., 1981, Chaos and Order in Nature, edited by H. Haken (Springer, Berlin).

Haken, H., 1983, Synergetics (Springer, Berlin).

Happer, W., 1972, Rev. Mod. Phys. 105, 1924.

Hermann, J. A. and D. F. Walls, 1982, Phys. Rev. A 26, 2085.

Hopf, F. A., D. L. Kaplan, H. M. Gibbs, and R. L. Shoemaker, 1982, Phys. Rev. A 25, 2172.

Ikeda, K., 1979, Opt. Commun. 30, 257.

Ikeda, K., H. Daido, and O. Akimoto, 1980, Phys. Rev. Lett. 45, 709.

Ikeda, K. and O. Akimoto, 1982, Phys. Rev. Lett. 49, 1467.

Ikeda, K., K. Kondo, and O. Akimoto, 1982, Phys. Rev. Lett. 49, 1467.

Jewell, J. L., H. M. Gibbs, S. S. Tarng, A. C. Gossard, and W. Wiegman, 1982, Appl. Phys. Lett. 40, 291.

Joseph, D. D., 1981, Hydrodynamic Instabilities and the Transition to Turbulence, edited by H. L. Swinney and J. P. Gollub (Springer, Berlin).

Kaplan, A. E. and P. Meystre, 1982, Opt. Commun. 40, 229.

Kastler, A., 1961, C. R. Acad. Sci. (Paris) 252, 2396.

Kawakami, H., 1979, Kokyuroku (Research note in Research Institute for Mathematical Sciences, Kyoto University) 370, 88 (in Japanese).

Kawakami, H. and K. Kobayashi, 1979, Bull. of Faculty of Engineering, Tokushima Univ. 16, 29.

Kitano, M., T. Yabuzaki, and T. Ogawa, 1981a, Phys. Rev. Lett. 46, 926.

Kitano, M., T. Yabuzaki, and T. Ogawa, 1981b, Phys. Rev. A 24,

- 3156.
- Kitano, M., T. Yabuzaki, and T. Ogawa, 1983, Phys. Rev. Lett. 50, 713.
- Kitano, M., T. Yabuzaki, and T. Ogawa, 1984, Phys. Rev. A 29, 1288.
- Landau, L. D. and E. M. Lifshitz, 1960, Electrodynamics of Continuous Media (Addison-Wesley, Reading).
- Lorenz, E. N., 1963, J. Atmos. Sci. 20, 130.
- Mackey, M. C. and L. Glass, 1977, Science 197, 287.
- Manabe, T., 1979, Thesis, Kyoto University.
- Mandelbrot, B. B., 1982, The Fractal Geometry of Nature (Freeman, San Francisco).
- Marsden, J. E. and M. McCracken, 1976, The Hopf Bifurcation and Its Applications (Springer, New York).
- Maurer, J. and A. Libchaber, 1979, J. Phys. (Paris), Lett. 40, 419.
- May, M., 1976, Nature 261, 459.
- McCall, S. L., 1978, Appl. Phys. Lett. 32, 284.
- McCartan, D. G. and J. M. Farr, 1976, J. Phys. B 9, 985.
- McLaughlin, D. W., J. V. Moloney, and A. C. Newell, 1983, Phys. Rev. Lett. 51, 75.
- Mitschke, F., J. Mlynek, and W. Lange, 1983, Phys. Rev. Lett. 50, 1660.
- Moloney, J. V. and H. M. Gibbs, 1982, Phys. Rev. Lett. 48, 1607.
- Nakatsuka, H., S. Asaka, H. Itoh, K. Ikeda, and M. Matsuoka, 1983, Phys. Rev. Lett. 50, 109.
- Nemytskii, V. V. and V. V. Stepanov, 1960, Qualitative Theory of Differential Equations (Princeton Univ. Press, Princeton).
- Nicolis, G. and I. Prigogine, 1977, Self-Organization in Non-

Equilibrium Systems (Wiley, New York).

- Omont, A., 1977, *Progress in Quantum Electronics* 5, 69.
- Ott, E., 1981, *Rev. Mod. Phys.* 53, 655.
- Parigger, C., P. Zoller, and D. F. Walls, 1983, *Opt. Commun.* 44, 213.
- Poston, T. and I. Stewart, 1978, Catastrophe Theory and Its Applications (Pitman, London).
- Poston, T., D. F. Walls, and P. Zoller, 1982, *Optica Acta* 29, 1691.
- Ruelle, D. and F. Takens, 1971, *Commun. Math. Phys.* 20, 167.
- Sandle, W. J. and M. W. Hamilton, 1983, in Laser Physics, Lecture Notes in Physics 182, edited by J. D. Harvey and D. F. Walls (Springer, Berlin) p. 54.
- Savage, C. M., H. J. Carmichael, and D. F. Walls, 1982, *Opt. Commun.* 42, 211.
- Schumacher, R. T., 1981, *Acoustica* 48, 71.
- Schumacher, R. T., 1983, Private communication.
- Smith, P. W. and W. J. Tomlinson, 1981, *IEEE Spectrum*, June, 26.
- Szöke, A., V. Daneu, J. Goldhar, and N. A. Kurnit, 1969, *Appl. Phys. Lett.* 15, 376.
- Tam, A. C. and W. Happer, 1977, *Phys. Rev. Lett.* 38, 278.
- Testa, J., J. Perez, and C. Jeffries, 1982, *Phys. Rev. Lett.* 48, 714.
- Thom, R., 1975, Structural Stability and Morphogenesis (Benjamin, Reading).
- Walls, D. F., C. V. Kunasz, P. D. Drummond, and P. Zoller, 1981, *Phys. Rev. A* 24, 627.
- Wieman, C. and T. W. Hänsch, 1976, *Phys. Rev. Lett.* 36, 1170.
- Wersinger, J. M., J. M. Finn, and E. Ott, 1980, *Phys. Rev. Lett.*

44, 453.

Yabuzaki, T., H. Hori, and M. Kitano, 1982, Japanese J. Appl. Phys. 21, 504.

Yabuzaki, T., M. Kitano, and T. Ogawa, 1983, Proceedings of International Conference on Lasers '82, New Orleans, ed. R. Powell (STS press, Mclean).

Yabuzaki, T., T. Okamoto, M. Kitano, and T. Ogawa, 1984, Phys. Rev. A 29, (April).

Zeeman, E. C., 1976, Sci. Am. 234, 65.

Zeeman, E. C., 1977, Catastrophe Theory (Addison-Wesley, Reading).